A large-stroke planar MEMS-based stage with integrated feedback

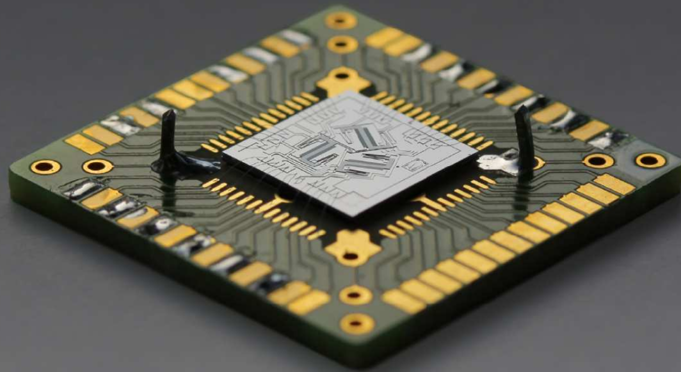

Bram Krijnen

A large-stroke planar MEMS-based stage with integrated feedback

Bram Krijnen

This research is conducted in the CLEMPS research project with project number PNE07004, supported by the Dutch association Point-One, empowered by the Ministry for Economic Affairs. The research was carried out at Demcon Advanced Mechatronics, Enschede, The Netherlands, and at the Mechanical Automation & Mechatronics and the Transducers Science & Technology research groups of the University of Twente, Enschede, The Netherlands.

UNIVERSITY OF TWENTE.

On the cover, a digital camera image of one of the fabricated 3DOF stages, as described in Chapter 6 of this thesis. The device is wirebonded to a PCB for electrical connection. The MEMS chip has a size of 8x8mm^2.
(Canon EOS 50D; 60mm, f/7.1, 1/200s, ISO-100)
Design & photography by Marjolein Stegeman; www.movingfocus.nl

Title	A large-stroke planar MEMS-based stage with integrated feedback
Author	Bram Krijnen
Contact	`krijnenbram@gmail.com`
ISBN	978-90-365-3730-8
DOI	10.3990/1.9789036537308

© Bram Krijnen, Enschede, the Netherlands, 2014
Printed by CPI-Koninklijke Wöhrmann, Zutphen, The Netherlands

A large-stroke planar MEMS-based stage with integrated feedback

Dissertation

to obtain
the degree of doctor at the University of Twente,
on the authority of the rector magnificus,
prof. dr. H. Brinksma,
on account of the decision of the graduation committee,
to be publicly defended
on Friday, 26 September 2014 at 12:45

by

Bram Krijnen

born on 3 July 1983,
in Apeldoorn, the Netherlands

This dissertation is approved by

Prof. dr. ir. J.L. Herder	University of Twente (promotor)
Prof. dr. ir. L. Abelmann	University of Twente (promotor)
Dr. ir. D.M. Brouwer	University of Twente (assistant promotor)

Graduation committee

Prof. dr. G.P.M.R. Dewulf	University of Twente (chairman, secretary)
Prof. dr. ir. J.L. Herder	University of Twente (promotor)
Prof. dr. ir. L. Abelmann	University of Twente (promotor)
Dr. ir. D.M. Brouwer	University of Twente (assistant promotor)
Prof. dr. ir. A. de Boer	University of Twente
Dr. ir. N.R. Tas	University of Twente
Prof. ir. R.H. Munnig Schmidt	Delft University of Technology
Prof. Dr.-Ing. L. Zentner	Ilmenau University of Technology
Dr. M.A. Lantz	IBM Zürich Research Laboratory

Paranymphs

Ir. J.H.J.A. (Jack) Krijnen
Ir. K.R. (Koen) Swinkels

Contents

1 Introduction **1**
1.1 Background 2
1.2 Objectives 3
1.3 Outline 4

2 Flexures for large stroke electrostatic actuation in MEMS **7**
2.1 Introduction 8
2.2 Method 10
2.3 Pull-in theory 11
2.3.1 Iterative model 11
2.3.2 Mechanical analysis 13
2.3.3 Electrostatic analysis 13
2.4 Flexures and optimization 16
2.4.1 Flexure mechanisms 16
2.4.2 Model verification 18
2.4.3 Wafer footprint 19
2.4.4 Optimization results 21
2.5 Design and fabrication 23
2.6 Experiment 25
2.7 Conclusion 28

3 Deflection and pull-in of a misaligned comb drive finger **29**
3.1 Introduction 30
3.2 Model description 31
3.2.1 Energy Functional 31
3.3 Analytic bifurcation calculations 33
3.3.1 Exact Solution 33
3.3.2 Approximate Solution 35
3.3.3 Perturbed Bifurcation Problem 36
3.4 Numerical calculations 37
3.5 Experimental validation 38
3.5.1 Experiments 38
3.5.2 Finite-Element Calculations 40
3.5.3 Measurement Results 41
3.6 Conclusions 42

4 A single-mask thermal displacement sensor in MEMS **45**
4.1 Introduction 46
4.2 Modeling and model verification 47
4.2.1 Lumped capacitance model 47
4.2.2 Resistivity and doping concentration 50
4.2.3 Temperature profile and power flow balance 52
4.2.4 Influence of heater dimensions 54
4.2.5 Operating mode and setpoint 56
4.3 Design 59
4.4 Fabrication 60
4.5 Experiment 61
4.5.1 Measurement setup 61
4.5.2 Sensor output and noise 63
4.5.3 Time constants and drift 64
4.6 Conclusion 65

5 Vacuum behavior and control of a MEMS stage **67**
5.1 Introduction 68
5.2 Theory 70
5.2.1 Vacuum behavior 70
5.2.2 Control 74
5.3 Experimental 76
5.4 Results 77
5.4.1 Vacuum behavior 78
5.4.2 Control 82
5.5 Discussion 85
5.6 Conclusions 86

6 A large-stroke 3DOF stage with integrated feedback in MEMS **87**
6.1 Introduction 88
6.2 Theory 90
6.2.1 Geometry 90
6.2.2 Electrostatic pull-in and range of motion 92
6.2.3 Optimization 94
6.2.4 Feedback control 95
6.3 Experimental 97
6.4 Results 98
6.4.1 Identification 98
6.4.2 Control 100
6.4.3 Range of Motion 100
6.5 Conclusions 102

7 Discussion and conclusions **105**
7.1 Discussion 106
7.2 Conclusions 106

Appendix A: Process Document **109**

Appendix B: Images **111**

Bibliography **117**

Summary **129**

Samenvatting **131**

Nawoord **133**

Chapter 1

Introduction

Micro-electromechanical systems (MEMS) are all around us nowadays, especially in sensor technology. MEMS-based positioning stages can serve as an enabling technology for many more applications. In this chapter we discuss the opportunities, objectives and outline of this research.

1.1 Background

From the 1980's on there is a strong increase in the number of applications that use MEMS-based actuation or sensing. One of the first examples is an accelerometer integrated in IC technology, consisting of little more than a mass on a beam [111]. Many sensor applications have been reported in the years after, such as pressure sensors [34] and cantilevers for use in atomic force microscopy [10]. Actuation of MEMS structures emerges some years after. A nice example is the use of a Digital Micromirror Device inside a DLP projector [52, 112]. Millions of micromirrors can be rotated individually to switch single pixels on or off, and anything in between by fast switching. The increasing amount of nozzles for printing accelerated the development of integrated heaters in an ink-jet printhead [3]. An example of a complete mechatronic system in MEMS is the rate sensor or gyroscope, in which actuation and sensing is combined in one application [45, 90]. Nowadays MEMS sensors are widely used in the automotive and aerospace industry for example in airbags for crash detection and in airplane roll/tilt stability control. Due to their small size and low cost, MEMS applications are also becoming increasingly popular in consumer products like in the Nintendo Wii for motion sensing, in digital cameras for image stabilization, and in smartphones for navigation or sports tracking. Micro-electromechanical systems are all around us.

MEMS applications do not only benefit from their small volume and low cost, they can also provide a superior performance. Several books have been published in the field of mechatronics that focus on the design principles for high stiffness and low mass to make a fast time response possible [68, 120, 114]. By scaling down from a macro-scale to a micro-scale, the mass of structures ($m \sim r^3$) decreases more rapidly than the stiffness ($k \sim r$), which inherently means a higher eigenfrequency ($f_0 \sim \sqrt{k/m} \sim 1/r$) and a faster response time. This opens up a range of interesting applications for MEMS-based positioning stages, for example integrated optical components [97], probe-based data storage systems [36], and sample or beam manipulators for use in electron microscopes [25, 94, 133]. In a broad perspective, the work on small manipulators can serve as an enabling technology for new applications when it is available.

For the actuation of a stage in MEMS typically thermal or electrostatic actuators are used. The drawbacks of thermal actuators are the relatively large time constant, therefore the limited actuation bandwidth, and the relatively high power consumption [23, 47, 102]. Flexure-based designs are commonly used to increase the positioning repeatability due to the lack of friction, hysteresis and play [120, 51, 55, 119]. Electrostatic comb-drive actuators in combination with flexure mechanisms can reach large strokes and only consume power when moving [124]. Since the electric field yields a negative lateral stiffness, electrostatic actuators can suffer from instability if the positive mechanical stiffness of the flexure mechanism or the individual comb fingers is not sufficient. For large deflections, and thus high voltages, the result is pull-in [80].

Adding feedback control, and thus a position sensor, can enhance the perfor-

mance of positioning systems. Position and acceleration sensing in MEMS is often based on the varying electrical capacitance between a static reference and an actuated stage [76, 77, 22]. Although a capacitive sensor can be 'easily' integrated in a single fabrication process with electrostatic actuators, the disadvantage of accurate and long-range capacitive displacement sensors is the large required wafer surface area. Some alternative sensors use integrated optical waveguides [9], the piezoresistive effect [84, 30], or varying thermal conductance [78, 26, 105]. However, these sensors require multiple fabrication steps and/or manual assembly with respect to the moving stage.

In literature several multiple degrees-of-freedom (DOF) stages are reported. For example De Jong et al. [28] and Mukhopadhyay et al. [91] show very similar 3DOF stages for in-plane motion. A six-axis compliant mechanism is presented by Chen and Culpepper [17], which consists of three pairs of two-axis thermomechanical actuators. A very compact electrostatic stepper platform is presented by Sarajlic et al. [113], capable of 2DOF movement. However, these stages do not include position sensing. Positioning stages with integrated feedback do also exist [22, 79, 108]. These stages require complicated fabrication schemes and assembly or offer relative small stroke.

1.2 Objectives

In the previous section the opportunities for MEMS manipulators and the disadvantages of existing stages are discussed. In this scope the objective of this work is formulated as *the development of a large-stroke closed-loop positioning system using a simple fabrication scheme and no assembly.* By developing such a positioning system, we gain insight into and knowledge of MEMS. This is formulated in a second, broader objective as *understanding the opportunities and limitations of positioning and manipulation in MEMS for use in future mechatronic applications.*

The positioning stage in this work should be able to move in three degrees-of-freedom (DOFs): x, y, and R_z. With respect to the existing stages we want the integration of a position sensor to decrease the influence of external disturbances and load forces, a large stroke in combination with a compact size to enable new applications and the integration of the complete system in a simple fabrication scheme. Especially the integration of the complete system without assembly can have major benefits with respect to cost and performance. Many high-tech applications need a vacuum environment to function correctly, like mass spectrometers, EUV or electron based lithography machines, and electron microscopes. Therefore it is interesting to investigate how a MEMS-based positioning stage will perform in a vacuum environment.

Summarizing, the goals of this research are:

- The design of a MEMS-based positioning stage for in-plane motion.
- The extension of the stroke with respect to currently available MEMS stages.
- Addition of a position sensor in the system to provide feedback.

- Integration of the complete system in a simple fabrication scheme without the use of assembly.
- Characterization of the system components in a vacuum environment.

1.3 Outline

The first chapters of this thesis focus on design and characterization of different components for a single-DOF system. These components are actuation, sensing, and control. The single-DOF shuttles are kinematically coupled into a 3DOF stage, described in the last chapter of this thesis and shown in Figure 1.1.

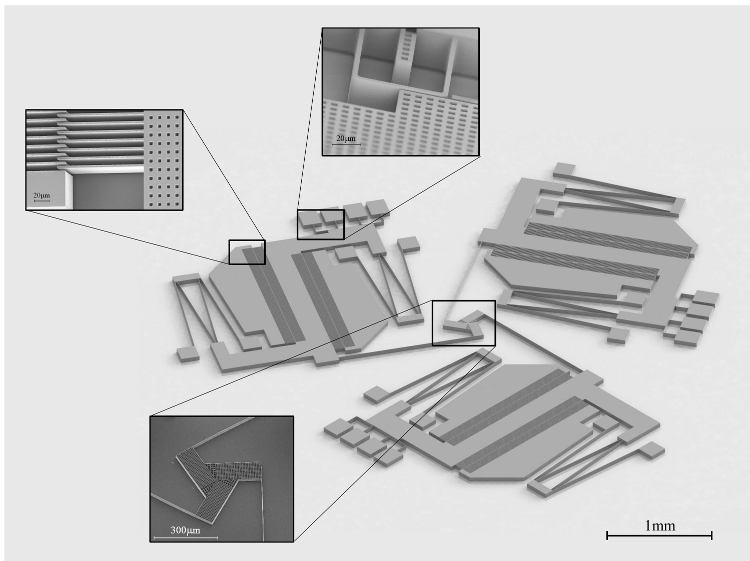

Figure 1.1: An overview of the closed-loop 3DOF stage. Actuation (top left), sensing (top center) and kinematic coupling (bottom left) are emphasized by scanning electron microscopy images of the fabricated system.

Electrostatic comb-drives can suffer from instability for large deflections. Instability can occur for the complete flexure mechanism as well as for individual comb-drive fingers. **Chapter 2** describes the optimization of several flexure mechanisms for large displacements actuated by comb-drives. **Chapter 3** analyzes pull-in of individual comb-drive fingers, for both perfectly aligned and slightly deflected (misaligned) fingers[1].

[1] The author of this thesis, Bram Krijnen, is not the first author of chapter 3. The contribution of Bram Krijnen was the design of the test structures, the finite element modelling and the measurement of the deflection curves and limit point voltages. The analytical and numerical model and the writing of the article was done by Jaap Meijaard.

In **chapter 4** a position sensor that can be easily integrated with the flexures as described in the previous chapters is shown. This sensor consists of two silicon heaters that are resistively heated. Heat is conducted through air towards the 'cold' stage and therefore the temperature of the heaters changes when the stage position and thus the overlap changes. This results in a measurable change in the electrical resistance of the heaters. For applications in a vacuum environment, the sensor response will drop since the air is removed. The effect of a vacuum environment on the sensor response and the resulting consequences for position control are investigated in **chapter 5**.

Finally, the three single-DOF shuttles with thermal position sensors for feedback are coupled to form a parallel kinematic 3DOF stage. The results are presented in **chapter 6**.

Provided as additional information are

- **Appendix A: Process Description**, the appendix provides a schematic overview of the fabrication process used for all of the devices described in this thesis, and
- **Appendix B: Images**, the appendix shows images of the fabricated structures in this work. Most of the images are made using a scanning electron microscope (SEM).

All chapters in this thesis have been or will be submitted as journal articles. At the moment of writing, Chapter 2, 3, and 4 are published. Chapter 5 is submitted for publication and Chapter 6 will be submitted for publication soon.

Chapter 2

Flexures for large stroke electrostatic actuation in MEMS

The stroke of a MEMS stage suspended by a flexure mechanism and actuated by electrostatic comb-drives is limited by pull-in. A method to analyze the electrostatic stability of a flexure mechanism and to optimize the stroke with respect to the footprint of flexure mechanisms is presented. Four flexure mechanisms for large stroke are investigated; the standard folded flexure, the slaved folded flexure, the tilted folded flexure and the Watt flexure. Given a certain stroke and load force, the flexures are optimized to have a minimum wafer footprint. From these optimizations it is concluded that the standard folded flexure mechanism is the best flexure mechanism for relatively small strokes (up to $\pm 40\,\mu m$*) and for larger strokes it is better to use the tilted folded flexure. Several optimized flexure mechanisms have been fabricated and experimentally tested to reach a stroke of* $\pm 100\,\mu m$*. The displacement of the fabricated stages as a function of the actuation voltage could be predicted with 82% accuracy, limited by the fairly large tolerances of our fabrication process.*

This chapter is published as 'B. Krijnen and D.M. Brouwer. Flexures for large stroke electrostatic actuation in mems. *Journal of Micromechanics and Microengineering*, 24(1):015006, 2014'.

2.1 Introduction

Thermal or electrostatic actuators are typically used for the actuation of a stage in MEMS. The drawbacks of thermal actuators are the relatively large time constant, therefore the limited actuation bandwidth, and the relatively high power consumption [23, 47, 102]. Flexure-based designs are commonly used to increase the positioning repeatability due to the lack of friction, hysteresis and play [120, 51, 55, 119]. Electrostatic comb-drive actuators in combination with flexure mechanisms can reach large strokes and do not consume a constant power [124]. For electrostatic comb-drive actuation the lateral movement of a stage needs to be constrained, since comb-drive actuators suffer from lateral instability due to electrostatic pull-in [80]. The voltage applied to the electrostatic comb-drive actuator results not only in a force in the actuation direction, but also in forces in the lateral direction. An exact straight-line guidance mechanism is symmetrically loaded by the electrostatic field, in which case the problem reduces to a pure bifurcation problem. A critical voltage and a maximum stage displacement can be determined, after which pull-in occurs. Alternatively, imperfect straight-line guidance mechanisms will get an additional lateral displacement due to the asymmetric electrostatic loading. The resulting electrostatic force is compensated for by the mechanical force from the flexure. In the stable operating range a smooth curve of equilibria is found. Pull-in occurs when no such equilibrium exists.

A commonly used flexure mechanism in MEMS consists of two nested parallelograms and is often referred to as the folded flexure mechanism [124, 80, 43]. The folded flexure combines a low actuation stiffness $K_{x,\mathrm{m}}$ with a high lateral stiffness $K_{y,\mathrm{m}}$ in the undeflected state. However, the stiffness ratio $K_{y,\mathrm{m}}/K_{x,\mathrm{m}}$ decreases rapidly for increasing displacements in the actuation direction. Legtenberg et al. [80] report displacements up to $\pm 40\,\mu\mathrm{m}$ using folded flexures. Zhou and Dowd [131] and Grade et al. [43, 44] use prebent folded flexures to reach only single-sided displacements of $61\,\mu\mathrm{m}$ and $175\,\mu\mathrm{m}$, respectively. Hou et al. [54] demonstrate the extension of the stable deflection range of an electrostatically driven flexure mechanism by adding a second comb-drive actuator without initial overlap between stator and stage. An extension of the stable deflection range from $\pm 61\,\mu\mathrm{m}$ to $\pm 86\,\mu\mathrm{m}$ is shown. Chen and Lee [15] show by simulations that tilting the leafsprings of the folded flexure mechanism inwards does increase the maximum stable travel range, which is validated by measurements in [98]. A displacement of $\pm 149\,\mu\mathrm{m}$ was reached. Olfatnia et al. [99] present a flexure mechanism that constrains the degree of freedom (DOF) of the intermediate body in the folded flexure mechanism. This directly results in an increase of the lateral stiffness and therefore of the stable travel range. They report displacements up to $245\,\mu\mathrm{m}$. Brouwer et al. [12] constrain the DOF of the intermediate body in the folded flexure by adding a 1:2 lever and introduce the Watt flexure in MEMS. Displacements of $\pm 100\,\mu\mathrm{m}$ are reported for both flexure mechanisms.

Previous work compares flexure designs basically on the maximum displacement that is reached. For example, Olfatnia et al. [99] plot the maximum dis-

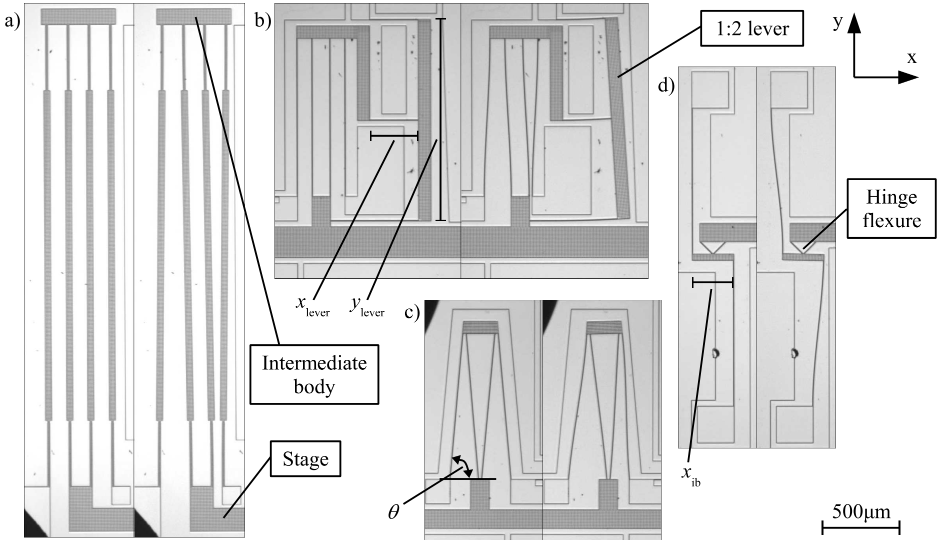

Figure 2.1: The four flexure mechanisms that have been studied in this work are shown. The optical microscope images of the fabricated devices show the flexure mechanism in nominal state (left) and in deflected state (right): a) the folded flexure, b) the slaved folded flexure, c) the tilted folded flexure and d) the Watt flexure. The movable stages and intermediate bodies look darker in the images due to the perforation, to release them from the underlying handle wafer. Apart from the leafspring length l_l and thickness t_l, the parameters used for optimization are given.

placement of several flexure mechanisms as a function of the leafspring length, the actuation voltage and the number of comb-drive fingers. However, the compared systems have different design constraints such as the maximum allowed voltage and minimum feature size. And due to the existence of compounded flexures, the use of leafspring length does not lead to a representative criterion. Brouwer et al. [12] optimize several flexure mechanisms with equal system requirements and design constraints using a criterion that includes the maximum displacement, an additional load force and the required device footprint. Although a fair comparison can be made for a single range of motion and load force combination, it is not valid for others.

In this work we present a method to optimize flexure mechanisms based on equal design constraints and based on equal required displacement and load force. For a wide range of required strokes and load forces, we will minimize the footprint area of the folded flexure, the tilted folded flexure, the slaved folded flexure and the Watt flexure. Figure 2.1 shows the four flexure mechanisms. For each specific combination of pull-in stroke and load force the 'best' flexure mechanism is chosen; this is the flexure mechanism that requires the smallest wafer footprint. The main contributions of this paper are 1) a generic method to compare four representative

flexure mechanisms using equal design constraints and requirements, 2) including the load force as a requirement in the optimization, 3) the true footprint criterion to optimize flexures mechanisms, and 4) a comprehensive, graphical presentation of the optimization results in a chart.

2.2 Method

The model that is used to calculate the pull-in of a flexure mechanism actuated by a comb-drive is presented in Section 2.3. This model combines a multibody mechanical analysis and an analytic electrostatic analysis. Then, in Section 2.4, simulation results are given on which flexure to use when a specified displacement and load force are required. Four flexure mechanisms are included in this study; the folded flexure, the tilted folded flexure, the slaved folded flexure and the Watt flexure. These flexure mechanisms are introduced in Section 2.4.1 and graphically shown in Figure 2.8. The behavior of the flexure mechanisms with equal leafspring length and equal leafspring thickness is compared and given in Section 2.4.2. Additionally, in this section our multibody models are verified using FEM simulations. Both are shown in Figure 2.6. The criterion to optimize our flexure mechanisms is introduced in Section 2.4.3. This criterion simply is the (estimated) wafer footprint that the flexures and the actuator will require. For example, a flexure with short leafsprings will lead to a small flexure area, but is relatively stiff. This will require a large actuation force and therefore a large number of comb-drive fingers. A large number of comb-drive fingers results in a large actuator area. So short leafsprings will not automatically lead to a smaller wafer footprint of the complete stage. The results of the optimization for wafer footprint are given in Section 2.4.4. This basically shows which of the four flexure mechanisms requires the smallest footprint for a specified displacement and load force, graphically given in Figure 2.10. To validate our models, measurements are performed on all four flexure mechanisms. The chosen designs are capable of making a displacement of $\pm 100\,\mu m$ with an additional load force of $50\,\mu N$ in actuation direction. The designs are given in Table 2.3. Section 2.5 provides more information on the design constraints and the fabrication process. The measurement of the displacement as a function of the actuation voltage is given in Section 2.6. Although our attempts to measure the additional load force failed, the measurements did confirm our mechanical as well as electrostatic model.

An overview of an electrostatically comb-drive actuated stage with two tilted folded flexures is given in Figure 2.2. Since a single flexure mechanism does not properly constrain the in-plane rotation of the stage, two flexure mechanisms are used. A comb-drive actuator can only provide attracting forces, so in order to move in positive as well as negative x-direction two actuators are required. All flexure mechanisms presented in this work are symmetrical and bidirectional, meaning that their behavior is equal in positive and negative x-direction. All components of the system are designed to be integrated in the device layer of a silicon-on-insulator wafer (SOI-wafer) with a single-mask fabrication process.

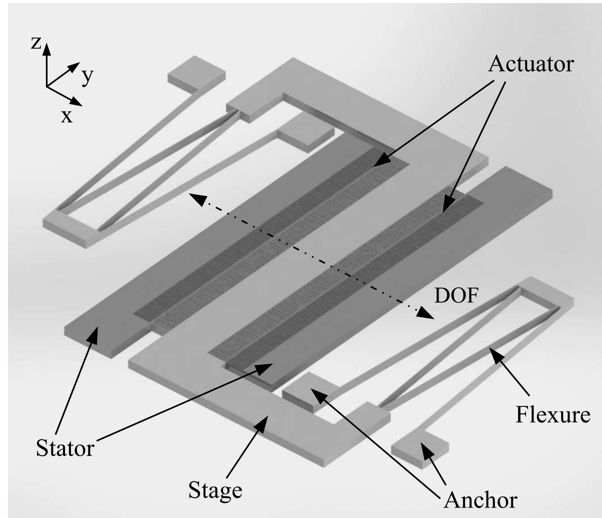

Figure 2.2: An overview of an electrostatically comb-drive actuated stage with a tilted folded flexure mechanism is given. The anchors on both sides of the stage stay mechanically connected to the handle wafer through the buried oxide layer. The stage with flexure mechanism and anchors (light gray) are electrically isolated from the stators (dark gray).

2.3 Pull-in theory

The model to analyze pull-in of a flexure mechanism with an electrostatic actuator basically consists of two steps, 1) the mechanical analysis of the flexure mechanism (Section 2.3.2) and 2) the electrostatic stability analysis based on the mechanical characteristics of the flexure mechanism (Section 2.3.3). First, Section 2.3.1 describes that the mechanical and the electrostatic analysis can be performed sequentially.

2.3.1 Iterative model

The electrostatic field generated by a voltage on the comb-drive actuator results in a force in the actuation direction, $F_{x,\mathrm{e}}$, and forces in the lateral direction, $F_{y,\mathrm{e1}}$ and $F_{y,\mathrm{e2}}$. These forces are schematically given in Figure 2.3. The phenomenon that the electrostatic force in y-direction increases faster than the counteracting mechanical force due to the lateral stiffness of the flexure mechanism is called pull-in. The displacement in x-direction for which this phenomenon first occurs is called the pull-in stroke s.

The electrostatic stability of the flexure mechanism can be determined analytically; this will be described in Section 2.3.3. The electrostatic analysis requires characteristics of the flexure mechanism: the restoring force of the flexure mech-

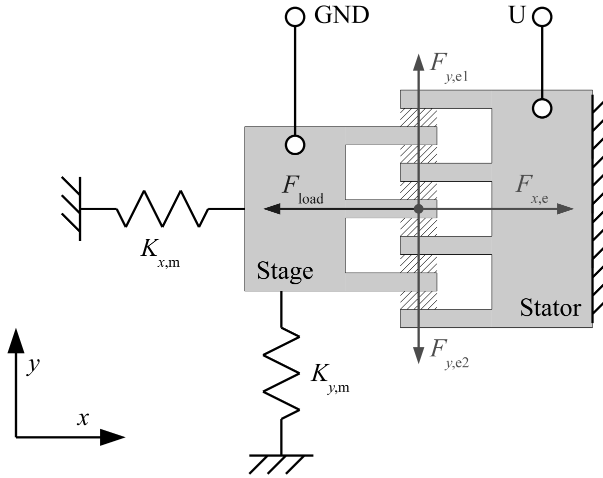

Figure 2.3: A schematical overview of a comb-drive actuator with flexure mechanism is given. Mechanical stiffnesses ($K_{x,\mathrm{m}}$ and $K_{y,\mathrm{m}}$) as well as electrostatic forces ($F_{x,\mathrm{e}}$, $F_{y,\mathrm{e1}}$ and $F_{y,\mathrm{e2}}$) due to the applied voltage U are indicated. The load force F_{load} acts in opposite direction to the actuation force $F_{x,\mathrm{e}}$. Rotation of the stage is constrained by the flexure mechanism.

anism acting on the stage $F_{x,\mathrm{m}}$, the trajectory of the stage in lateral direction without additional load forces y_{m} (for imperfect straight-line guidances), and the lateral stiffness $K_{y,\mathrm{m}}$. These mechanical properties are functions of the stage displacement x. For a stage displacement an actuation force is required that is generated by applying an actuation voltage. The actuation voltage will also introduce lateral electrostatic forces onto the stage. For an imperfect straight-line guidance mechanism the intrinsic displacement y_{m} will be magnified by the lateral electrostatic forces and will introduce an additional displacement y_{e}. The total lateral displacement y then becomes $y = y_{\mathrm{m}} + y_{\mathrm{e}}$.

The additional lateral electrostatic force $F_{y,\mathrm{e}}$ due to a lateral displacement influences the lateral stiffness $K_{y,\mathrm{m}}$ and the x displacement of the stage, as shown in [7]. Thus the lateral electrostatic force should be used as an input for the mechanical analysis, schematically given in Figure 2.4. By iteration towards a stable solution, the pull-in stroke of the flexure mechanism is determined. However, the lateral electrostatic force is relatively small and does hardly affect the lateral stiffness of the flexure mechanism. Simulations show deviations of less than 1% in pull-in stroke by including or omitting iteration in our simulations. Therefore iterations that deal with the variation in lateral stiffness in the presence of a lateral force are omitted in our simulations.

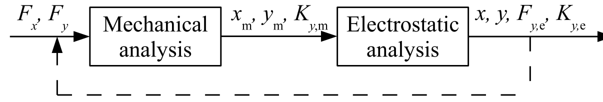

Figure 2.4: The method to analyze pull-in basically consists of two steps, 1) the mechanical analysis of a flexure mechanism and 2) the electrostatic analysis based on the mechanical characteristics of the flexure mechanism. The additional lateral electrostatic force $F_{y,\mathrm{e}}$ should be used as an input for the mechanical analysis. When iteration is omitted, simulations show deviations of less than 1%.

2.3.2 Mechanical analysis

The relevant mechanical characteristics required for the electrostatic stability analysis are the restoring force $F_{x,\mathrm{m}}$, the lateral displacement y_{m}, and the lateral stiffness $K_{y,\mathrm{m}}$ of the flexure mechanism as a function of the x-displacement. Although the MEMS are planar devices, the characteristics are determined using spatial mechanics, since out-of-plane bending and torsion can easily lead to pull-in or stiction. Basically three methods exist for solving force-displacement relations: FEM, multibody and analytical. Awtar [7], for example, shows a closed-form expression for the folded flexure and the tilted folded flexure, both in planar mechanics. The analytical model does not include the compliance of the stage and cannot be directly used for other flexure mechanisms, like the slaved folded flexure and the Watt flexure. Flexures mechanisms can also be modeled using readily available FEM software packages. However, due to the many elements necessary for accurate results, the model changes which cause rigid body motion, and the geometric non-linear effects of flexure mechanisms undergoing large deflections, FEM simulations are time consuming computations. For optimization, where many of such computations are necessary, computationally efficient models that are capable of capturing the relevant dynamic and compliant characteristics over the full range of motion are crucial. A multibody modeling method allows a limited number of elements which are invariant for arbitrary rigid body motion facilitating fast and accurate simulations. The authors choose to use SPACAR, since it is a relatively fast, multibody program that is capable of spatial mechanics simulations [62, 85, 87, 129]. The SPACAR simulations of different flexure mechanisms are verified by FEM calculations; these results will be given in Section 2.4.1.

2.3.3 Electrostatic analysis

Due to the chosen geometry of the stage, with a relatively large span in between the flexures, the rotation of the stage is small. For this reason we only look at pull-in as a function of the stage position in x and y. The electrical capacitance

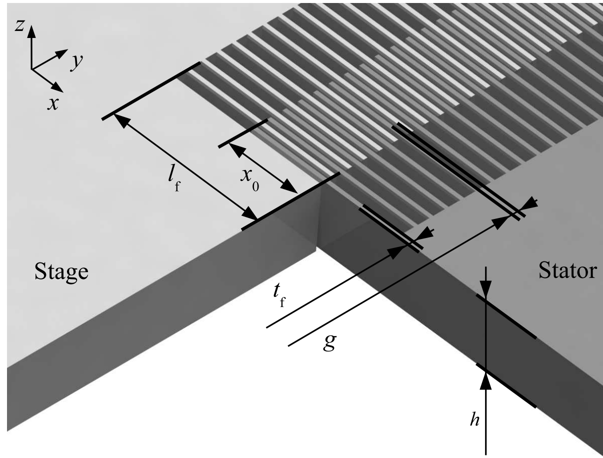

Figure 2.5: The figure shows the parameters of the comb-drive actuator. In the actual design the stage is perforated.

of a comb-drive as a function of the stage position is given by

$$C(x, y) = N\epsilon_0\epsilon_\mathrm{r}h(x_0 + x)\left(\frac{1}{g-y} + \frac{1}{g+y}\right), \tag{2.1}$$

where N is the number of comb-drive finger pairs, ϵ_0 is the vacuum permittivity of $8.854 \times 10^{-12}\,\mathrm{Fm}^{-1}$, ϵ_r is the relative permittivity of air of 1.001, h is the height of the structures, x_0 is the initial overlap of the comb-drive fingers and g is the symmetric air gap between the comb-drive fingers. The geometric properties of the comb-drive are given in Figure 2.5.

The potential energy in the comb-drive actuator is a sum of the mechanical and the electrical energy, as a function of x, y and the electric charge q,

$$\begin{aligned} E(x, y, q) &= E_\mathrm{m}(x, y) + E_\mathrm{e}(x, y, q) \\ &= \frac{1}{2}K_{x,\mathrm{m}}x^2 + \frac{1}{2}K_{y,\mathrm{m}}(y - y_\mathrm{m})^2 + \frac{1}{2}\frac{q^2}{C(x, y)}. \end{aligned} \tag{2.2}$$

$K_{x,\mathrm{m}}$ and $K_{y,\mathrm{m}}$ are the mechanical actuation and lateral stiffnesses, both results of the mechanical analysis given in Section 2.3.2. Equation (2.2) can be rewritten to the complementary energy E' in which the electrical charge q is replaced by the actuation voltage U

$$E'(x, y, U) = \frac{1}{2}K_{x,\mathrm{m}}x^2 + \frac{1}{2}K_{y,\mathrm{m}}(y - y_\mathrm{m})^2 - \frac{1}{2}C(x, y)U^2. \tag{2.3}$$

The external forces acting on the stage are given by the negative partial derivatives of the complementary energy with respect to x and y [80]. Since the stage can be used to manipulate an end-effector or simply to apply a force, an additional

load force in actuation direction is added to the force equilibrium in x-direction, graphically given in Figure 2.3. The static equilibria to describe the behavior of the comb-drive actuator suspended by a flexure mechanism are

$$\sum F_x = -\frac{\partial E'(x,y,U)}{\partial x} - F_{\mathrm{load}} = 0 \tag{2.4a}$$

$$\sum F_y = -\frac{\partial E'(x,y,U)}{\partial y} = 0. \tag{2.4b}$$

Combining (2.1), (2.3), and (2.4a) leads to the force equilibrium in actuation direction in which the actuation voltage U appears,

$$F_{x,\mathrm{m}} + F_{\mathrm{load}} = \frac{N\epsilon_0\epsilon_{\mathrm{r}}hU^2}{g}. \tag{2.5}$$

The influence of y is omitted in this equation, since small displacements in y-direction, roughly below 10% of the gap g, influence the electrostatic actuation force less than 1%. The first term in this equation corresponds to the restoring force of the flexure mechanism acting on the stage. The second term is the additional load force. The third term is the required electrostatic actuation force to establish the equilibrium. Equation (2.5) is used to calculate the required actuation voltage to reach a displacement or to apply a load force,

$$U_{\mathrm{req}} = \left(\frac{g(F_{x,\mathrm{m}} + F_{\mathrm{load}})}{N\epsilon_0\epsilon_{\mathrm{r}}h}\right)^{1/2}. \tag{2.6}$$

The required actuation voltage U_{req} is used to analyze the lateral electrostatic forces and thereby the lateral stability of the flexure mechanism. Combining (2.1), (2.3), and (2.4b) leads to the force equilibrium in y-direction,

$$-K_{y,\mathrm{m}}(y - y_{\mathrm{m}}) + \frac{1}{2}N\epsilon_0\epsilon_{\mathrm{r}}h(x_0 + x)U_{\mathrm{req}}^2\left(\frac{1}{(g-y)^2} - \frac{1}{(g+y)^2}\right) = 0. \tag{2.7}$$

From this equation it can be seen that when the stage is perfectly aligned ($y = 0$) over the complete stroke, no mechanical and electrostatic force in lateral direction will occur, irrespective of the applied actuation voltage. However, perfect straight guidance mechanisms do not exist, since there will always be offsets due to fabrication inaccuracies. So the static solution for y that can be calculated from (2.7) must be a stable equilibrium; there must be a minimum in the complementary energy. A minimum in the complementary energy exists when the second-order partial derivative of the complementary energy with respect to y is positive,

$$\sum K_y = \frac{\partial E'(x,y,U)^2}{\partial^2 y} > 0. \tag{2.8}$$

Combining (2.1), (2.3), and (2.8) leads to the stiffness criterion for stability, also presented in [15],

$$K_{y,\mathrm{m}} - N\epsilon_0\epsilon_{\mathrm{r}}h(x_0 + x)U_{\mathrm{req}}^2\left(\frac{1}{(g-y)^3} + \frac{1}{(g+y)^3}\right) > 0. \tag{2.9}$$

The second term in this equation is called the 'electrostatic stiffness' $K_{y,\mathrm{e}}$. The electrostatic stiffness has an opposite sign with respect to the lateral mechanical stiffness $K_{y,\mathrm{m}}$ and is therefore seen as a strongly non-linear, negative stiffness. Equation (2.7) and (2.9) lead to the same non-trivial solution for the pull-in stroke of a flexure mechanism with electrostatic actuation. Since the lateral displacement y_m of the flexure mechanism never is exactly zero due to loads or inaccuracies, (2.7) suffices for the electrostatic stability analysis. To obtain a fifth-order polynomial equation in standard form, (2.7) is multiplied by $(g-y)^2(g+y)^2$ and reordered. The roots of the polynomial equation are calculated; one of the roots of this equation is the equilibrium solution for the displacement in y.

2.4 Flexures and optimization

Several linkages have been evaluated for use as a flexure mechanism in MEMS. We considered a double four-bar linkage, a slaved double four-bar linkage, Roberts' linkage, Watt's linkage, Chebyshev's linkage, Peaucellier's linkage, Hoeken's linkage Bricard's linkage and Evans' linkage. We found Peaucellier's and Bricard's linkage too complex to transform into a MEMS flexure. Chebyshev's linkage is incompatible with the single device layer we intend to use. Evans' and Hoeken's linkage have the disadvantage of a relatively small stroke compared to their size. Therefore we investigate the double four-bar linkage, the slaved double four-bar linkage, Roberts' linkage and Watt's linkage. Converted to MEMS these linkages are also known as the folded flexure (FF), the slaved folded flexure (SFF), the tilted folded flexure (TFF) and the Watt flexure. An overview of these four flexure mechanisms in nominal and in deflected states is given in Figure 2.1.

2.4.1 Flexure mechanisms

As a general geometry for our stages we have chosen to use two flexure mechanisms with a relatively large span, as shown in Figure 2.2. The large span offers two advantages. First, the influence of the rotational stiffness of the single flexures is small compared to the influence of the lateral stiffness. Second, the rotation of the stage due to a lateral displacement of an imperfect straight-line flexure is negligable. For example, a lateral displacement of 1 µm with a flexure span of at least 1000 µm results in a rotation of less than 1 mrad. Pre-bended and pre-tilted flexure mechanisms are known from literature to increase the single-sided stroke of a flexure mechanism [43, 131, 44]. The use of such asymmetrical flexures can be beneficial in terms of wafer footprint since only one actuator has to be used. However, the comb-drive fingers need to be twice as long and the actuation force needs to be twice as high. The comb-drive fingers, as well as the complete flexure mechanisms, suffer from electrostatic pull-in, as described in [35, 88]. Rough calculations show that either increasing the number of comb-drive fingers or increasing the actuation voltage and the finger thickness both result in

an increase of the actuator area of at least a factor of 1.33. For this reason we have not included asymmetrical flexure mechanisms in our optimization.

The folded flexure is a double parallelogram flexure mechanism [124]. The lateral movement of the intermediate body due to the outer parallelogram flexure is canceled by the inner parallelogram flexure. Theoretically this results in a perfectly straight-guided stage. The mechanical stiffness in the actuation as well as in the lateral direction of the folded flexure mechanism is analytically given by Legtenberg [80]. In the actuation direction the mechanical stiffness is more or less constant if the deflection is small compared to the leafspring length [11]. In the lateral direction, the folded flexure suffers from a large decrease in the stiffness when the flexure is in a deflected state. This is caused by the internal DOF of the intermediate body in the x-direction, described among others in [7, 61]. According to the coordinate system defined in Figure 2.1, when the stage is deflected in positive x-direction, a positive y-force on the stage causes an extra force in negative x-direction on the intermediate body. The intermediate body will easily deflect due to the internal DOF and as such causes a deflection in lateral direction. This deflection causes the decrease in lateral stiffness. For optimization, the leafspring length l_l and leafspring thickness t_l of the folded flexure are varied.

The slaved folded flexure as well as the tilted folded flexure constrain the intermediate body of the folded flexure. The slaved folded flexure uses a 1:2 lever to constrain the deflection of the intermediate body to half of the deflection of the stage, which has been shown for example in [61, 59]. The lever length y_lever and lever leafspring length x_lever do influence the mechanical behavior of the flexure mechanism. A short lever and short lever leafsprings lead to a high additional stiffness in the actuation direction, whereas a long lever and long lever leafsprings result in an increase in footprint. For practical (design) reasons the minimum lever length is chosen to be the flexure leafspring length l_l. Simulations prove that this minimum lever length does lead to the minimum footprint device. Therefore, the lever length is always set equal to the flexure leafspring length in our optimization. The lever leafspring length x_lever is included in our optimization.

A second way to constrain the deflection of the intermediate body in the folded flexure is by tilting the outer leafsprings slightly inwards. Tilting these leafsprings will result in a rotation of the intermediate body. To release the stage rotation from the rotation of the intermediate body, the inner leafsprings of the flexure need to be tilted as well. The result is the tilted folded flexure, which is described analytically by Awtar [7]. As mentioned before, two tilted folded flexure mechanisms are used to properly constrain the rotation of the stage. In this way the intermediate body of a each tilted folded flexure is kinematically constrained by two centers of rotation which are not coincident. A tilt angle of 90° corresponds to the folded flexure with parallel leafsprings. Simulations prove that an angle of 85° already increases the pull-in stroke significantly. The tilt angle θ of the leafsprings is used as a parameter in the optimization.

The fourth flexure mechanism that is included in this study is the Watt flexure. The intermediate body of the Watt flexure also rotates for deflections of the stage. An extra hinge flexure is added to decouple the rotation of the intermediate body

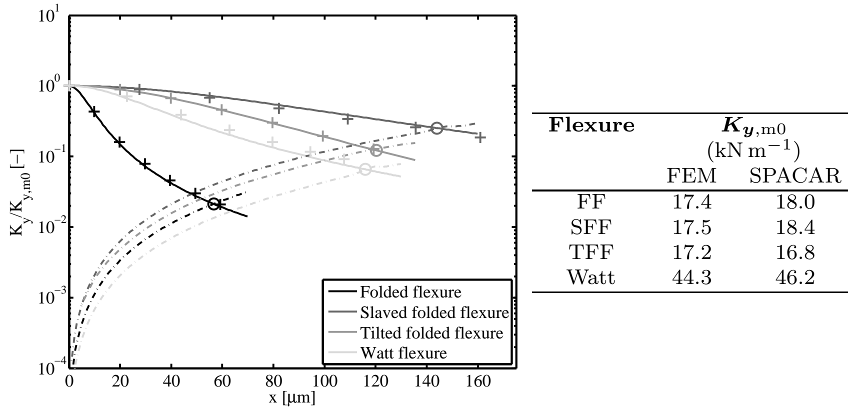

Flexure	$\boldsymbol{K_{y,\mathrm{m0}}}$ (kN m^{-1})	
	FEM	SPACAR
FF	17.4	18.0
SFF	17.5	18.4
TFF	17.2	16.8
Watt	44.3	46.2

Figure 2.6: The flexure mechanisms are compared in lateral stiffness when using an equal leafspring length of 1000 µm and an equal leafspring thickness of 3 µm. The continuous lines show the lateral mechanical stiffness of the four flexure mechanisms as a function of the deflection x, the dash-dotted lines indicate the (negative) lateral electrostatic stiffness. For normalization the mechanical stiffness as well as the electrostatic stiffness are divided by the lateral mechanical stiffness at zero deflection $K_{y,\mathrm{m0}}$. The intersection between the continuous and the dash-dotted line is the deflection at which flexure pull-in occurs, indicated by the circles. The lateral mechanical stiffness of the flexure mechanisms is verified by FEM calculations, indicated by the markers in the graph. The lateral mechanical stiffness at zero deflection of the flexures is given in the table next to the figure, for the FEM as well as the SPACAR simulations.

from the stage. In the Watt flexure the width of the intermediate body x_{ib} is used as an input for the optimization. The leafsprings of the hinge flexure are chosen as large as possible with regard to the width of the intermediate body. Increasing the width of the intermediate body will lead to smaller rotations of the intermediate body and therefore less deflection of the hinge flexure leafsprings. This results in a lower and more linear actuation stiffness, at the cost of a larger footprint.

2.4.2 Model verification

In the case that the leafspring length l_{l} is chosen to be 1000 µm and the leafspring thickness t_{l} is chosen to be 3 µm, for all flexure mechanisms the pull-in stroke is calculated and given in Figure 2.6. The solid lines show the lateral mechanical stiffness of the various flexure mechanisms calculated with SPACAR, the dash-dotted lines show the absolute value of the lateral electrostatic stiffness as given in (2.9). The stiffnesses in the graph are normalized towards the initial lateral mechanical stiffness $K_{y,\mathrm{m0}}$, which is given in the table next to the figure. The lateral mechanical stiffness of the flexure mechanisms is verified using FEM calculations

with Solidworks Simulation using a non-linear, large deflection study with a solid mesh [118]. The FEM results agree within 15% with the SPACAR calculations and are added as markers in Figure 2.6.

The lateral mechanical stiffness of the folded flexure decreases the fastest of all four flexure mechanisms when in a deflected state. This leads to pull-in at a stroke of ±57 µm. The flexure mechanisms in this study are symmetrical around zero deflection, so a pull-in stroke of ±57 µm in fact means a total stroke of 114 µm. From the low normalized lateral electrostatic stiffness of the Watt flexure (with $x_{\mathrm{ib}} = 500\,\mu\mathrm{m}$) we can conclude that this mechanism has the highest stiffness ratio $K_{y,\mathrm{m}}/K_{x,\mathrm{m}}$. This leads to a higher pull-in stroke than for the folded flexure, ±117 µm. At the cost of extra actuation stiffness, the slaved folded flexure (with $x_{\mathrm{lever}} = 500\,\mu\mathrm{m}$) and the tilted folded flexure (with $\theta = 85°$) give less decrease in lateral mechanical stiffness and therefore higher pull-in strokes, ±145 µm and ±119 µm respectively.

The basic parameters that can be varied to change the pull-in stroke of a flexure mechanism are the leafspring length l_{l} and thickness t_{l}. For the folded flexure mechanism the influence of the leafspring length and thickness is given in Figure 2.7; the other flexure mechanisms react similarly to a change in the leafspring length and thickness. For each leafspring thickness a leafspring length exists for which the pull-in stroke is at its maximum. When the leafspring thickness increases, the pull-in stroke will also increase. However, an increasing leafspring thickness also leads to a higher stiffness in actuation direction, which results in extra comb-fingers when the actuation voltage is limited. To obtain a ±100 µm stroke with a load force of 50 µN the leafspring thickness of the folded flexure needs to be at least 11 µm.

2.4.3 Wafer footprint

We will optimize the flexure mechanisms based on an estimation of the required wafer footprint. We are aware that any area estimation is open for discussion. For example, simply taking the 'bounding box' area overestimates the actual device footprint. Furthermore we have chosen to exclude anchor points and parts of the stage, since these areas rely heavily on limitations of the fabrication process. As a result we use the sum of the area of the flexure mechanism A_{flex} and the area of the electrostatic actuator A_{act} as the wafer footprint, both given in Table 2.1. The area of the flexure mechanism is expressed as a function of the parameters of the flexure. The area of the actuator is calculated as a function of the number of comb-fingers, the width of the comb-fingers and the width of the air gap between the comb-fingers. A safe maximum actuation voltage is chosen to be 80 V, to prevent pull-in of individual comb-drive fingers for displacements up to ±150 µm, as described in [35, 88]. The value for the maximum actuation voltage is used to calculate the number of comb-fingers N using equation (2.5) and as such influences the area of the actuator. A graphical representation of the area estimation of the four flexure mechanisms with actuators is given in Figure 2.8. The blue rectangles

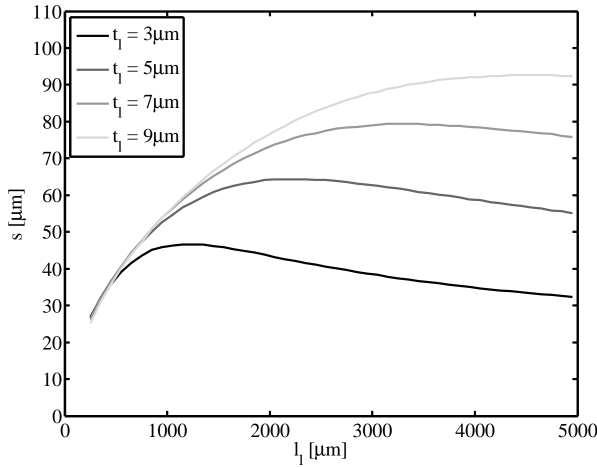

Figure 2.7: The influence of the leafspring length l_l and leafspring thickness t_l of the folded flexure on the pull-in stroke is given. For the other flexure mechanisms the influence of the leafspring length and thickness is similar (although on another scale). A load force of 50 µN is applied in this plot.

give the area of the flexure mechanisms, the red rectangles show the actuator required for the actuator.

The initial comb-drive finger overlap x_0 has been chosen to be 10 µm and the height of the structures h equals the thickness of the device layer, 50 µm. The minimum feature size and the minimum trench width are both limited to 3 µm in our fabrication process, which constrains the minimum leafspring thickness t_l, the minimum thickness of the comb-drive fingers t_f and the minimum width of the air gap between the comb-fingers g. Simulations show that increasing the air gap results in a higher pull-in stroke at the cost of a higher actuator area. The lower limit value of 3 µm leads to the flexure mechanisms with the minimum footprint. Comb-drive fingers of 3 µm do not suffer from pull-in with actuation voltages up to

Table 2.1: An estimation of the wafer footprint of the four different flexure mechanisms is made as a function of its parameters. The footprint is the sum of the area of the flexure mechanism A_flex and the area of the electrostatic actuator A_act.

Flexure	$\boldsymbol{A}_\mathrm{flex}$	$\boldsymbol{A}_\mathrm{act}$
Folded Flexure	$2(4s)(l_\mathrm{l})$	$(8s)(2Ng + 2Nt_\mathrm{f})$
Slaved Folded Flexure	$2(4s + x_\mathrm{lever})(l_\mathrm{l})$	$(8s)(2Ng + 2Nt_\mathrm{f})$
Tilted Folded Flexure	$2(4l_\mathrm{l}\cos\theta)(l_\mathrm{l}\sin\theta)$	$(8s)(2Ng + 2Nt_\mathrm{f})$
Watt flexure	$2(2s + x_\mathrm{ib})(2l_\mathrm{l})$	$(8s)(2Ng + 2Nt_\mathrm{f})$

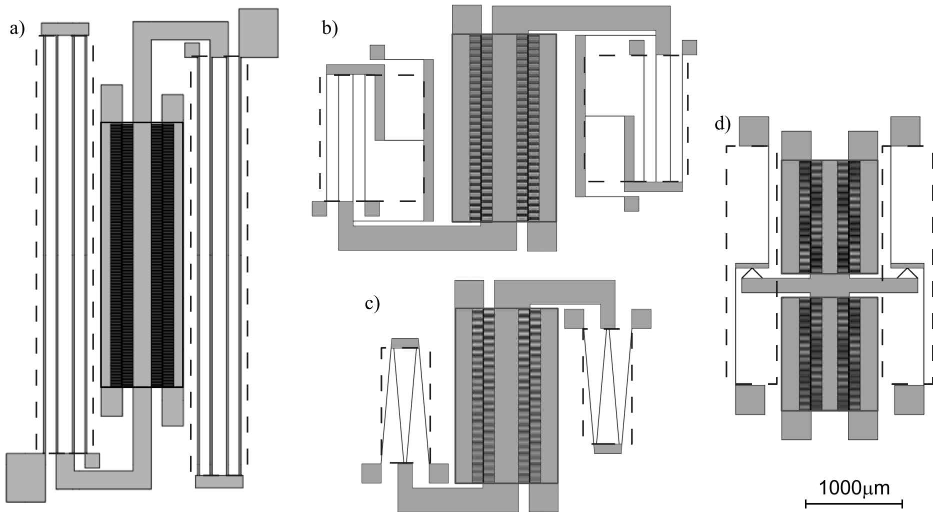

Figure 2.8: A graphical representation of the area estimation of the four flexure mechanisms with actuators is given here. The blue dashed line rectangles give the area of the flexure mechanisms, the red solid line rectangles show the area required for the actuator.

80 V, so there is no need to increase the finger thickness and thereby the (actuator) footprint. Both the air gap g and the finger thickness t_f are set to 3 µm and used as a fixed input for the optimization.

2.4.4 Optimization results

Since the number of parameters for optimization is limited, the mechanical analysis for each flexure mechanism is performed for every combination of input values. The results from the mechanical analysis are used to calculate the pull-in stroke and wafer footprint for each input parameter set. The input parameters that are varied for each flexure mechanism are already discussed in Section 2.4.1 and listed in Table 2.2. Their upper and lower bounds for the optimization are also given.

For each combination of pull-in stroke and load force the parameter set that requires the smallest footprint is chosen as 'optimal' for that flexure mechanism. The resulting footprint for each flexure mechanism is given in Figure 2.9. Each mechanism shows an increase in footprint when the required pull-in stroke or the load force is increased. The maximum leafspring length and maximum leafspring thickness are limited to 2000 µm and 10 µm respectively, based on the limitations of the fabrication process. Using these limitations on the leafspring length and thickness, none of the flexure mechanisms can reach a pull-in stroke of ±200 µm combined with a load force of 600 µN. The load force has limited influence on the pull-in stroke of the folded flexure, but does reduce the pull-in stroke of the other

Table 2.2: For each flexure mechanism the inputs for optimization are listed. The range over which the parameters are varied is also given, as well as the resolution or step size of the optimization.

Flexure	**Input**	**Lower bound**	**Step size**	**Upper bound**
Folded Flexure	l_l	500 µm	100 µm	5000 µm
	t_l	3 µm	1 µm	30 µm
Slaved Folded Flexure	l_l	500 µm	100 µm	3000 µm
	t_l	3 µm	1 µm	10 µm
	x_{lever}	300 µm	100 µm	700 µm
Tilted Folded Flexure	l_l	500 µm	100 µm	3000 µm
	t_l	3 µm	1 µm	10 µm
	θ	70°	2.5°	87.5°
Watt Flexure	l_l	600 µm	100 µm	2000 µm
	t_l	3 µm	1 µm	10 µm
	x_{ib}	300 µm	100 µm	700 µm

flexure mechanisms significantly.

For the specific combination of ±100 µm stroke combined with a load force of 100 µN, our 'optimal' flexure mechanisms result in a wafer footprint of 3.24 mm^2 for the slaved folded flexure, 2.22 mm^2 for the tilted folded flexure and 4.36 mm^2 for the Watt flexure. In Brouwer et al. [12] the designs for similar flexure mechanisms with the same specifications lead to footprints of 3.94 mm^2, 3.33 mm^2 and 7.49 mm^2, respectively. Olfatnia et al. [99] report flexures (only C-DP-DP) with measured strokes ranging from ±119 µm up to ±245 µm. The wafer footprint of these devices is estimated to range from 5.78 mm^2 up to 10.77 mm^2. The tilted folded flexure mechanism from our study to reach a stroke of ±120 µm without an additional load force requires a footprint of 1.01 mm^2 and the slaved folded flexure to reach a stroke of ±200 µm, which was the maximum stroke in our simulations, requires a footprint of 5.68 mm^2. We conclude that the 'optimal' flexure mechanisms from our theoretical study indeed lead to smaller wafer footprints than flexure mechanisms with similar measured displacements from literature.

The areas required by the different flexure mechanisms are compared with each other, leading to the most compact flexure mechanism for each combination of pull-in stroke and load force. The results are given in Figure 2.10. For a pull-in stroke up to roughly ±40 µm the basic folded flexure is the best flexure to use. Although the slaved folded flexure and the tilted folded flexure can reach a larger stroke, due to the additional stiffness in actuation direction they require a larger actuator area. So when only a small stroke is required, the basic folded flexure is the 'optimal' flexure mechanism. For pull-in strokes up to roughly ±130 µm it is better to use the tilted folded flexure. The tilted folded flexure adds significant lateral stiffness in deflected state at the cost of little additional actuation stiffness. When the leafspring length is limited, for example due to the fabrication process,

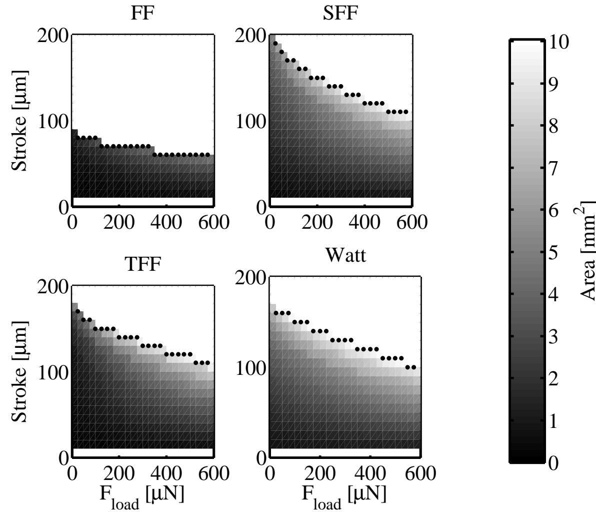

Figure 2.9: The wafer footprint of the flexure mechanisms is given as a function of the required stroke and the load force. The black dots indicate the maximum stroke for a given load force.

the slaved folded flexure is the mechanism that gives the largest pull-in stroke. This agrees with the results in Figure 2.6.

2.5 Design and fabrication

To validate our simulation results several designs have been made. The specific combination of a ±100 µm displacement and a 50 µN load force is chosen. These specifications have been chosen, since we are working on a multi-DOF platform with a stroke of ±100 µm [75]. This multi-DOF platform also requires an additional load force from our single-DOF actuators. The fabricated single-DOF designs for the four different flexure mechanisms are close to the minimum footprint designs for the given requirements and listed in Table 2.3 as 'FF L4300T19', 'SFF L1300T3', 'TFF L1200T3', and 'WATT L1200T3'. The most remarkable result is the extremely large leafspring length l_1 and thickness t_1 that is required for the folded flexure to reach the given specifications. With our fabrication process it is practically impossible to release 19 µm thick leafsprings from the handle wafer with HF etching. To create leafsprings with a thickness of 19 µm, perforation was added to the leafsprings. The leafspring thickness was increased slightly to 19.2 µm to correct for the stiffness decrease due to perforation, determined using FEM simulations with Solidworks Simulation [118].

Designs with different leafspring length and different leafspring thickness have also been made for validation. Due to fabrication issues it was not possible to

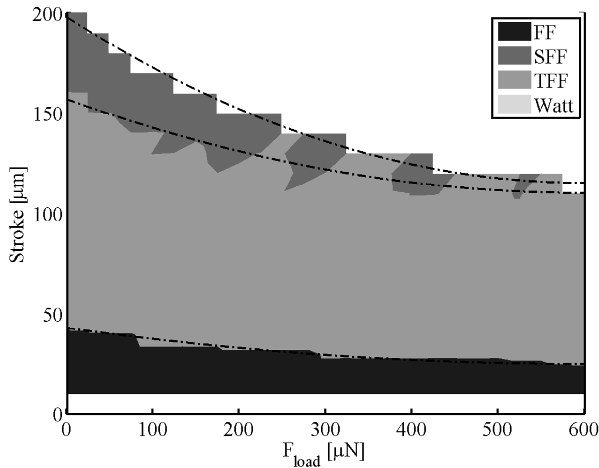

Figure 2.10: The graph shows the most compact flexure mechanism to reach a specified pull-in stroke and load force. The dash-dotted lines roughly give the limits to choose for the 'optimal' flexure mechanism. The Watt flexure never is the 'optimal' flexure mechanism.

perform measurements on all designed devices. In Table 2.3 the devices on which we were able to perform eigenfrequency and deflection measurements are listed. In addition to the aforementioned designs, this holds 'SFF L2000T5' and 'TFF L1400T5'.

To fabricate the designs aspect-ratio controlled deep reactive-ion etching (DRIE) was used to etch through the full device layer of the SOI-wafer of 50 µm. The directional etching and resulting high aspect ratios are particularly useful for good mechanical behavior of the leafsprings used for straight guiding the stage. A minimum trench width and a minimum feature size of 3 µm is used, limited by the aspect ratio of the DRIE step. A maximum trench width of 50 µm is used where possible to reduce variations in etch loading, which influences the subsurface profile development [58]. Former production runs have shown yield problems with extremely long leafsprings, so a maximum leafspring length of 2000 µm is used where possible. After reactive-ion etching, the structures were released from the handle wafer by isotropic HF vapor phase etching of the 1 µm thick buried oxide layer [49]. Thin structures (<10 µm) are released from the handle wafer in this way. Wide structures will stay mechanically fixed to the handle wafer, while being electrically isolated from the handle wafer due to the oxide layer. Stages and intermediate bodies that should be able to move are perforated to be released from the handle wafer. A probe station is used to connect the devices electrically for measurement.

Table 2.3: The fabricated designs that we were able to perform measurements on are listed in this table. The designs marked as 'FF L4300T19', 'SFF L1300T3', 'TFF L1200T3', and 'WATT L1200T3' are close to the minimum footprint designs for the requirement of ±100 µm and 50 µN. Designs with different leafspring length and different leafspring thickness have also been made for validation.

Flexure	**Parameters**		**Footprint**
FF L4300T19	$l_\mathrm{l} = 4300\,\mu\mathrm{m}$	$t_\mathrm{l} = 19\,\mu\mathrm{m}$	$5.60\,\mathrm{mm}^2$
		$N = 225$	
SFF L1300T3	$l_\mathrm{l} = 1300\,\mu\mathrm{m}$	$t_\mathrm{l} = 3\,\mu\mathrm{m}$	$3.62\,\mathrm{mm}^2$
	$x_\mathrm{lever} = 400\,\mu\mathrm{m}$	$N = 160$	
TFF L1200T3	$l_\mathrm{l} = 1200\,\mu\mathrm{m}$	$t_\mathrm{l} = 3\,\mu\mathrm{m}$	$2.44\,\mathrm{mm}^2$
	$\theta = 85°$	$N = 150$	
WATT L1200T3	$l_\mathrm{l} = 1200\,\mu\mathrm{m}$	$t_\mathrm{l} = 3\,\mu\mathrm{m}$	$4.48\,\mathrm{mm}^2$
	$x_\mathrm{ib} = 350\,\mu\mathrm{m}$	$N = 192$	
SFF L2000T5	$l_\mathrm{l} = 2000\,\mu\mathrm{m}$	$t_\mathrm{l} = 5\,\mu\mathrm{m}$	$5.12\,\mathrm{mm}^2$
	$x_\mathrm{lever} = 400\,\mu\mathrm{m}$	$N = 200$	
TFF L1400T5	$l_\mathrm{l} = 1400\,\mu\mathrm{m}$	$t_\mathrm{l} = 5\,\mu\mathrm{m}$	$3.28\,\mathrm{mm}^2$
	$\theta = 85°$	$N = 200$	

2.6 Experiment

The fabrication process introduces tapering of the leafsprings, which depends on many factors, such as the distance from the center of the wafer, the trench width and the timing of the SF_6 and FC deposition in the DRIE fabrication step [58]. Engelen et al. [38] report that in similar devices a designed leafspring thickness of 3 µm leads to an effective leafspring thickness roughly between 2.9 µm and 3.8 µm. So in order to compare the behavior of the designs with our simulations, an estimation of the effective leafspring thickness is required. A scanning electron microscope can be used to measure the thickness of the leafsprings at the top surface of the wafer, but cannot be used to measure the subsurface leafspring thickness without destroying the devices. Another method to estimate the effective leafspring thickness is used. The mass of the stage can be determined from the design fairly accurate. The mass of the stage and the first eigenfrequency are used to estimate the stiffness $\hat{K}_{x,\mathrm{ms}}$ in the actuation direction around zero deflection. The stiffness of the stage is related to the leafspring thickness. So the effective leafspring thickness $\hat{t}_{\mathrm{l,eff}}$ can be estimated from the measured eigenfrequency $f_{x,\mathrm{ms}}$, the designed eigenfrequency $f_{x,\mathrm{des}}$ and the designed leafspring thickness $t_{\mathrm{l,des}}$,

$$\frac{\hat{t}_{\mathrm{l,eff}}}{t_{\mathrm{l,des}}} = \left(\frac{\hat{K}_{x,\mathrm{ms}}}{K_{x,\mathrm{des}}}\right)^{1/3} = \left(\frac{f_{x,\mathrm{ms}}}{f_{x,\mathrm{des}}}\right)^{2/3}. \tag{2.10}$$

A Polytec MSA-400 and its Planar Motion Analyzer software [106] were used to measure the first eigenfrequency of the stages in actuation direction by applying

Table 2.4: The measured and the designed eigenfrequency are used to calculate the ratio between the designed and measured stiffness and the ratio between designed and effective leafspring thickness.

Flexure	**Stroke** µm	$\boldsymbol{f_{x,\mathrm{ms}}}$ Hz	$\boldsymbol{f_{x,\mathrm{des}}}$ Hz	$\boldsymbol{\hat{K}_{x,\mathrm{ms}}/K_{x,\mathrm{des}}}$ -	$\boldsymbol{\hat{t}_{\mathrm{l,eff}}/t_{\mathrm{l,des}}}$ -
FF L4300T19	87	498	511	0.950	0.983
SFF L1300T3	99[a]	271	215	1.59	1.17
TFF L1200T3	100[a]	352	287	1.50	1.15
WATT L1200T3	97[a]	483	407	1.41	1.12
SFF L2000T5	98[a]	242	246	0.968	0.989
TFF L1400T5	50[a]	432	369	1.37	1.11

[a] Stroke limited mechanically by endstops

a step in the actuation voltage. From the resulting underdamped oscillation of the stage the eigenfrequency and Q-factor were determined. The Q-factor was used to compensate the eigenfrequency for the relatively high damping of the stage in air. The measurements are listed in Table 2.4. The ratio between the effective leafspring thickness and the designed leafspring thickness is between 0.98 and 1.17 in our measurements. This means the effective leafspring thicknesses were between 2.9 µm and 3.5 µm, which is similar to the thicknesses reported by Engelen et al. [38].

The Polytec MSA-400 was also used to analyze the displacement of the flexure mechanisms as a function of the actuation voltage. The effective leafspring thicknesses $\hat{t}_{\mathrm{l,eff}}$ from Table 2.4 are used in our models for comparison with the measurements. It is assumed that tapering of the leafsprings is caused by wide trenches and for this reason the comb finger thichness t_{f} as well as the air gap g are not compensated with the measured leafspring thicknesses. Since the variation in leafspring thickness is relatively large, the eigenfrequency measurement as well as the displacement voltage measurement are needed to make a fair comparison with our electrostatic flexure pull-in model. For several devices we could not determine both, so these measurements are not included in this paper. The displacement of several flexure mechanisms is plotted versus the voltage squared in Figure 2.11.

In equation (2.6) we can see that when a flexure mechanism has a constant stiffness over its stroke, the displacement of the stage is linear with the actuation voltage squared. This is approximately the case for the folded flexure, the slaved folded flexure and the tilted folded flexure. The results of the Watt flexure show that the actuation stiffness of this flexure mechanism increases for large deflections; the voltage squared increases more than linearly with the deflection. This is the result of the non-linearly increasing curvature of the hinge flexure leafsprings for increasing stage displacements.

Although the additional load force was not applied, measurements showed that it was possible to reach displacements up to ±100 µm with all four flexure mechanisms, limited mechanically by endstops. When the effective leafspring thickness

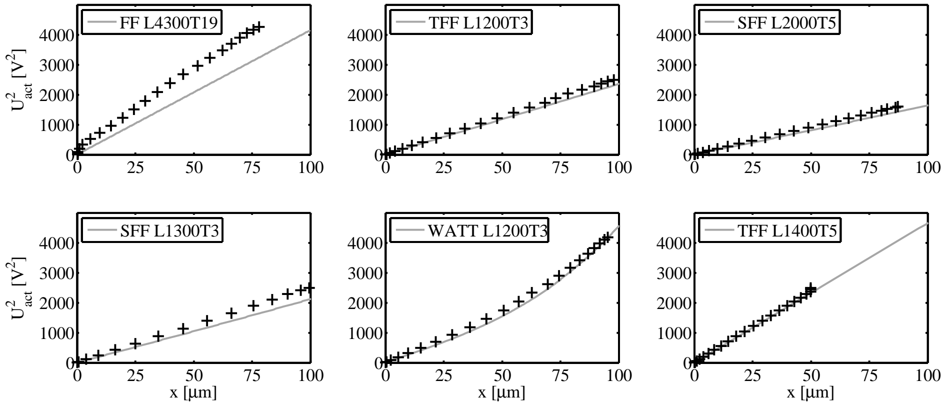

Figure 2.11: The displacement voltage measurements are given for several flexure mechanisms. The markers give the measurements and the lines indicate the simulation results.

$\hat{t}_{\mathrm{l,eff}}$ is used in the simulations, the displacement as a function of the actuation voltage does match the simulations fairly well, with 82% accuracy, for the slaved folded flexure, the tilted folded flexure and the Watt flexure. When the designed leafspring thickness is used for comparison with the measurements, the maximum error between measurement and simulation increases to 48%. Since the fabrication process has large variations and geometry measurements on fabricated devices are difficult in MEMS, it is hard to predict the displacement of the MEMS stages more accurately. However, the displacement results as a function of the actuation voltage are very repeatable, so the large deviation between simulation and measurement is not seen as a problem. The variation in leafspring thickness does theoretically influence the pull-in stroke of a flexure mechanism, since the lateral mechanical stiffness responds differently to variations in the leafspring thickness than the actuation stiffness. A decrease in pull-in stroke due to variations in the leafspring thickness was not observed. We conclude that the models can be used to predict the pull-in stroke of the various flexure mechanisms, but a large variation on the predicted actuation voltage to reach the displacement is possible due to tolerances in the fabrication process.

The folded flexure mechanism has a maximum error of 46% on the measured displacement for a given actuation voltage. As shown before in Table 2.3, the leafspring thickness of the folded flexure needed to be 19 µm. Our fabrication process only allowed structures with a thickness up to 10 µm to be underetched by the VHF. For this reason the leafsprings were perforated. The designed, right-angled perforations are probably different from the fabricated, chamfered perforations. This easily leads to a large variation in the stiffness of the flexure mechanism, which is a plausible cause for the large error between the simulation and the measurement results for the folded flexure.

2.7 Conclusion

In this paper a method to analyze the electrostatic stability of a flexure mechanism is presented, which limits the stroke of a stage actuated by comb-drives. Optimization of various flexure mechanisms with respect to the wafer footprint is performed and used to select the optimal flexure mechanism for a range of stroke and load force combinations.

Displacements of the fabricated stages as a function of the actuation voltage could be predicted with 82% accuracy, limited by the fairly large tolerances in our fabrication process. Although the additional load force was not tested, measurements also showed that it was possible to reach strokes of ±100 µm with four different flexure mechanisms. Based on the results of the measurements it is concluded that the models can be used to predict the pull-in stroke of different flexure mechanisms.

For small strokes, roughly up to ±40 µm, the standard folded flexure still is the optimal flexure mechanism to use. For larger strokes, the tilted folded flexure mechanism should be chosen. When the fabrication process limits the leafspring length, the slaved folded flexure is the mechanism that gives the largest pull-in stroke. The load force does not influence the choice of the flexure mechanism much.

Chapter 3

Deflection and pull-in of a misaligned comb drive finger in an electrostatic field

The elastic deflection of a comb drive finger in an electrostatic field is considered. The finger can be symmetrically located between two rigid fingers of the matching comb, in which case the problem reduces to a pure bifurcation problem for which the critical voltage can be determined. Alternatively, due to the non-linear motion of an approximate straight-line guidance mechanism, the base of the finger can have a lateral and angular displacement, which results in a smooth curve of equilibria with a limit point, after which pull-in occurs. An analytic model is derived, which is validated by two- and three-dimensional finite-element analyses and by experiments. For the analytic model, an assumed deflection shape and a series expansion of the electrostatic capacity yield the deflection curves. This shows that pull-in occurs at a voltage that is reduced by an amount that is about proportional to the two-third power of the relative base displacement. The theoretical results for the case of a lateral base displacement have been experimentally tested. The results show a qualitative agreement with the analytic model, but the experimental deflections are larger and the pull-in voltages are lower. The finite-element analyses show that these differences can be explained from neglected fringe fields and deviations from the nominal shape.

This chapter is published as 'J.P. Meijaard, B. Krijnen, and D.M. Brouwer. Deflection and pull-in of a misaligned comb drive finger in an electrostatic field. *Journal of Microelectromechanical Systems*, 23(4):927–933, 2014'.

3.1 Introduction

Actuation in microelectromechanical systems can be provided by electrostatic comb drives, which consist of two arrays of interdigitated fingers or teeth, one connected to a fixed base and the other to a moving base, which are held at an electric potential difference (voltage), as was first demonstrated by Tang *et al.* [124]. Since the electric field yields a negative lateral stiffness, these drives can suffer from instability if the positive mechanical stiffness is not sufficient, which can result in a sudden pull-in. This electrostatic instability has been known since the advent of microelectomechanical systems [95] and has been used to measure material properties at small scales [93, 100]. The lateral instability of comb drives, where the comb is pulled in as a whole, has been studied by Legtenberg *et al.* [80]. Also locally individual fingers can be pulled in, while the base to which the fingers are connected remains in place. The case of a finger centrally located between two rigid fingers has been considered by Elata and Leus [35], who analytically derived the critical voltage. Some experiments on buckling were performed later [2], which in essence confirmed the theory.

The combs are usually guided by an elastic straight-line mechanism. The approximate nature of the guidance causes the base to have, besides the intended longitudinal displacement, lateral and angular displacements. For instance, in a tilted folded flexure with a leaf-spring length of 1000 µm and a tilt angle of 5° [69], the lateral displacement (translation) is about 200 nm and the angular displacement (rotation) about 1.0 mrad for a longitudinal displacement of 150 µm, but the precise values depend strongly on the specific guidance and the configuration used. As an extension to [88], where only a lateral base displacement was considered, rotation as well as displacement are considered here. The analysis is restricted to the pull-in behavior of an individual finger placed between two rigid matching fingers. Of particular interest is the decrease of the pull-in voltage due to the base displacements, which is the main extension with respect to the analysis by Elata and Leus [35]. More general cases with flexible matching fingers and a finite support stiffness of the base can be analyzed along similar lines and yield qualitatively similar results.

The next section describes the model for a slender elastic finger between a pair of rigid fingers of the matching comb. The analytic solution given by Elata and Leus for the perfectly symmetrical case is reviewed next and an approximate deflection shape is shown to give accurate results. Then a deflection formula for a finger with a lateral and an angular base displacement is derived by an asymptotic analysis, and the results are compared with numerical results that more accurately take the non-linearity of the electrostatic force into account. The influence of fringe fields, neglected in the analytic approximation, is included in two- and three-dimensional finite-element calculations. Finally, theoretical results are compared with experimental results for the case of a lateral base displacement only.

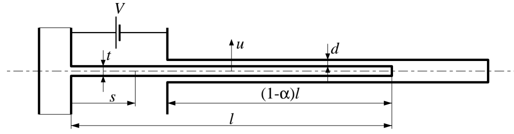

Figure 3.1: Flexible comb-drive finger between two rigid matching fingers.

3.2 Model description

The modeled configuration of the system is shown in Fig. 3.1. A flexible finger is inserted between two rigid matching fingers. The dimensions along the length of the finger are considered to be much larger than the dimensions in the lateral direction. Also the dimensions in the height direction, the view direction of Fig. 3.1, are considered to be much larger than the dimensions in the lateral direction, so the problem can be treated as two-dimensional. The height of the finger is h, the thickness is t and the length is l. The material of the finger has Young's modulus E. The finger is set at a voltage V with respect to the matching fingers. The distance between the rigid fingers is $2d+t$, so the gap width between the matching fingers is d if the finger is in a central position. The overlap is $(1-\alpha)l$, where we assume that α is close to 0, and in particular $\alpha = 0$ for most calculations, which represents the most critical position. The lateral deflection of the finger from the central position is denoted by u and the material coordinate along the length of the finger is s.

3.2.1 Energy Functional

A static equilibrium is characterized by a stationary value of the potential energy, which has contributions from the elastic deflection of the finger, the electric field, and the voltage source. For the considered small deflections, the elastic energy per unit of length is $EI(u'')^2/2$, where a prime denotes a derivative with respect to the material coordinate s and $EI = Eht^3/12$ is the flexural rigidity of the finger. Over the part of the finger between the two adjacent fingers of the matching comb, $\alpha l \leq s \leq l$, the electric field energy per unit of length is $q^2/(2C)$, where q is the charge per unit of length of the finger and C is the electrostatic capacity per unit of length, which depends on the lateral displacement u and is approximated by the parallel-plate formula as

$$C = \epsilon h \left(\frac{1}{d-u} + \frac{1}{d+u} \right) = \frac{2\epsilon h d}{d^2 - u^2} \,. \tag{3.1}$$

Here, ϵ is the permittivity of the air or vacuum in the gap, $\epsilon \approx 8.86\,\mathrm{pF/m}$. The contribution of the out-of-plane fringe fields at the top and the bottom of the finger are neglected, which is admissible if the height of the finger h is many times

larger than the thickness t and the gap width d. The fringe fields increase the capacity and change the dependence on the displacement, which has been studied in [60, 46].

The energy of the voltage source, $-V$ times the charge, has to be considered, because the charge changes as the finger deflects. The total potential energy, P, becomes

$$P = \int_0^l \left[\frac{1}{2}EI(u'')^2 + \frac{1}{2}\frac{q^2}{C} - Vq\right]\mathrm{d}s. \tag{3.2}$$

Because the in-plane fringe fields at the tip and at the part $0 \le s \le \alpha l$ are neglected, the charge as well as the capacity is zero for this part, so the two electrical terms have no contribution to P over this part of the finger. Taking variations with respect to the charge per unit of length q yields

$$q = CV, \tag{3.3}$$

which agrees with the definition of a capacity. On the other hand, taking variations of P with respect to u yields

$$\begin{aligned} \delta P &= \int_0^l \left[EIu''\delta u'' - \frac{q^2}{2C^2}\frac{\mathrm{d}C}{\mathrm{d}u}\delta u\right]\mathrm{d}s \\ &= \int_0^l \left[EIu'''' - \frac{q^2}{2C^2}\frac{\mathrm{d}C}{\mathrm{d}u}\right]\delta u\mathrm{d}s + \left[EIu''\delta u' - EIu'''\delta u\right]_0^l, \end{aligned} \tag{3.4}$$

where we have made use of partial integration. Since $\delta P = 0$ at an equilibrium and the variations are independent,

$$EIu'''' - \frac{q^2}{2C^2}\frac{\mathrm{d}C}{\mathrm{d}u} = 0. \tag{3.5}$$

The kinematic boundary conditions at $s = 0$ are

$$u(0) = u_0, \quad u'(0) = \psi_0, \tag{3.6}$$

where u_0 is the lateral displacement at the base of the finger and ψ_0 is the rotation of the base. The dynamic boundary conditions at $s = l$ follow from the boundary terms in the variation (3.4) and are the coefficients of $\delta u'$ and δu:

$$EIu''(l) = 0, \quad EIu'''(l) = 0, \tag{3.7}$$

which means that the moment and transverse shear force at the tip vanish. The energy functional can be modified by eliminating the charge by the relation (3.3) as

$$P^* = \int_0^l \left[\frac{1}{2}EI(u'')^2 - \frac{1}{2}CV^2\right]\mathrm{d}s. \tag{3.8}$$

Since the voltage V is a parameter, this is now a purely mechanical energy functional that contains the elastic energy and the negative energy of the attracting

distributed electrostatic forces. Taking variations with respect to u yields the mechanical equations, equivalent to (3.5),

$$EIu'''' - \frac{V^2}{2}\frac{\mathrm{d}C}{\mathrm{d}u} = 0, \tag{3.9}$$

or written out,

$$\frac{Eht^3}{12}u'''' - \frac{2V^2\epsilon hdu}{(d^2-u^2)^2} = 0, \tag{3.10}$$

where it is understood that the term with V^2 vanishes for $0 \leq s < \alpha l$.

3.3 Analytic bifurcation calculations

First, the analytic solution to the bifurcation problem when the finger is centrally located in the gap is reviewed. Then this solution is compared with a one-mode approximation, which shows that the approximation gives good results, so the single-mode approximation can be used for the more general case with base displacements. If the finger is centrally located in the gap, the pull-in voltage can be calculated analytically, as has been shown by Elata and Leus [35]. The difference here is that we assume plane stress instead of plane strain, as in elementary beam theory, which is a better approximation for the small deflections considered here [6] and gives a more conservative estimate of the pull-in voltage. The clamping at $s = 0$ further increases the stiffness if h/l is not small [86, 11]. Equation (3.10) can be linearized for small u as

$$\frac{Eht^3}{12}u'''' - \frac{2V^2\epsilon hu}{d^3} = 0, \tag{3.11}$$

or

$$l^4u'''' - \frac{V^2}{V_0^2}u = 0, \tag{3.12}$$

where

$$V_0 = \sqrt{\frac{Et^3d^3}{24\epsilon l^4}}. \tag{3.13}$$

The boundary conditions are

$$u(0) = 0, \quad u'(0) = 0, \quad EIu''(l) = 0, \quad EIu'''(l) = 0. \tag{3.14}$$

3.3.1 Exact Solution

For full overlap, $\alpha = 0$, the general solution to (3.12) is a linear combination of sine, cosine, hyperbolic sine, and hyperbolic cosine functions. The solution that satisfies the boundary conditions at $s = 0$ is

$$u = A(\cos\lambda s - \cosh\lambda s) + B(\sin\lambda s - \sinh\lambda s) \tag{3.15}$$

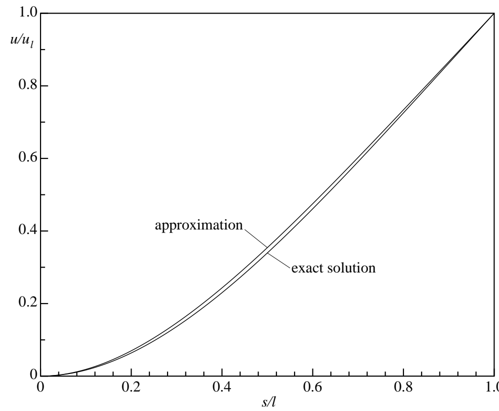

Figure 3.2: Normalized buckling mode shape $u(s)/u(l)$, for $\alpha = 0$ according to the exact analysis and according to the approximation (3.20).

with the undetermined constants A and B; λ is found to be

$$\lambda = \frac{1}{l}\sqrt{\frac{V}{V_0}}. \tag{3.16}$$

With (3.15), the dynamic boundary conditions (3.14) at $s = l$ become

$$\begin{aligned} EI\lambda^2[(-\cos\lambda l - \cosh\lambda l)A + (-\sin\lambda l - \sinh\lambda l)B] = 0, \\ EI\lambda^3[(\sin\lambda l - \sinh\lambda l)A + (-\cos\lambda l - \cosh\lambda l)B] = 0. \end{aligned} \tag{3.17}$$

In order to have a non-trivial solution, the determinant of the matrix of coefficients of the linear equations has to be zero. The root $\lambda = 0$ still leads to a trivial solution, so only $\lambda > 0$ need be considered. The equation for the determinant divided by the non-zero constant $(EI)^2\lambda^5$ is

$$\begin{aligned} &\begin{vmatrix} -\cos\lambda l - \cosh\lambda l & -\sin\lambda l - \sinh\lambda l \\ \sin\lambda l - \sinh\lambda l & -\cos\lambda l - \cosh\lambda l \end{vmatrix} = \\ &= 2(1 + \cos\lambda l \cosh\lambda l) = 0. \end{aligned} \tag{3.18}$$

The smallest positive solution is approximately $\lambda = 1.8751/l$, so the critical voltage is

$$V_{\mathrm{cr}} = (1.8751)^2\, V_0 = \frac{3.5160}{l^2}\sqrt{\frac{Et^3d^3}{24\epsilon}}. \tag{3.19}$$

The buckling mode shape with $u(l) = 1$ has $A = -0.5$ and $B = (1+\cos\lambda l)/(2\sin\lambda l) = 0.36705$, which is the same as the mode shape of a vibrating cantilever beam [29], and is shown in Fig. 3.2 as the exact solution.

For $\alpha > 0$, the parts with $0 \le s < \alpha l$ and $\alpha l \le s < l$ have to be considered separately and the solutions have to be continuous with continuous derivatives up

to the third order. Details can be found in [35]. For $\alpha = 0.1$, 0.2 and 0.5, the numerical value in (3.19) becomes 3.51606, 3.51720 and 3.60761, respectively, so for small values of α, the critical voltage does not change so much and the value for $\alpha = 0$ is a conservative estimate.

3.3.2 Approximate Solution

In this section, an approximate solution based on an assumed mode is compared with the exact solution to assess its accuracy. The assumed mode can be used in more general cases with base displacements and $\alpha > 0$. An approximate solution to the bifurcation problem can be found by assuming some suitable deflection mode, substituting this mode with an undetermined participation factor into the functional of (3.8) and finding non-trivial stationary values. We take an assumed mode that satisfies the kinematic and dynamic boundary conditions in (3.6) and (3.7) and is proportional to the deflection caused by a uniformly distributed lateral load. With the base displacements and the tip displacement u_l, the total deflection is expressed as [41]

$$u = u_0 + \psi_0 l\xi + (u_l - u_0 - \psi_0 l)\big(\frac{1}{3}\xi^4 - \frac{4}{3}\xi^3 + 2\xi^2\big), \tag{3.20}$$

where $\xi = s/l$, $0 \leq \xi \leq 1$, is the dimensionless material coordinate along the finger, u_0 and ψ_0 are the base displacements as in (3.6), and $u_l - u_0 - \psi_0 l$ is the undetermined participation factor for the deflection mode, the deflection at the tip of the finger minus the initial deflection due to the base displacements. The mode shape for $u_0 = 0$ and $\psi_0 = 0$ is shown in Fig. 3.2 as the approximation.

Expansion of the capacity C of (3.1) in powers of u leads to

$$C = \frac{2\epsilon h}{d}\Big[1 + \frac{u^2}{d^2} + \frac{u^4}{d^4} + \cdots\Big]. \tag{3.21}$$

For the perfect bifurcation problem, only terms up to quadratic ones in the energy functional (3.8) need be included, so we can use the truncated functional

$$P_2^* = \int_0^l \Big[\frac{1}{2}EI(u'')^2 - \frac{\epsilon h}{d^3}u^2V^2\Big]\mathrm{d}s, \tag{3.22}$$

where the constant term has been omitted. Substitution of (3.20) with $u_0 = 0$ and $\psi_0 = 0$ into the functional (3.22) and evaluating the integrals for $\alpha = 0$ results in

$$P_2^* = \frac{2}{15}\frac{Eht^3}{l^3}u_l^2 - \frac{104}{405}\frac{\epsilon hl}{d^3}u_l^2V^2, \tag{3.23}$$

which ceases to be positive definite if the second derivative is zero, which occurs at

$$V_{\mathrm{cr}} = \sqrt{\frac{162}{13}}\,V_0 = \frac{3.53009}{l^2}\sqrt{\frac{Et^3d^3}{24\epsilon}}\,. \tag{3.24}$$

This value differs only 0.4 % from the analytic value, so the assumed mode can be considered a good approximation for any small deflection. For $\alpha = 0.1$, 0.2 and 0.5, the numerical values in (3.24) become 3.53014, 3.53150 and 3.63174, respectively, so even for $\alpha = 0.5$, the difference from the analytic solution is smaller than 0.7 %.

3.3.3 Perturbed Bifurcation Problem

For the case with an initial base displacement, the problem changes from a bifurcation problem to a deflection problem. For small base displacements, the problem can be seen as a perturbed bifurcation problem and an asymptotic analysis can be made according to the post-buckling theory by Koiter [67, 125, 127]. In the present analysis, we stick to the approximation of the deflection by the single mode (3.20) and a direct analysis can be made.

With the dimensionless quantities

$$\begin{aligned} &\bar{u} = \frac{u}{d}\,, \quad \bar{u}_0 = \frac{u_0}{d}\,, \quad \bar{u}_l = \frac{u_l}{d}\,, \quad \bar{\psi}_0 = \frac{\psi_0 l}{d}\,, \\ &\bar{V} = \frac{V}{V_{\text{cr}}} = V l^2 \sqrt{\frac{52\epsilon}{27Et^3d^3}}\,, \quad \bar{P}^* = \frac{15P^*l^3}{4Eht^3d^2}\,, \end{aligned} \tag{3.25}$$

we expand the functional (3.8) further to quartic terms as

$$\bar{P}^* \approx \bar{P}_2^* + \bar{P}_4^* = \int_0^1 \left[\frac{5}{32}\left(\frac{\mathrm{d}^2\bar{u}}{\mathrm{d}\xi^2}\right)^2 - \frac{405}{208}\bar{V}^2\left(\bar{u}^2 + \bar{u}^4\right)\right]\mathrm{d}\xi. \tag{3.26}$$

Substituting the approximation (3.20) in the expansion and evaluating the integrals, omitting some constant terms, gives the result

$$\begin{aligned} \bar{P}^* \approx \frac{1}{2}(\bar{u}_l - \bar{u}_0 - \bar{\psi}_0)^2 - \bar{V}^2\Bigg[\\ &\left(\frac{81}{52}\bar{u}_0 + \frac{9}{8}\bar{\psi}_0\right)(\bar{u}_l - \bar{u}_0 - \bar{\psi}_0) + \frac{1}{2}(\bar{u}_l - \bar{u}_0 - \bar{\psi}_0)^2 \\ &+\left(\frac{81}{26}\bar{u}_0^3 + \frac{45}{4}\bar{u}_0^2\bar{\psi}_0 + \frac{1917}{364}\bar{u}_0\bar{\psi}_0^2 + \frac{4185}{2912}\bar{\psi}_0^3\right) \\ &\quad\times(\bar{u}_l - \bar{u}_0 - \bar{\psi}_0) \\ &+\left(3\bar{u}_0^2 + \frac{438}{91}\bar{u}_0\bar{\psi}_0 + \frac{16059}{8008}\bar{\psi}_0^2\right)(\bar{u}_l - \bar{u}_0 - \bar{\psi}_0)^2 \\ &+\left(\frac{1752}{1183}\bar{u}_0 + \frac{32577}{26026}\bar{\psi}_0\right)(\bar{u}_l - \bar{u}_0 - \bar{\psi}_0)^3 \\ &+\frac{65154}{221221}(\bar{u}_l - \bar{u}_0 - \bar{\psi}_0)^4\Bigg]. \end{aligned} \tag{3.27}$$

Equilibria are found from the equation obtained by putting the derivative with respect to $\bar{u}_l$ equal to zero. For a limit point, the resultant stiffness is zero, so

this point can be calculated by simultaneously solving the equation obtained by putting the second derivative equal to zero.

For moderate values of $\bar{V}$, we can restrict ourselves to the quadratic terms and we obtain the formula for the deflection

$$\bar{u}_l = \bar{u}_0 + \bar{\psi}_0 + \frac{81\bar{V}^2}{52(1-\bar{V}^2)}\left(\bar{u}_0 + \frac{13}{18}\bar{\psi}_0\right). \tag{3.28}$$

For an asymptotic analysis near the limit point, we can even simplify the energy expression (3.27) further by noting that $\bar{V}$ is close to one and $\bar{u}_l$ is much larger than $\bar{u}_0$ and $\bar{\psi}_0$, which gives

$$\begin{aligned}\bar{P}^* \approx\ & \frac{1}{2}(1-\bar{V}^2)(\bar{u}_l - \bar{u}_0 - \bar{\psi}_0)^2 \\ & -\frac{81}{52}\left(\bar{u}_0 + \frac{13}{18}\bar{\psi}_0\right)(\bar{u}_l - \bar{u}_0 - \bar{\psi}_0) \\ & -\frac{65154}{221221}(\bar{u}_l - \bar{u}_0 - \bar{\psi}_0)^4 .\end{aligned} \tag{3.29}$$

Putting $\mathrm{d}\bar{P}^*/\mathrm{d}\bar{u}_l = 0$ and $\mathrm{d}^2\bar{P}^*/\mathrm{d}\bar{u}_l^{\,2} = 0$ yields the asymptotic analytic expressions for the limit point voltage and the corresponding limit point deflection as

$$\begin{aligned}\bar{V}_{\mathrm{lp,an}} &\approx 1 - 1.341(\bar{u}_0 + 0.722\bar{\psi}_0)^{\,2/3}, \\ \bar{u}_{l,\mathrm{lp,an}} &\approx \bar{u}_0 + \bar{\psi}_0 + 0.871(\bar{u}_0 + 0.722\bar{\psi}_0)^{\,1/3} \\ &\approx 0.871(\bar{u}_0 + 0.722\bar{\psi}_0)^{\,1/3}.\end{aligned} \tag{3.30}$$

The linear term in the critical tip displacement can be omitted, since terms of the same order have been neglected in the calculations.

It is seen that the drop in the critical voltage is proportional to the two-third power of the magnitude of the base displacements, whereas the deflection at the critical voltage is proportional to the cubic root of the magnitude of the base displacements. This means that the curve of the critical voltage against a component of the base displacement has a vertical tangent at zero displacement and a small base displacement may already give rise to a significant drop in the critical voltage. For instance, for $d = t = 3\,\mu\mathrm{m}$, $l = 120\,\mu\mathrm{m}$, $E = 169\,\mathrm{GPa}$, the critical voltage without base displacements is $V_{\mathrm{cr}} = 186\,\mathrm{V}$. For base displacements $u_0 = 0.15\,\mu\mathrm{m}$ and $\psi_0 = 0.001\,\mathrm{rad}$, the critical voltage drops to 140 V. For fingers with an increased length of 160 μm, the critical voltage drops from 105 V to 73 V for base displacements of $u_0 = 0.20\,\mu\mathrm{m}$ and $\psi_0 = 0.001\,\mathrm{rad}$.

3.4 Numerical calculations

In order to see how accurate the asymptotic results of (3.30) are, some numerical calculations are made. The differential equation (3.10) is solved for given values of

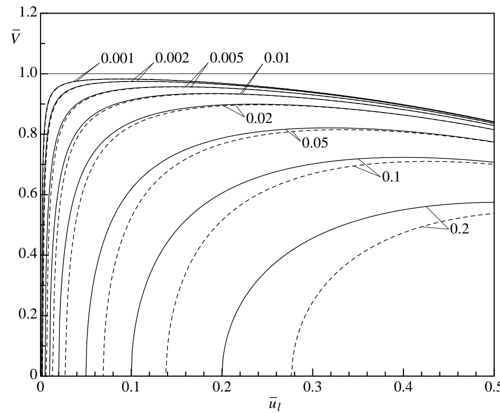

Figure 3.3: Dimensionless finger tip deflection $\bar{u}_l$ versus dimensionless voltage $\bar{V}$ from numerical calculations for several values of the dimensionless lateral base displacement $\bar{u}_0$ or scaled dimensionless base rotation $13\bar{\psi}_0/18$ as indicated for each line: 0.001, 0.002, 0.005, 0.01, 0.02, 0.05, 0.1 and 0.2. The solid lines are for the case of a lateral base displacement and the dashed lines are for the case of a base rotation.

the lateral base displacement, u_0, and base rotation, ψ_0, and a given tip displacement, which gives as results the voltage and the deflection. A shooting method [121] is used to solve the resulting boundary value problem. The deflection curves for several values of the initial lateral base displacement as well as for several values of the base rotation are shown in Fig. 3.3. The solutions in the initial rising part are stable, whereas the solutions beyond the limit point are unstable.

The approximate values of the dimensionless limit-point voltages and the values obtained in a numerical way are compared in Fig. 3.4. It appears that the asymptotic approximation is rather good in comparison with the numerical solution up to a dimensionless initial lateral tip displacement of 0.1 and gives conservative qualitatively valid estimations for much larger initial displacements, at least up to an dimensionless initial lateral tip deflection of 0.5.

3.5 Experimental validation

3.5.1 Experiments

Experimental samples were produced by etching structures in the device layer of a silicon-on-insulator (SOI) wafer, which consists of a device layer of monocrystalline silicon on an insulating layer of silicon oxide, which in turn rests on a substrate layer of silicon. The height of the device layer, and hence the height of the structures, was $h = 50\,\mu\text{m}$, whereas the insulating layer was 1 μm thick. Each structure

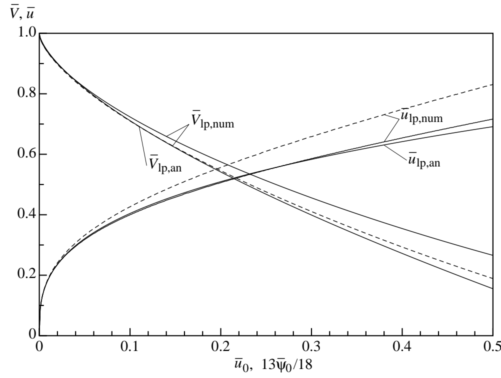

Figure 3.4: Dimensionless limit-point voltages $\bar{V}$ and tip deflections $\bar{u}_l$ as functions of the dimensionless lateral base displacement $\bar{u}_0$ or the scaled base rotation $13\bar{\psi}_0/18$. $\bar{V}_{\text{lp,an}}$ and $\bar{u}_{\text{lp,an}}$ are from the asymptotic analytic approximation, and $\bar{V}_{\text{lp,num}}$ and $\bar{u}_{\text{lp,num}}$ are from the numerical approximation. The solid lines are for the case of a lateral base displacement and the dashed lines are for the case of a base rotation.

consisted of a single finger fixed to a sturdy base located at a fixed position in a slit etched out of a solid block. The fingers had a nominal length $l = 120\,\mu\text{m}$ and a nominal width of $t = 3\,\mu\text{m}$. The slit had a nominal width of $9\,\mu\text{m}$, so the nominal gap width was $d = 3\,\mu\text{m}$. The overlap was chosen as large as practically possible, $110\,\mu\text{m}$, which gives $\alpha = 10/120 = 0.0833$. The position of the finger in the slit could be central, or with a nominal uniform lateral offset of $u_0 = 0.25\,\mu\text{m}$ or $u_0 = 0.50\,\mu\text{m}$. The axis of the finger was in the $< 1\,1\,0 >$ direction of the crystal, so $E = 169\,\text{GPa}$ [50]. As an example, a test specimen with a lateral offset of $0.50\,\mu\text{m}$ is shown in Fig. 3.5, where pull-in has occurred and the finger sticks to the wall.

Deflection curves were measured by applying a voltage difference between the finger and the slit and observing the deflection by stroboscopic light microscopy with a microsystem analyzer (Polytec MSA-400). Software for planar motion analysis was used to extract the deflections with a resolution of 15 nm rms. The pull-in voltage was determined by slowly increasing the applied voltage until pull-in took place. The pull-in voltage was determined for the point where a current through the device started to flow owing to short-circuiting caused by contact between the finger and the wall. The set-up for measurement of the limit-point voltages is given in Fig. 3.6. The supply voltage V_s is too high to be measured directly, so a voltage divider (R_1, R_2, V_1) is used to measure it. The supply voltage is increased until the finger gives pull-in, where the MEMS structure short-circuits and V_2 shows a voltage step. The value of V_1 at the moment of short-circuit is used to calculate the corresponding supply voltage, which is the limit-point voltage.

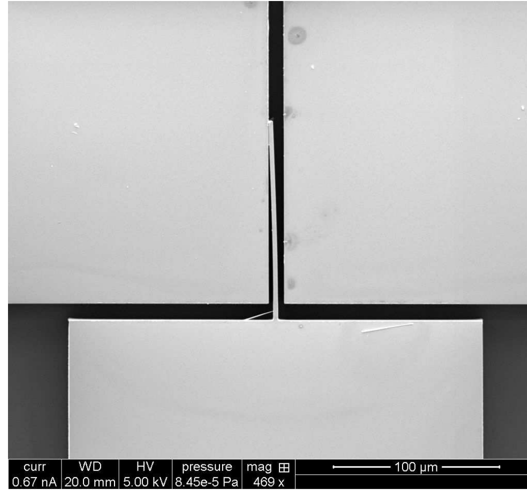

Figure 3.5: SEM picture of a test specimen with a lateral offset of 0.50 µm after pull-in.

3.5.2 Finite-Element Calculations

To check the accuracy of the basically one-dimensional model, more advanced finite-element models were used. A two-dimensional model, which includes the effects at the base and the tip of the finger, was analyzed, and also a three-dimensional model which includes the effects of the fringe fields at the top and the bottom of the finger. The fringe fields tend to increase the capacity of the finger and the absolute value of the negative electrostatic stiffness. Furthermore, in the three-dimensional model, the influence of the grounded substrate was investigated. The finite-element models were made and analyzed in the multi-physics finite-element program COMSOL [92]. Quadratic triangular elements for the two-dimensional calculations and quadratic tetrahedral elements for the three-dimensional case were used. The mesh had a minimal element size of 2.4 µm, which means that in general a mesh one element through the thickness of the fingers is used. The average element size of the mesh of the finger was about 4.0 µm. Near the edges, the minimal element size was chosen. The gaps were meshed in a similar way, whereas for the three-dimensional case, the element size for the surrounding space was allowed to increase gradually to about 0.1 mm in a rectangular box with dimensions of $0.2 \times 0.4 \times 0.6\,\mathrm{mm}^3$.

The results of the calculations are shown in Fig. 3.7 for the two experimental cases of a lateral base displacement of 0.25 µm and 0.50 µm. The finite-element models yield larger displacements and the three-dimensional models yield larger displacements than the two-dimensional models. The influence of the grounded substrate is considerable and yields increased displacements. The field energy near the bottom is larger if the substrate is present compared with the case without

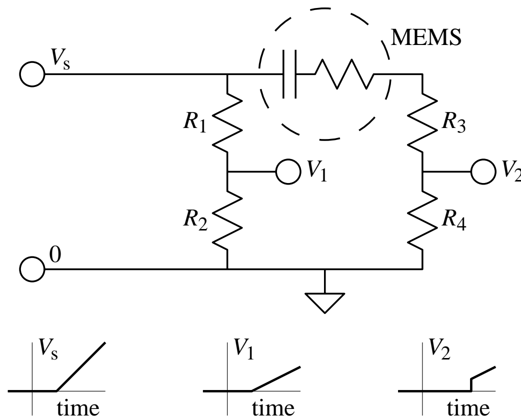

Figure 3.6: Measurement circuit for determining pull-in voltages.

substrate. The attractive force is the change of the field energy with respect to the displacement, which will also increase, although the relation is not a simple proportionality. Furthermore, it could be observed that the attractive force near the substrate made the finger twist along its longitudinal axis, so the bottom has a higher deflection than the top. Also shown are two cases of a base rotation of 2 mrad and 4 mrad, where the results from the one-dimensional model are compared with the two-dimensional finite-element results. The same qualitative behavior as for the case of a lateral base translation can be seen.

3.5.3 Measurement Results

The observed deflection curves, where the displacement is scaled with the gap width and the voltage with the theoretical pull-in voltage of $V_{\mathrm{cr}} = 186\,\mathrm{V}$, are shown in Fig. 3.8. The measurement produced loops for an increasing voltage up to its maximum and then a decreasing voltage back to zero. The spread of the lines is mainly a result of the limited resolution of the optical measurement system. It is seen that the measured deflections are larger than the theoretical deflections, but agree reasonably well with the results from the three-dimensional finite-element model with a grounded substrate.

Table 3.1 lists the observed pull-in voltages for four different values of the lateral base displacement $\bar{u}_0$, which are compared with the voltages predicted by the models. The pull-in voltages for the finite-element models were obtained from extrapolations of the results as shown in Fig. 3.7. The measured pull-in voltages are lower than the predicted ones except for the pull-in voltages obtained with the three-dimensional model with a grounded substrate. The rather low measured pull-in voltage for a zero lateral base displacement can be attributed to the high sensitivity of the results for small imperfections in the samples for this case.

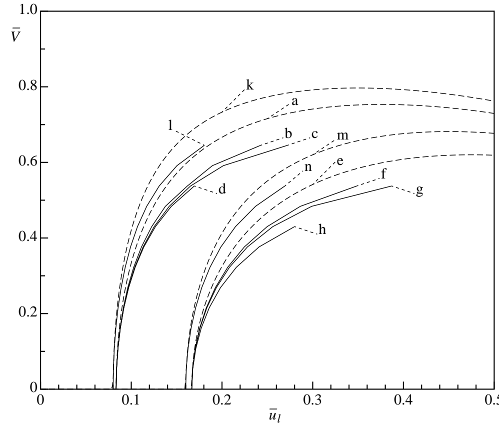

Figure 3.7: Calculated deflection curves for $\bar{u}_0 = 1/12$ (lines a, b, c, and d), $\bar{u}_0 = 1/6$ (lines e, f, g, and h), $\bar{\psi} = 0.08$ (lines k and l), and $\bar{\psi}_0 = 0.16$ (lines m and n). Lines a, e, k, and m (dashed) are from the 1-D numerical model, as in Fig. 3.3, lines b, f, l, and n are from a 2-D finite-element model, lines c and g are from a 3-D finite-element model without substrate and lines d and h are from a 3-D finite-element model with grounded substrate.

Table 3.1: Calculated and measured pull-in voltages for four different lateral base displacements. The calculated values are the analytical and numerical values as in Fig. 3.4 and the 2-D and 3-D finite-element results.

$\bar{u}_0$	0.0	0.08333	0.100	0.16666
$\bar{V}_{\text{lp,an}}$	1.000	0.744	0.711	0.594
$\bar{V}_{\text{lp,num}}$	0.996	0.753	0.723	0.620
$\bar{V}_{\text{lp,2-D}}$		0.652	0.648	0.555
$\bar{V}_{\text{lp,3-D}}$ (no substrate)		0.651	0.648	0.542
$\bar{V}_{\text{lp,3-D}}$ (with substrate)		0.586	0.554	0.464
$\bar{V}_{\text{lp,measured}}$	0.750		0.605	0.510

3.6 Conclusions

An asymptotic expression for the pull-in voltage for a finger with a lateral base displacement and a base rotation has been derived, together with an asymptotic analytic expression for the tip displacement at the onset of pull-in. The decrease of the dimensionless pull-in voltage is proportional to the two-third power of the dimensionless base displacement, whereas the corresponding dimensionless tip displacement is proportional to the cubic root of the dimensionless base displacement. The asymptotic expressions have been checked by an accurate numerical solution of the simple one-dimensional model, which validates their correctness and shows their applicability if the initial lateral tip displacement is smaller than one tenth of

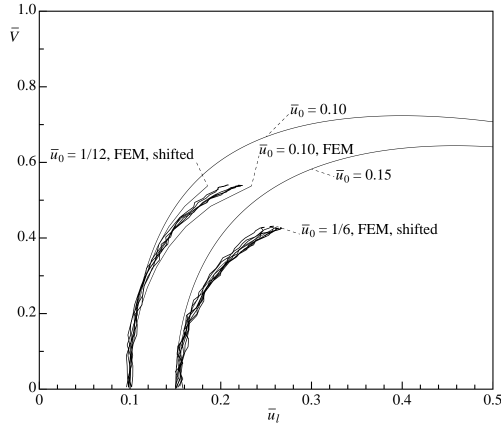

Figure 3.8: Measured deflection curves for $\bar{u}_0 = 1/12$ (three measured loops) and $\bar{u}_0 = 1/6$ (four measured loops). Also shown are the numerically determined deflection curves, as in Fig. 3.3, and the curves for the top deflection from the 3-D finite-element model with grounded substrate.

the nominal gap width. More accurate finite-element models can take into account the influence of fringe fields, which tend to lower the pull-in voltage.

An experimental validation of some of the presented theoretical results shows that the observed deflections are larger and the observed pull-in voltages are lower than the theoretical values, except for those obtained with the most complete three-dimensional finite-element model, which are in rather good agreement with the experimental results.

Chapter 4

A single-mask thermal displacement sensor in MEMS

This work presents a MEMS displacement sensor based on the conductive heat transfer of a resistively heated silicon structure towards an actuated stage parallel to the structure. This differential sensor can be easily incorporated in a SOI based process, and fabricated within the same mask as electrostatic actuators and flexure based stages. We discuss a lumped capacitance model to optimize the sensor sensitivity as a function of the doping concentration, the operating temperature, the heater length and width. We demonstrate various sensor designs. The typical sensor resolution is 2 nm within a bandwidth of 25 Hz at a full scale range of 110 µm.

This chapter is published as 'B. Krijnen, R.P. Hogervorst, J.W. van Dijk, J.B.C. Engelen, L.A. Woldering, D.M. Brouwer, L. Abelmann, and H.M.J.R. Soemers. A single-mask thermal displacement sensor in mems. *Journal of Micromechanics and Microengineering*, 21(7):074007, 2011'.

4.1 Introduction

The trend towards smaller and more accurate positioning systems stimulates the use of MEMS applications. Examples of such accurate positioning systems already exist for a long time in MEMS. Two examples are (digital) light processing [52, 112] and the use of cantilevers in atomic force microscopy [10]. Actuators in combination with flexure based stages are able to reach positioning accuracies of several nanometers. Still, accurate positioning is limited by many factors, such as drift, external disturbances and load forces. Adding feedback control, and thus a position sensor, can enhance the performance of positioning systems.

Position and acceleration sensing in MEMS is often based on the varying electrical capacitance between a static reference and an actuated stage [76, 77, 22]. The disadvantage of accurate and long-range capacitive displacement sensors is the large required wafer surface area. Some alternative sensors use integrated optical waveguides [9], the piezoresistive effect [84, 30], or varying thermal conductance [78, 26, 105]. Lantz et al. demonstrate a thermal displacement sensor achieving nanometer resolution over a 100 µm range [78]. However, this sensor is produced in two separate wafers and therefore precision assembly was needed to fabricate this displacement sensor together with the stage. We found a way to integrate a thermal displacement sensor together with an actuated and flexure based stage in the device layer of a silicon-on-insulator (SOI) wafer. Design, fabrication and experimental validation of the sensor is presented in this work.

The integration of sensor and actuator in a single layer of silicon has multiple advantages. It obeys several design principles for precision manipulation [120]; contactless sensing and actuation do not introduce friction and hysteresis. Without assembly of separate components, misalignments are avoided. Overconstraints in a monolithic device layer are less likely to lead to unpredictable system behavior [87]. We succeeded in integrating the sensor without any modification of the process for the fabrication of the electrostatic actuators and the flexure based stage. The complete device is designed to be fabricated using only one mask.

The basic design of one of the heaters of the sensor is shown in Figure 4.1. Wire bonds are connected to the bondpads to supply an electrical current. The silicon heater is resistively heated due to the supplied electrical power. When the stage is overlapping the heater, heat is conducted from the heater to the stage, q_{stage}, through the thin layer of air, a. A large stage overlap results in efficient cooling of the heater and therefore its temperature will decrease. The resulting decrease in electrical resistance can be measured, since the electrical resistivity of silicon is highly dependent on the temperature. The electrical resistance of the heater thus is a measure for the position of the stage. A differential sensor configuration is chosen to make the sensor less sensitive to changes common to both heaters, like ambient temperature and air humidity. This differential configuration is shown in Figure 4.2.

In Section 4.2 we will show a lumped capacitance model of the sensor. The model will be used to design and optimize the sensor. The integration of the sensor

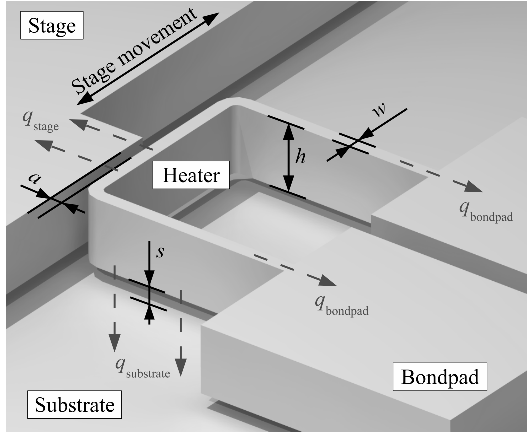

Figure 4.1: Schematic overview of a single heater with its dimensions and conductive heat flows (dashed red arrows). The heater height is given by h, the heater width is given by w, the air gap towards the stage by a and the air gap towards the substrate by s. The heater consists of two parts, the sensing part, which is parallel to the stage, and the heater legs, which are perpendicular to the stage. Heat conduction dominates the heat transport in the sensor. Conduction inside the silicon heater structure towards the bondpads is labeled q_{bondpad}, the conductive heat flow towards the stage is given by q_{stage} and the heat flow towards the substrate is given by $q_{\mathrm{substrate}}$. The stage will be perforated for fabrication.

with a flexure based stage and electrostatic comb-drive actuation is described in Section 4.3. Fabrication will be discussed in Section 4.4. Finally, measurements on the sensor output, noise and time constants are given in Section 4.5.

4.2 Modeling and model verification

In this section we will describe the lumped capacitance model of the sensor. The model is used to describe the temperature profile over the heaters and the heat flows in the sensor. Subsequently the model is used to optimize the sensor sensitivity as a function of the doping concentration, the heater dimensions and the operating mode and temperature. The sensitivity due to variation in heater dimensions and operating temperature is validated using measurements.

4.2.1 Lumped capacitance model

A dynamic multiphysics model is created of the thermal sensor in 20-sim [1]. The created model is a lumped capacitance model, which divides the heater structure into a discrete number of elements [56]. Each element has a single temperature.

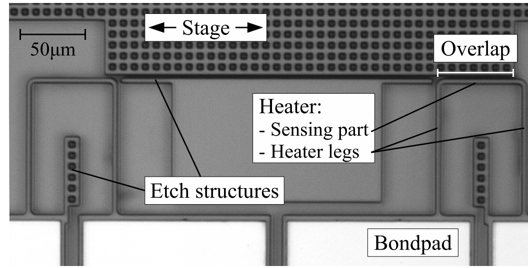

Figure 4.2: Top view, optical microscope image of a fabricated sensor with the actuated stage in its rightmost position. The electrostatic comb-drive actuators are outside the image. The sensor consists of two heaters. Each heater structure consists of a sensing part, two heater legs and two bondpads for mechanical and electrical connection. The heater on the right has maximum overlap with the stage, the heater on the left has minimum overlap with the stage. 'Etch structures' are incorporated to increase the DRIE quality. The heater leg length is 100 µm and the sensing part has a length of 60 µm.

One of the model elements is shown in Figure 4.3. The element consists of a heat capacitance (C1) coupled to an electrical resistance (Ω). The temperature of the heat capacitance determines the electrical resistance, which in turn determines the dissipated power in the heater element. The thermal capacitance of silicon is modeled temperature dependent, according to [42]. The temperature dependent electrical resistance of the silicon heaters is the basic quantity through which the stage position is measured. The temperature dependent electrical resistivity will be described in Section 4.2.2.

Heat transport in the sensor will take place due to conduction, convection and radiation. Conduction occurs inside the silicon heater structure towards the bondpads and through the air towards the stage and the substrate, as shown in Figure 4.1. The equation for conductive heat transfer is

$$q = \frac{\Delta T}{R_{\mathrm{T}}} \tag{4.1}$$

where q is the heat flow, ΔT is the difference in temperature and R_{T} is the thermal resistance. The thermal resistance is given by

$$R_{\mathrm{T}} = \frac{l}{kA} \tag{4.2}$$

where k is the thermal conductivity of the material, l is the length over which the heat transfer occurs and A is the area through which the heat transfer occurs. Both l and A are geometry and orientation dependent. The thermal conductivities of silicon and air are a function of the temperature. They are modeled according to [123] and [57], respectively.

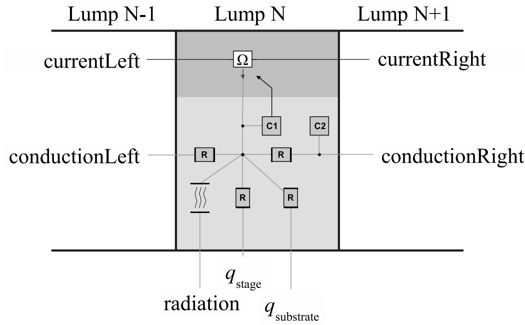

Figure 4.3: One of the elements of the thermal sensor model. The top of the diagram shows the electrical resistance (Ω). The thermal capacity C1 is connected to multiple thermal conductivities (R). A negligible thermal capacity C2 is added to prevent algebraic loops and the resulting increase of simulation time. Radiation is added, since it will play a role at high heater temperatures.

Convection does not play a significant role in the heat transport due to the small surface area of the heated structures. Radiation increases to the fourth power with the heater temperature and at 900 K the heat transfer due to radiation is around 2% of the total heat transfer. Radiation with an emissivity factor of 0.65 is included in the model. The emissivity factor of 0.65 takes temperature dependency as well as surface roughness of the silicon structures into account [109].

The effect of heat conduction towards the air is examined using the finite element modeling software COMSOL Multiphysics [92]. A bounding box is placed around the heater structure and underlying substrate layer. Two different boundary conditions are applied, thermal insulation and heatsink. Simulations show that when the air layer is thicker than 100 µm, the heater temperature varies by only 0.1 K for the different boundary conditions. This means the heat will flow only towards the substrate layer and the 100 µm thick air layer around the heater will function as a thermal insulation layer. In the design of the system, trenches as wide as possible are chosen to avoid heat flow through the air towards other structures in the device layer. The additional conductive heat flow towards the substrate layer is also examined using COMSOL Multiphysics. This showed that the heat conduction from the heater towards the underlying substrate is underestimated, roughly by a factor 5, when using only the heater width and the substrate gap thickness. This is caused by extra heat conduction from the sidewalls of the heaters towards the substrate.

An effective width w_{eff} is determined empirically to compensate for the additional heat flow towards the substrate. The effective width is based on the actual heater width w, the heater height h and substrate gap thickness s

$$w_{\mathrm{eff}}(w, h, s) = w + w_{\mathrm{a}}(h) f(s) \tag{4.3}$$

The additional width w_{a} as a function of the heater height h as well as the

correction factor f as a function of the substrate gap s are approximated by a Taylor expansion

$$w_{\mathrm{a}}(h) = 1.50 \times 10^{8} h^{3} - 1.65 \times 10^{4} h^{2} + 5.95 \times 10^{-1} h + 6.99 \times 10^{-6} \tag{4.4}$$

$$f(s) = -2.15 \times 10^{10} s^{2} + 3.49 \times 10^{5} s + 1.32 \times 10^{-1} \tag{4.5}$$

The effective width w_{eff} instead of the actual heater width w is used to calculate the heat flow towards the substrate. The basic equations for conductive heat transfer can be applied again, (4.1) and (4.2).

A model with 5 elements for each leg of the heater and 13 elements for the sensing part of the heater proved to be sufficient. Convergence was checked by using the same model with twice the amount of elements. COMSOL was used to verify the response of the sensor for several configurations. The model is used to gain more insight in the heat flow balance and temperature profile over the heaters and for optimization of the sensor design.

4.2.2 Resistivity and doping concentration

An important property in the lumped capacitance model is the resistivity of silicon as a function of temperature. A model for the temperature dependent electrical resistivity of silicon with various doping species is given in [123]. The intrinsic carrier concentration determines the majority and minority carrier concentrations and is given in [33].

$$n_{\mathrm{i}}(T) = K\sqrt{N_{\mathrm{c}} N_{\mathrm{v}}} \left(\frac{T}{T_0}\right)^{3/2} \exp\left(-\frac{E_{\mathrm{g}}(T)}{2k_{\mathrm{B}}T}\right) \tag{4.6}$$

where T_0 is 300 K, $N_{\mathrm{c}} = 2.8 \times 10^{19}\,\mathrm{cm}^{-3}$ denotes the effective density of states for electrons in the conduction band and $N_{\mathrm{v}} = 1.04 \times 10^{19}\,\mathrm{cm}^{-3}$ denotes the effective density of states for holes in the valence band at T_0, E_{g} is the band-gap energy as a function of the temperature and k_{B} the Boltzmann constant. An empirical value for $K \simeq 3.0$ is used to correct the intrinsic carrier concentration n_{i} as a function of temperature, as described in [33].

The mobility of the charge carriers is limited due to impurity scattering and due to phonon scattering. The mobility of the charge carriers due to phonon scattering as a function of temperature is

$$\mu_{\mathrm{ps}} = \mu_{\mathrm{L0}} \left(\frac{T}{T_0}\right)^{p_{\mathrm{ps}}} \left(\frac{m_{\mathrm{e}}}{m}\right)^{5/2} \tag{4.7}$$

where $\mu_{\mathrm{L0}} = 1600\,\mathrm{cm}^2\mathrm{V}^{-1}\mathrm{s}^{-1}$ is the lattice mobility at T_0, $m_{\mathrm{e}} = 0.33$ is the effective electron mass and $m = 0.55$ is the effective charge carrier mass for holes. The phonon scattering exponent p_{ps} for boron doping ranges roughly from 1.5 to 2.2 in literature [123, 32, 110]. In our resistivity model a phonon scattering exponent p_{ps} of 1.90 gives the best fit. For two boron doping concentrations,

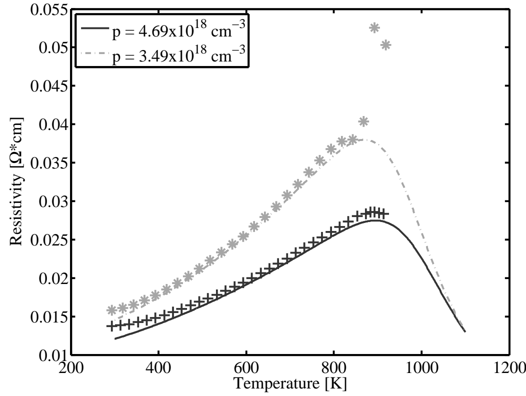

Figure 4.4: Resistivity model and measured data of highly boron doped silicon, with doping concentrations $3.5 \times 10^{18}\,\mathrm{cm}^{-3}$ and $4.7 \times 10^{18}\,\mathrm{cm}^{-3}$, as a function of the temperature. Fit parameters used in the model are $p_{\mathrm{ps}} = 1.90$ and $K = 3.0$ [33]. The aluminium wire bonds that connect the structures in a 4-point measurement setup melt around 900 K, which explains the deviated measurement results at these high temperatures.

$3.5 \times 10^{18}\,\mathrm{cm}^{-3}$ and $4.7 \times 10^{18}\,\mathrm{cm}^{-3}$, the theoretical model of the silicon resistivity is given together with the measured data in Figure 4.4. The measured data fits well with the theoretical model.

The resistivity curves are used in the lumped capacitance model to examine the influence of the doping concentration in the device layer of the SOI wafer on the sensitivity of the sensor. In a differential configuration, the resistance change as a function of the stage overlap is roughly linear. Therefore the resistance change from maximum to minimum overlap, divided by the stroke from maximum to minimum overlap, is a good number for the sensor sensitivity in Ω/µm. To decrease boundary effects on the transition from the sensing part to the heater legs, the sensing part is designed slightly longer than the required stroke.

The sensitivity of the sensor as a function of the maximum heater temperature at minimum overlap is shown for several doping concentrations in Figure 4.5. At a low operating temperature, the sensitivity of the sensor is restricted by the small change in temperature when going from minimum to maximum overlap. At a high operating temperature, close to the maximum resistivity, the sensitivity is restricted by the slope in the resistivity curve, which determines the resistance change as a function of the temperature change from minimum to maximum overlap.

The sensitivity of the sensors increase for lower doping concentrations. This is a direct result of the steeper slope in the resistivity curve at these lower doping concentrations (Figure 4.4). The peak in the resistivity curve is located at a lower temperature for lower doping concentrations. This explains why the sensitivity curve for lower doping concentrations has its maximum at lower temperatures.

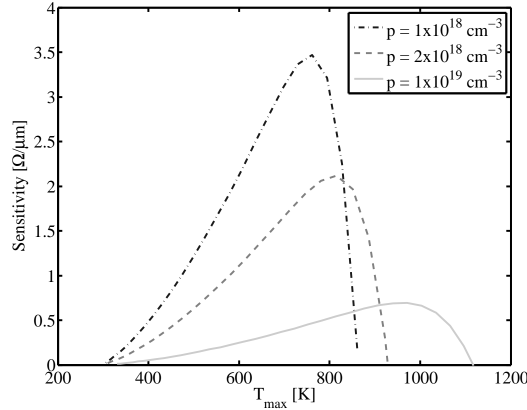

Figure 4.5: For a given maximum temperature at minimum overlap, the sensitivity is plotted for different doping concentrations. The heaters used in this simulation have the following dimensions: heater width and air gap 3 µm, heater length 610 µm (sensing part 130 µm and legs 240 µm), heater height 50 µm and substrate gap 3 µm.

A lower doping concentration leads to a higher electrical resistance of the heater structures. Therefore more intrinsic thermal Johnson-Nyquist noise will occur, which might be a problem. For the examined heater dimensions and doping concentrations the intrinsic thermal Johnson-Nyquist does not exceed 2 µV, for a bandwidth of 1 kHz and an average heater temperature of 1000 K. Therefore, we conclude that Johnson-Nyquist noise is negligible compared to other noise sources in our sensor, also see Section 4.5.2.

A lower limit for the doping concentration is based on the increasing electrical resistance of the comb-drive actuators when decreasing the doping concentration. This will result in higher electrical time constants of the comb-drive actuators, which can cause pull-in at high frequency actuation. For our system a minimum doping concentration of $1 \times 10^{16}\,\mathrm{cm}^{-3}$ still is acceptable.

4.2.3 Temperature profile and power flow balance

This section will describe the temperature profile over the heaters and the power flow balance in the sensor for varying stage overlap. When the stage is at a fixed position, the power flows in the sensor should be in an equilibrium situation; the supplied electrical power must be equal to the heat flow from the heaters towards the environment. The power flow balance is dependent on the stage overlap. When the stage is in front of the heater structure (maximum overlap), this results in a lower heater temperature and therefore a lower heater resistance. Due to the lower resistance, more electrical power will be dissipated in the heater. This effect can be seen in the sum of the power flows in Table 4.1. When the stage moves

Table 4.1: Calculated power flow balance in the heaters for maximum, half and minimum stage overlap. The heaters in this simulation have the following dimensions: heater width and air gap 3 µm, heater length 610 µm (sensing part 130 µm and legs 240 µm), heater height 50 µm and substrate gap 3 µm. The doping concentration is 3.5×10^{18} cm^{-3}. A constant voltage of 8.3 V was applied to the heaters.

	Maximum overlap (mW)	**Half overlap (mW)**	**Minimum overlap (mW)**
Bondpads	55	56	57
Stage	14	8	2
Substrate	15	18	21
Radiation	0	0	0
Sum	**84**	**82**	**80**

in front of the heater, more power will flow towards the stage. As a result the heater will cool down and the power flows towards bondpads and substrate will decrease. Table 4.1 shows the power flow balance in the sensor for maximum, half and minimum overlap with the stage. A constant voltage of 8.3 V is applied to reach a maximum temperature of 600 K at minimum overlap. The differential sensor dissipates a more or less constant amount of power, independent on stage position. When the stage is in one of its outer positions, one of the heaters will have minimum overlap and one of the heaters will have maximum overlap. The power dissipation in this case 80 mW + 84 mW = 164 mW. When the stage is in neutral position, both heaters will have half overlap and the total power dissipation will be 82 mW + 82 mW = 164 mW.

The difference in power flow from the heater to the stage q_{stage} between maximum and minimum overlap results in the temperature change in the heater. The power flows towards bondpads q_{bondpad} and substrate $q_{\text{substrate}}$ can be seen as power loss. Most of the power in the sensor will flow through the silicon heater structure towards the bondpads. This power flow is a direct result of the high thermal conductivity of silicon compared to that of air. By decreasing the heater width, the ratio between the power flow towards the bondpads and the power flow towards the stage will change, resulting in a more sensitive sensor. This effect will be discussed in Section 4.2.4. Decreasing the heater height, which is in fact the thickness of the device layer of the SOI-wafer, will have less effect on the sensor sensitivity, since it will reduce the thermal conduction to the bondpads as well as the thermal conduction towards the stage.

For the same sensor configuration used to determine the power flow balance (Table 4.1), the modeled temperature profile over the heater for different stage overlaps is shown in Figure 4.6. At minimum overlap the heater structure will reach the highest temperature. In this case the maximum temperature is limited to 600 K. When the stage partially overlaps the heater structure, the heater structure cools down and the temperature profile becomes asymmetric. Eventually, when

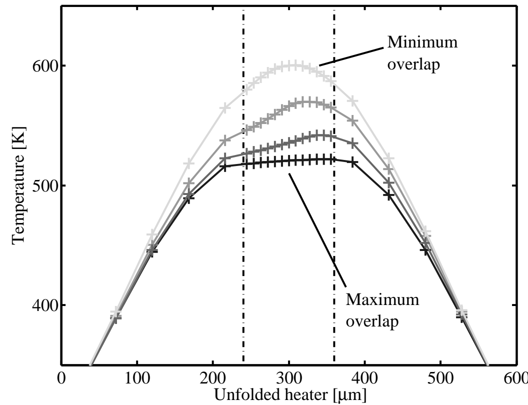

Figure 4.6: The modeled temperature profile over the heaters is a function of the stage overlap. The heater, sensing part and legs, is unfolded over the x-axis. The sensing part of the heater is in between 240 μm and 360 μm (vertical dashed lines). The maximum temperature is 600 K at minimum overlap and 522 K at maximum overlap. The curves in between correspond with the temperature profiles of 36% and 73% overlap.

the stage is completely in front of the heater structure, the maximum temperature of the heater structure has been decreased to 522 K. The temperature profile is roughly symmetric again. As a result of this temperature change, the heater resistance will decrease from 840 Ω to 790 Ω, which is approximately -6% of the initial resistance.

Due to its elevated temperature, considerable thermal expansion of the sensor structures is expected. The heater legs as well as the sensing part will expand, which results in outwards bending of the heater legs and bending of the sensing part towards the stage. Finite element simulations using COMSOL showed a reduction of the air gap between the heater and the stage of 150 nm for a maximum heater temperature of 700 K. This results in a higher sensor sensitivity and extra non-linearity. In the calibration of the sensor output voltage with respect to the displacement, the effect of thermal expansion is compensated for.

In the chosen geometry with relatively compliant heater legs, compressive forces due to the thermal expansion of the sensing part of the heater at an operating temperature of 700 K are at least 100 times lower than the force required for buckling of the sensing part. If the sensing part is too rigidly clamped or the sensing part is very thin, buckling might occur. Since buckling will probably cause mechanical as well as electrical failure, this is a situation that must be avoided.

4.2.4 Influence of heater dimensions

The dimensions of the heaters will have influence on the sensitivity of the sensor. The height of the heaters is the same as the thickness of the device layer of the

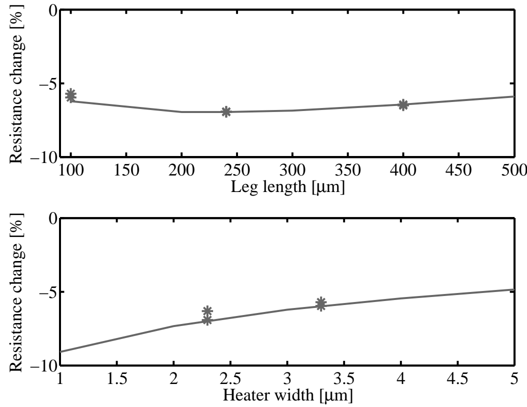

Figure 4.7: The resistance change from minimum to maximum overlap of a single heater structure as a function of variation in leg length (top) and heater width (bottom) is modeled (lines) and measured (stars). In the simulation the maximum temperature at minimum overlap is set to 600 K, in the measurement this is realized by increasing the voltage until the same resistance change as in the model to reach 600 K was measured.

SOI-wafer. For a device layer thickness of 50 µm the optimum in heater length and width is modeled. The mimimum length of the sensing part is determined by the required stroke of the stage, only the length of the legs of the heater is varied. The sensor sensitivity as a function of the leg length is shown in Figure 4.7 (top). The influence of the heater leg length is validated by measurements using heaters with three different leg lengths: 100 µm, 240 µm and 400 µm. The fabrication process puts restrictions on the minimum width of the heaters. Two heater widths are tested, 2 µm and 3 µm. The measurement results are shown together with the simulation results in Figure 4.7 (bottom). On the vertical axis the resistance change of a single heater from minimum to maximum overlap is given. The width of the designed structures is 2 µm and 3 µm. The produced structures do have an additional width of approximately 0.3 µm, as shown by scanning electron micrographs. The difference between the designed and fabricated widths is probably caused by the resist developing step after photolithography in the fabrication process. Consequently, the air gaps towards the stage reduce to 2.7 µm. The simulation results are compensated for this effect.

The simulation data shows that there exists an optimum in the leg length, but the variation in leg length does not result in a large changes of the sensitivity. For a sensor with heater width and air gap 3 µm, heater height 50 µm, substrate gap 3 µm and doping concentration $3.5 \times 10^{18}\,\mathrm{cm}^{-3}$, the optimum leg length is 240 µm. The existence of an optimum in leg length can be explained by looking at the power flows from the heaters towards the substrate and towards the bondpads. At a fixed temperature of the heater and with a fixed overlap, for short heater legs the power flow towards the bondpads will increase due to a lower thermal resistance towards

the bondpads. For long heater legs the power flow towards substrate will increase due to a large area underneath the sensor. Both these power flows can be seen as a loss in sensitivity. In the simulation a maximum temperature at minimum overlap of 600 K was chosen. In the measurement this was realized by increasing the voltage until the same resistance change as in the model was measured to reach 600 K. The measurements on the leg length variation indeed show that there exists an optimum in leg length. The exact location of the optimum cannot be obtained from this limited number of measurements. The measured resistance change from minimum to maximum overlap (with respect to minimum overlap) of a single heater for a leg length of 240 µm is -6.95%, on average over two heaters. For 100 µm, the resistance change is -5.84% and for 400 µm the resistance change is -6.48%.

The effect of the heater width is also simulated and validated using measurements, see Figure 4.7 (bottom). The simulation clearly shows that a lower heater width will result in a higher resistance change when going from minimum to maximum overlap. For two heater widths the resistance change is measured; a heater width of 2.3 µm gives an average resistance change of -6.62% and a heater width of 3.3 µm gives an average resistance change of -5.84%.

A large variation in the measurements at 2.3 µm width is shown in Figure 4.7. We propose that this is caused by irregularities in the production process when fabricating thinner structures. Structures with a designed width of 2 µm and less are actually outside the window of our fabrication process, because we cannot fabricate photolithographic masks with smaller features. Although there is a fairly large variation in the measurement results for a heater width of 2.3 µm, the accuracy of the lumped capacitance model is within 10% with respect to changes in heater width and heater leg length.

4.2.5 Operating mode and setpoint

The lumped model of the thermal displacement sensor is used to investigate the influence of the applied voltage on the sensor sensitivity. Figure 4.8 shows that the sensitivity is highly dependent on the applied voltage to the heaters. The simulation data is validated using measurements. The sensitivity curve shown here is closely related to the sensitivity curve as a function of operating temperature, shown in Figure 4.5, since a higher applied voltage will result in a higher temperature of the heaters.

In the simulations the maximum sensitivity $S_{\max}$ is 1.30 Ω/µm at a supply voltage of 9.7 V. In our measurement, the maximum sensitivity is slightly lower, 1.25 Ω/µm, at a supply voltage of 10 V. In general, the measured sensitivity values occur at a higher supply voltage than in the simulation. This causes the largest deviation at high operating voltages. The accuracy of the model is within 10% with respect to the measured values on the positive slope of the sensitivity curve.

An explanation for the deviation between the simulation and the measurements might be that the maximum temperature in the measurement is lower than in the

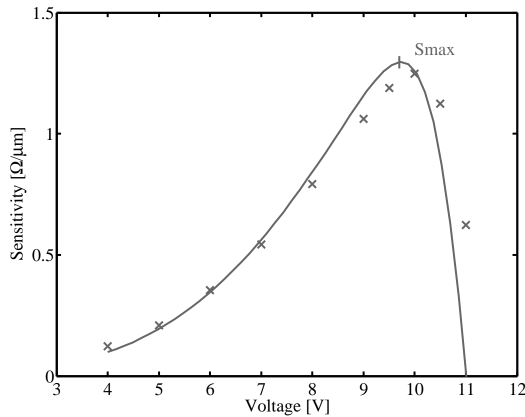

Figure 4.8: The sensitivity of the sensor is highly dependent on the applied voltage setpoint. The continuous line gives the simulation data, the measurements are indicated by stars. The heaters in this sensor have the following dimensions: heater width 3.3 µm and air gap 2.7 µm, heater length 350 µm (sensing part 150 µm and legs 100 µm), heater height 25 µm and substrate gap 3 µm. The doping concentration in this simulation is $4.7 \times 10^{18}\,\mathrm{cm}^{-3}$.

simulation, causing a shift in the optimum supply voltage. A possible cause for the lower maximum temperature is a resistance in series with the MEMS heater structures, for instance on the wire bond to silicon interface. This series resistance will cause the effective voltage over the heater structure to drop. A second explanation is that the temperature dependence of the thermal capacities or the thermal resistances is not modeled correctly. Finite size effects due to downscaling cannot be the origin of the deviation. In silicon and silicon dioxide layers thicker than 1 µm, finite size effects should be negligible [5, 130], which is the case in our sensors. The thermal conductivity of the air gap suffers from finite size effects on the boundary layer between silicon and air [33]. These boundary effects in fact increase the effective width of the air gap, which would result in a shift of the sensitivity peak in simulation towards lower temperatures. This does not match with our measurements.

The model of the sensor is also used to determine the influence of different operating modes. Two operating modes are a) applying a constant voltage and measuring the current and b) applying a constant current and measuring the voltage. Other possibly interesting operating modes, which were not investigated, are controlling the voltage or current in order to create a constant power dissipation or to create a constant heat flow towards the stage, independent on the stage overlap.

The effect of applying a constant voltage or a constant current to the heater structures is shown in Figure 4.9. By applying a constant current to the sensor, the maximum sensitivity is 2.7 times higher than by applying a constant voltage.

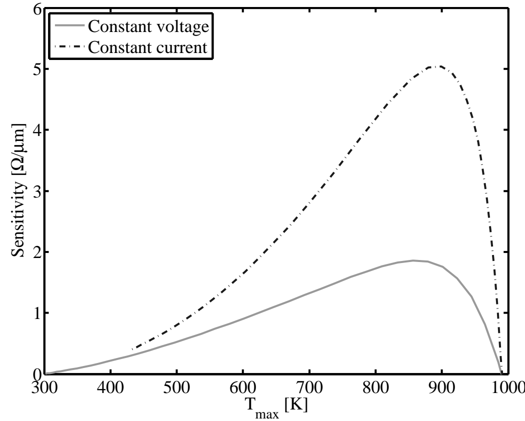

Figure 4.9: There is a difference between driving the heaters with a constant voltage and with a constant current. The temperature shown on the horizontal axis is the maximum heater temperature at minimum overlap. The maximum sensitivity of the sensor is around 2.7 times higher when a constant current is applied to the sensor. The heaters have the following dimensions: heater width and air gap 3 µm, heater length 610 µm (sensing part 130 µm and legs 240 µm, heater height 50 µm and substrate gap 3 µm. The doping concentration in this simulation is 3.5×10^{18} cm^{-3}.

This can be understood by looking at the equations for power dissipation in the heater structures:

$$P_{\mathrm{U}}(T) = \frac{U^2}{R_{\mathrm{E}}(T)} \tag{4.8}$$

$$P_{\mathrm{I}}(T) = I^2 R_{\mathrm{E}}(T) \tag{4.9}$$

If a situation is considered with constant voltage, at minimum overlap the heater will reach a certain (high) temperature and therefore a (high) resistance. If the stage is moved to maximum overlap, the heater structure will cool down and the resistance will decrease. According to (4.8) this will result in an increase of the power supplied to the sensor. This increase in power increases the heater temperature, which counteracts the decrease in temperature by more stage overlap. If a constant current is chosen, from minimum to maximum overlap, the resistance will decrease and according to (4.9) the power supplied to the sensor will also decrease, which amplifies the cooling effect of the stage displacement. Applying a constant current can lead to instability when the sensor is operated close to and beyond S_{max}.

The operating mode of the sensor also influences the time it takes for the heater to react on a change in stage position, i.e. the thermal time constant of the heater. When a low heater current or voltage is used, this will lead to a certain low resistance. When a step is made in the supply voltage, the low initial resistance leads to an initial power that is higher than the final power, according to (4.8).

When a step is made in the applied current, the low initial resistance leads to an initial power that is lower than the final power, according to (4.9). As a result the temperature of the heater will increase more quickly with a constant supplied voltage than with a constant applied current. Simulations with the lumped model show that the current mode will result in a time constant that is roughly 2 to 3 times higher than the time constant in voltage mode.

4.3 Design

The modeling section, Section 4.2, shows the influence of the parameters such as doping concentration, operating temperature, heater leg length and heater width on the sensitivity of the sensor. Several conclusions can be drawn from modeling.

The doping concentration in the device layer of the SOI wafer does affect the sensitivity of the sensor. Choosing a low doping concentration will result in a sensor with increased sensitivity. For our system a minimum doping concentration of $1 \times 10^{16}\,\mathrm{cm}^{-3}$ still is acceptable, based on the the increasing electrical time constant when decreasing the doping concentration. For this research SOI wafers with two different doping concentrations were available, $3.5 \times 10^{18}\,\mathrm{cm}^{-3}$ and $4.7 \times 10^{18}\,\mathrm{cm}^{-3}$.

The sensitivity of the sensor as a function of the operating temperature shows that this function is closely related to the resistivity curve of silicon as a function of temperature. Up to a certain maximum operating temperature setpoint the sensitivity will increase. Above this temperature setpoint, the sensitivity of the sensor will decrease. In this work the sensor is operated on the positive slope of the sensitivity curve.

The heater width should be chosen as small as possible to result in a sensor with a higher sensitivity. The minimum width of the heaters is restricted by the fabrication process. A minimum feature size of 3 µm is recommended for reliable fabrication. Sensors with designed heater widths of 2 µm and 3 µm have been produced.

Varying the leg length of the heaters will result in a sensitivity curve that has an optimum. For a heater width and air gap of 3 µm, a doping concentration of $3.5 \times 10^{18}\,\mathrm{cm}^{-3}$, a device layer thickness of 50 µm, a sensing part length of 130 µm and a substrate gap of 3 µm the optimum leg length is 240 µm. Sensors with various leg lengths have been produced. Section 4.2.5 showed that the sensor should be used in current mode. This means that a constant current is applied to the heaters and that the voltage over the heaters is a measure for the stage position. With the same sensor configuration and depending on the temperature setpoint, applying a constant current results in a sensitivity that is up to 2.7 times higher than in voltage mode.

The differential sensor is integrated in the system design. In a first production run a proof of the sensor principle was given [48, 72]. In this production run a SOI wafer with device layer 25 µm, oxide layer 1 µm and doping concentration $4.7 \times 10^{18}\,\mathrm{cm}^{-3}$ was used. The moving stage is actuated using electrostatic comb-

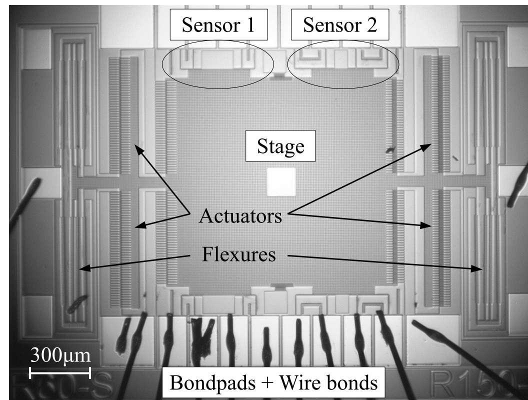

Figure 4.10: Top view, optical micrograph of the proof of principle system. The comb-drive actuators in combination with the guidance mechanism are able to enable stage displacements up to 30 µm in both directions. Four differential sensors with different geometries are connected to a single stage. Only the two sensor pairs on the top side of the stage are indicated here, two more sensor pairs are located on the bottom side of the stage.

drives [80]. The stage used folded flexures as a straight guidance mechanism to ensure parallel movement with respect to the heaters. The displacement obtained using the folded flexure straight guidance is limited to roughly 30 µm in both directions. For larger displacements, the stiffness of the guidance mechanism in the direction perpendicular to the direction of motion of the stage is not sufficient to prevent the complete stage from snap-in due to electrostatic forces. This proof-of-principle system is shown in Figure 4.10. Various differential sensors with different heater geometries are connected to a single stage. A gold layer was added to the bondpads to facilitate the connection with the wire bonds.

In a second production run, the straight guidance mechanism using four folded flexures is replaced by two constrained folded flexures [12]. This straight guidance mechanism can reach displacements up to 100 µm in both directions. A SOI wafer with device layer 50 µm, oxide layer 3 µm and doping concentration $3.5 \times 10^{18}\,\mathrm{cm}^{-3}$ was used. No gold deposition layer was used in the second production run, but wires were bonded directly onto the silicon.

4.4 Fabrication

For both production runs described in Section 4.3, aspect-ratio controlled deep reactive-ion etching (DRIE) was used to etch through the full device layer of the wafer. The directional etching and resulting high aspect ratios are particularly useful for good mechanical behaviour of the leafsprings used for straight guiding the stage, resulting in low driving stiffness and high transversal- and out-of-plane

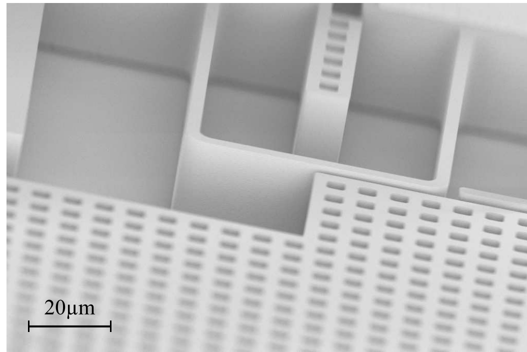

Figure 4.11: Scanning electron micrograph of a fabricated heater in front of the stage. This heater was part of the first production run, using wafers with a device layer of 25 µm and an oxide layer of 1 µm.

stiffness. A minimum trench width and a minimum feature size of 3 µm is used in the design, limited by the aspect ratio of the DRIE step and limited by the resolution of the fabrication of the photolithographic masks. A maximum trench width of 50 µm is used to prevent large variations in etch loading. Etch loading influences the etch rate and the subsurface profile development [58]. For this reason several etch compensation structures are included in the design, as depicted in Figure 4.2. After reactive-ion etching, the structures were released from the substrate by isotropic HF vapour phase etching of the buried oxide layer [49]. Thin structures (<10 µm) are released from the substrate in this way. Large structures will stay mechanically fixed to the substrate, while being electrically isolated from the substrate due to the oxide layer. Large bodies that should be floating, are perforated to be released from the substrate. The fabricated devices are diced, glued and wire bonded with thin aluminium wires to a printed circuit board for measurement. A scanning electron micrograph of a sensor from the first production run is shown in Figure 4.11.

4.5 Experiment

In this section the measurement setups will be described first. Subsequently the sensor output voltage as a function of the displacement, the sensor noise and the time constants of the system are discussed.

4.5.1 Measurement setup

Two different measurement setups were developed to characterize the fabricated sensors. One setup applies a constant current and measures the voltage over the heaters, the other setup applies a constant voltage and measures the current

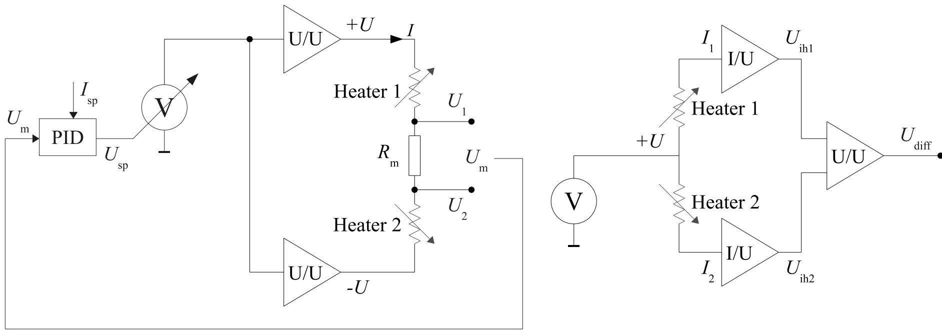

Figure 4.12: Schematic overview of the measurement setups for current (left) and voltage (right) mode. For constant current, the measured voltage U_m over the resistor R_m is used to determine the current through the heaters. The driving voltage ($+U$ and $-U$) is adjusted to control the current through the heaters (I) using the current setpoint I_{sp}. The advantage of this half bridge measurement setup is that the output voltages U_1 and U_2 have little offset and can be directly used for A/D conversion with little quantization noise. For constant voltage, a well defined constant voltage source is used to drive the heaters. The resulting currents through the heaters (I_1 and I_2) are amplified using two equal current-to-voltage amplifiers. A second, differential amplifier is used to generate the signal (U_diff) for A/D conversion. (Color version: The digital part of the measurement setup is depicted in blue, the MEMS structures are depicted in red.)

through the heaters. The current control setup, Figure 4.12 (left), places two heaters in series, so equal current through both heaters is guaranteed. The current through the heaters is measured by the voltage over the low-impedance resistor R_m. The voltage source is adjusted to generate a constant current I through the heaters. The sensor output is the voltage on either of the electrodes of the resistance R_m with respect to ground. The bandwidth of the control loop limits the bandwidth of the sensor in this configuration. The measurement setup for voltage control, Figure 4.12 (right), is more straightforward, but requires more analog electronics. A voltage supply is directly connected to both heaters in parallel. The resulting currents are amplified in two equal current-to-voltage amplifiers. A differential amplifier is used to generate the measurement signal.

A secondary measurement setup is used to calibrate the stage deflection as a function of the actuation voltage on the comb-drives. Stroboscopic video microscopy is used for this purpose, performed with a Polytec MSA-400 and its Planar Motion Analyzer software [106]. The measured data provides accurate information ($1\sigma \sim 20\,\mathrm{nm}$) about the stage position at a specified actuation voltage. The comb-drive actuators in combination with the flexure based stage are designed to generate the required $100\,\mu\mathrm{m}$ deflection at a maximum voltage of $80\,\mathrm{V}$.

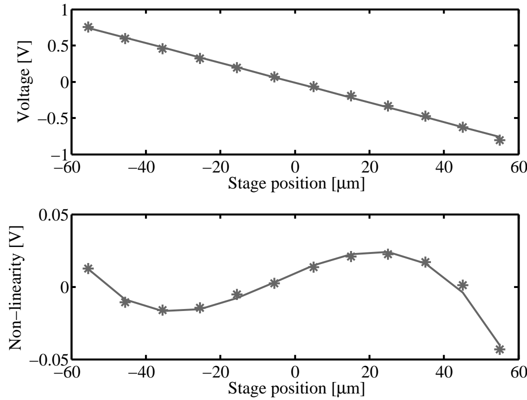

Figure 4.13: The measured voltage output as a function of the stage displacement is shown for the situation that a constant current of 9.8 mA is applied (top). A linear fit is made with slope −13.7 mV/μm and offset −12.5 mV. The deviation from the linear fit, can be approximated by a third order polynomial (bottom). The heaters in this experiment have the following dimensions: heater width and air gap 3 μm, heater length 610 μm (sensing part 130 μm and legs 240 μm), heater height 50 μm and substrate gap 3 μm. The doping concentration of this wafer is $3.5 \times 10^{18}\,\mathrm{cm}^{-3}$.

4.5.2 Sensor output and noise

At a constant heater current of 9.8 mA, the displacement versus the sensor output voltage was measured and shown in Figure 4.13 (top). The current is chosen such that a maximum heater temperature at minimum overlap of 800 K is expected. The stage movement in this experiment is from −55 μm to 55 μm. The measured voltage U_2 ranges from −0.807 V to 0.758 V. The resistance of heater 1 decreases from 1108 Ω to 963 Ω and the resistance of heater 2 increases from 953 Ω to 1127 Ω. This corresponds to an average sensitivity of 2.91 Ω/μm.

The linear fit through the measured data has a slope of −13.7 mV/μm. The deviation from a linear fit is measured to be at maximum 23 mV, which corresponds to approximately 1.6 μm. Considering all non-linear effects in the sensor, for instance the electrical resistivity of silicon as a function of the temperature, and the fairly large temperature variation over the sensing part of the heater, the differential sensor is surprisingly linear. The nonlinearity of the sensor is highly repeatable and can be fitted with a third order polynomial with minor deviation, as shown in Figure 4.13. This is necessary for accurate positioning.

The noise of the unfiltered sensor signal has an RMS value of 122 μV at a sampling frequency of 1 kHz. If the noise is assumed white, this leads to a noise value of $3.9\,\mu\mathrm{V}/\sqrt{\mathrm{Hz}}$. Using the slope of 13.7 mV/μm this yields $0.28\,\mathrm{nm}/\sqrt{\mathrm{Hz}}$. The noise of the measurement setup is dominated by the specified RMS noise of the 16-bit A/D converter, which is 98.1 μV. The measurement signal is digitally

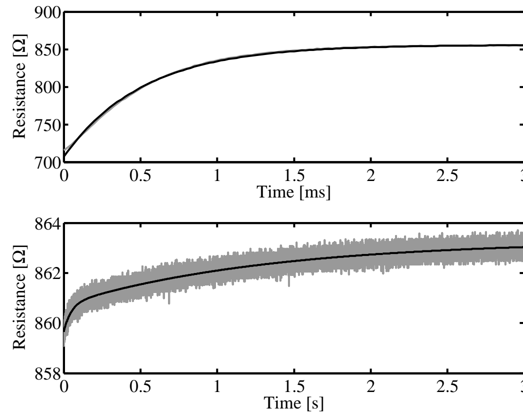

Figure 4.14: This sensor structure has a time constant τ_{heater} of 522 µs (top). Two more time constants can be distinguished; the stage has a time constant τ_{stage} of 50.8 ms and the complete system has a time constant τ_{system} of 1.32 s (bottom). The measurement results are depicted in light grey and the exponential fits in black. The heaters in this experiment have the following dimensions: heater width and air gap 3 µm, heater length 610 µm (sensing part 130 µm and legs 240 µm), heater height 50 µm and substrate gap 3 µm.

filtered with a 6th order low-pass filter with a cut-off frequency of 25 Hz. The filtered signal has an RMS noise value of 22.2 µV, which corresponds to a sensor resolution of 1.65 nm.

4.5.3 Time constants and drift

An important drawback of thermal systems usually is the low bandwidth due to high thermal time constants. With a thermal sensing or actuation principle in MEMS, much higher bandwidths can be achieved. The thermal capacitance ($C \sim r^3$) decreases much faster due to miniaturization than the thermal resistance increases ($R \sim r^{-1}$). Therefore the time constant will decrease quadratically with decreasing size ($\tau = RC \sim r^2$). In order to measure the time response of the heaters, a voltage step was applied to one of the two heaters of the sensor. The resistance of the heater was measured at a high sample rate, see Figure 4.14 (top). The heater structure has a time constant τ_{heater} of 522 µs, which means the sensor has a bandwidth (−3 dB) of 305 Hz.

The time constant of the heater structure is not the only time constant in the complete system. By applying a step voltage to the second heater in the sensor and measuring the response on the first heater, two more time constants are found, Figure 4.14 (bottom). A time constant τ_{stage} of 50.8 ms was found that can be attributed to the time constant of the stage and a time constant τ_{system} of 1.32 s was found that is caused by heating of the complete system and substrate.

Continuous usage of the sensor can prevent τ_{system} from showing up, because the power dissipation of the sensor is more or less constant, independent on stage position, as shown by the simulations in Table 4.1. The stage time constant τ_{stage} is harder to suppress, since at every stage movement the temperature distribution over the stage changes. The influence of the stage time constant can be reduced by choosing an operating mode of the sensor in which the power flow towards the stage for each heater is constant or by adding a stage position history in the sensor that compensates for the stage time constant. In both cases information of the model is used to make predictions about the power flows and time constants in the sensor, based on the applied current or voltage and the previously known positions. For control, the relatively large time constant of the stage does not lead to large phase shifts or instability, therefore the control bandwidth is not limited by the stage bandwidth.

A drift measurement was performed with the differential sensor. Without control of ambient temperature and air humidity, the drift of the sensor was determined to be 32 nm over a measurement period of 32 hours. A 'run-in' time of several days was required to remove this long-term drift. Both ambient temperature and air humidity do influence the sensor response. These effects can be compensated for by using a reference sensor with a fixed overlap that purely measures environmental fluctuations. A long-term drift of single heater resistances was observed over a time period of more than 100 hours. Even when using the heater at 'reasonable' temperatures, around 600 K, the resistance increases irreversibly with roughly 5% with respect to the initial resistance. For example thermal oxidation [123] and thermal activation of oxygen [13] are effects that can change the properties of the silicon material slightly. Electromigration and diffusion effects due to fairly high current densities on the wire bond to silicon interface are difficult to predict, but can also have a significant influence. Frequent internal calibration of the sensor by hard mechanical endstops will be used to compensate for long-term drift effects.

4.6 Conclusion

This work presents a MEMS displacement sensor based on the conductive heat transfer of a resistively heated silicon structure towards an actuated stage parallel to the structure. Using the heaters in a differential configuration and using a typical sensor design, an RMS position noise of 2 nm was measured. This resolution was measured over a range of 110 µm and after filtering with a bandwidth of 25 Hz. Due to the small scale of MEMS structures the thermal sensing principle can achieve reasonably high bandwidths, in contrast with thermal systems in the macro world.

A dynamic multiphysics lumped capacitance model was generated to optimize the sensor sensitivity as a function of doping concentration, operating temperature, heater leg length and heater width. The accuracy of the model is within 10% with respect to the measured values on the positive slope of the sensitivity curve.

Sensitivity changes due to a variation in the heater leg length and the heater width can be predicted within the same accuracy.

Based on this model, we conclude that the heater width should be designed as small as allowed by the fabrication process. An optimum in the heater leg length exists, but does not have a large influence on the sensitivity. Constant current supplied to the heaters, rather than constant voltage, results in a higher sensitivity. A decrease in doping concentration will also increase the sensitivity of the sensor substantially.

An important conclusion is that the differential sensor can be easily incorporated in a silicon-on-insulator (SOI) based process, and fabricated within the same mask as electrostatic actuators and flexure based stages. The sensor including bondpads requires only little wafer surface area ($<0.5\,\mathrm{mm}^2$). With nanometer resolution, the presented thermal displacement sensor is an interesting sensor for accurate positioning systems.

Chapter 5

Vacuum behavior and control of a MEMS stage with integrated thermal displacement sensor

We investigate the applicability of a MEMS stage in a vacuum environment. The stage is suspended by a flexure mechanism and is actuated by electrostatic comb-drives. The position of the stage is measured by an integrated sensor based on the conductance of heat through air. The vacuum behavior of the sensor and the stage is identified. A model for thermal conductivity and viscous damping as a function of the vacuum pressure is presented and validated by measuring the decreasing sensor response and the increasing Q-factor for decreasing pressure. We have identified the system in the frequency domain, which is used to compare the closed-loop behavior with three different controllers: an integral controller, an integral controller with low-pass filter, and an integral controller with notch filter. The integral controller can become unstable due to the high Q-factor in vacuum. Adding a low-pass or a notch filter improves the stability at low pressures. Since the integral controller with notch filter shows the lowest settling time, this is the preferred controller. Overall, we conclude that stable position control of the MEMS stage is possible for pressures down to 1 mbar.

This chapter is submitted as 'B. Krijnen, D.M. Brouwer, L. Abelmann, and J.L. Herder. Vacuum behavior and control of a mems stage with integrated thermal displacement sensor. *Sensors and Actuators A: Physical*, 2014 (submitted)'.

5.1 Introduction

Manipulators for confined vacuum chambers are becoming increasingly important for future applications in scanning electron microscopes (SEMs) and transmission electron microscopes (TEMs). Typically SEMs and TEMs operate at vacuum pressures below 1×10^{-6} mbar. Environmental SEMs (eSEMs) offer the possibility of making electron microscopy images in gaseous environments at higher pressures, up to 20 mbar, so that 'wet' samples can be investigated. Applications include maneuverable phase plates, TEM sample manipulators, and in-situ sample straining. An example of a MEMS-based device for in-situ sample straining is shown in [133]. Large manipulators, as shown in [25] and [94], can be avoided by using a MEMS-based stage. A MEMS-based sample manipulator is shown in [28], but this stage does not include feedback and is not characterized in vacuum.

The main objective of this paper is to investigate the applicability of a closed-loop MEMS-based positioning stage in a vacuum environment. For this reason we want to 1) characterize the sensor response and stage dynamics as a function of pressure, and 2) perform stable position control of the stage using an integrated sensor.

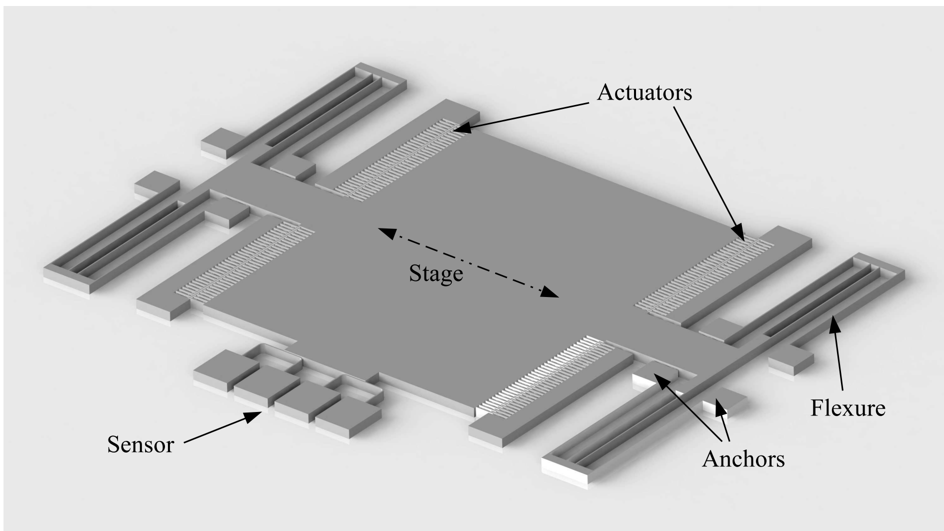

Figure 5.1: An overview of the comb-drive actuated stage is given. Due to four flexure mechanisms, the stage is able to move along a straight line. The anchors are connected to the handle wafer underneath and therefore stay in place. A thermal displacement sensor gives feedback on the stage position.

An overview of the MEMS stages we have used in this work is given in Figure 5.1. The stage is suspended by folded flexures to constrain the movement of the stage to a straight line and to prevent the stage from pull-in due to lateral

forces generated by the electrostatic actuators [124, 80]. Feedback is provided by a thermal displacement sensor that we have published before [73]. Each sensor consists of two silicon heaters that are resistively heated by applying a fixed voltage. The temperature of the heaters changes due to a varying overlap with the 'cold' stage. The resulting change in electrical resistance is measured.

Resonating stages in MEMS are often used as sensors. Such resonators require vacuum packaging to increase their performance by removing the viscous damping effect of a gas (air) [81, 82, 63, 20]. Examples are structures for time keeping, gyroscopes, accelerometers, pressure sensors, and even musical instruments [19, 115, 34, 38]. The decrease of viscous damping in a vacuum environment is addressed in most of these publications, resulting in resonators with a higher Q-factor. The effect of the reduced thermal conductivity of the air in a MEMS structure has been less well studied. The decreasing thermal conductivity of air as a function of the pressure with characteristic dimensions of several micrometers is used, for example, in Pirani gauges [37, 4, 117]. Thermal sensors for measuring the position of a MEMS stage have been reported before, but their vacuum behavior is not mentioned [78, 26, 105, 73]. Although many actuated MEMS stages have been reported with integrated sensors, only a few have been actually used for control, for example [22, 18, 53, 101]. Position feedback in these papers is provided by capacitive or piezoresistive position sensors. Pantazi et al. [103] and Zhu et al. [132] demonstrate controlled MEMS stages with thermal position sensors. The reported positioning stages are not intended for use in a vacuum environment and so their controllers are not designed to handle the decreasing sensor sensitivity and increasing Q-factor.

Summarizing, the main contributions of this paper are 1) the quantitative characterization of the thermal displacement sensor in a vacuum environment from 1 mbar to 1 bar, 2) the identification of the complete stage in the frequency domain at four different pressures, and 3) the design of a simple and stable position controller for the MEMS stage, taking into account the decreasing sensor sensitivity and increasing Q-factor in vacuum.

Section 5.2, 'Theory', gives analytical expressions for the thermal conductivity and viscosity of air as a function of the pressure. These analytical expressions are used to model the Q-factor of the MEMS stage and the sensor response. We expect the MEMS stage to behave as a mass–spring–damper system in the frequency domain (Section 5.2.1.4), on which we base our controller design (Section 5.2.2). Section 5.3, 'Experimental', describes the fabrication process of the MEMS devices and the measurement setups used for characterization of our devices. In the 'Results' section the actuator, the sensor and the mechanics are characterized quasi-statically as a function of the pressure (sections 5.4.1.1 to 5.4.1.3). At four different pressures a frequency domain identification of the MEMS stage is performed (Section 5.4.1.4). Finally, stable position control of the stage is shown by using the integrated sensor (Section 5.4.2).

5.2 Theory

The theory section consists of two parts. In Section 5.2.1 the models that describe the vacuum behavior of the stage are given and in Section 5.2.2 the control strategy for the stage is introduced.

5.2.1 Vacuum behavior

This section presents the analytical and simulation models that are used to describe the vacuum behavior of the MEMS stage. The electrostatic actuator is covered in Section 5.2.1.1, the sensor response is given in Section 5.2.1.2, and the damping of the flexure-based mechanism is described in Section 5.2.1.3. These three quasi-static models are combined into a dynamic model of the complete system in Section 5.2.1.4.

5.2.1.1 Capacitance

The actuation force of an electrostatic comb-drive is given by Legtenberg [80],

$$F_{\mathrm{act}} = \frac{N\epsilon_0\epsilon_{\mathrm{r}}hU^2}{g}. \tag{5.1}$$

In this equation, N is the number of finger pairs, h is the height of the comb-drive, in our case the thickness of the device layer of 25 µm, U is the actuation voltage in V, g is the air gap between the comb-drive fingers in m, ϵ_0 is the vacuum permittivity of $8.854\,\mathrm{F\,m^{-1}}$, and ϵ_{r} is the relative permittivity of air. Since the relative permittivity of air is very close to one (1.0006), we do not expect to measure a variation of the stage displacement as a function of the pressure.

5.2.1.2 Thermal conductivity

The behavior of a gas is highly dependent on the state of the gas. The state of the gas is determined by the relation between the mean free path λ of the gas molecules and a characteristic dimension D of the volume surrounding the gas. The ratio λ/D is called the Knudsen number Kn and describes the ratio between the number of collisions between the gas molecules and the amount of collisions with the surrounding surface. Traditionally, three regimes are distinguished to describe the behavior of a gas: the continuum regime ($\mathrm{Kn} < 0.01$), the free-molecule regime ($\mathrm{Kn} > 10$), and the transition regime ($0.01 < \mathrm{Kn} < 10$) [14].

The mean free path of air molecules is given in [16],

$$\lambda = \frac{k_{\mathrm{B}}T_{\mathrm{air}}}{\sqrt{2}\pi d^2 p}; \tag{5.2}$$

in which k_{B} is the Boltzmann constant, $1.38 \times 10^{-23}\,\mathrm{J\,K^{-1}}$; T_{air} is the temperature of the gas in K; d is the effective diameter of the average air molecule,

2.5×10^{-10} m; and p is the pressure in Pa. For standard atmospheric pressure, 1.01×10^5 Pa, and a temperature of 300 K this results in a mean free path of approximately 150 nm. In our MEMS stages the characteristic dimensions are between 1 µm and 3 µm, which leads to a Knudsen number of roughly 0.1 and so we need to describe the air in the transition regime. When the pressure decreases below 10 mbar, the air must be described in the free-molecule regime.

In the continuum regime, the thermal conductivity of air, k_c in W m^{-1} K^{-1}, is described by the kinetic theory of gases [16],

$$k_\mathrm{c} = \rho c_\mathrm{v} v_\mathrm{rms} \lambda / 3. \tag{5.3}$$

In this equation, ρ is the density of air in kg m^{-3}, c_v is the heat capacity of the gas at a constant volume in J kg^{-1} K^{-1}, and v_rms is the root mean square velocity of the gas molecules in m s^{-1}. In the continuum regime, the thermal conductivity of a gas is constant, since ρ increases proportionally with the pressure and λ decreases reciprocally with the pressure (c_v and v_rms are constant with pressure).

In the free-molecule regime, the heat transfer is highly dependent on the temperature jump at the interface between the gas and the solid. The energy interaction due to a collision of an air molecule with the wall is described by the thermal accommodation coefficient α_T,

$$\alpha_\mathrm{T} = \frac{T_\mathrm{i} - T_\mathrm{r}}{T_\mathrm{i} - T_\mathrm{w}}. \tag{5.4}$$

The temperatures in this equation represent the incident (i), reflected (r) and wall (w) temperatures. The thermal accommodation coefficient between a gas and a solid is dependent on, for instance, the material, the surface roughness, and the diameter of the gas molecules. Typical values between between 0.8 and 0.9 are reported for oxygen and nitrogen [107]. The heat transfer in the free-molecule region between parallel plates is described by Kennard [64] and later by Corruccini [24],

$$\frac{q}{T_2 - T_1} = \frac{\alpha_\mathrm{T}}{2 - \alpha_\mathrm{T}} \frac{\gamma + 1}{\gamma - 1} \left(\frac{k_\mathrm{B}}{8 \pi m T_\mathrm{air}} \right)^{1/2} p. \tag{5.5}$$

In this equation, q is the heat transfer in W m^{-2}; γ is the ratio between the heat capacity of air at constant pressure c_p and the heat capacity of air at constant volume c_v; and m is the average mass of the air molecules, 4.82×10^{-26} kg. The heat transfer can be rewritten as a thermal conductivity coefficient for the free-molecule regime k_fm,

$$k_\mathrm{fm} = D \frac{\alpha_\mathrm{T}}{2 - \alpha_\mathrm{T}} \frac{\gamma + 1}{\gamma - 1} \left(\frac{k_\mathrm{B}}{8 \pi m T_\mathrm{air}} \right)^{1/2} p. \tag{5.6}$$

Sherman [116] describes and validates a model for the thermal conductivity in the transition regime based on the two limiting cases, the free-molecule regime and the continuum regime,

$$\frac{1}{k} = \frac{1}{k_\mathrm{fm}} + \frac{1}{k_\mathrm{c}}. \tag{5.7}$$

The normalized thermal conductivity k/k_c of air as a function of the pressure is given in Figure 5.2.

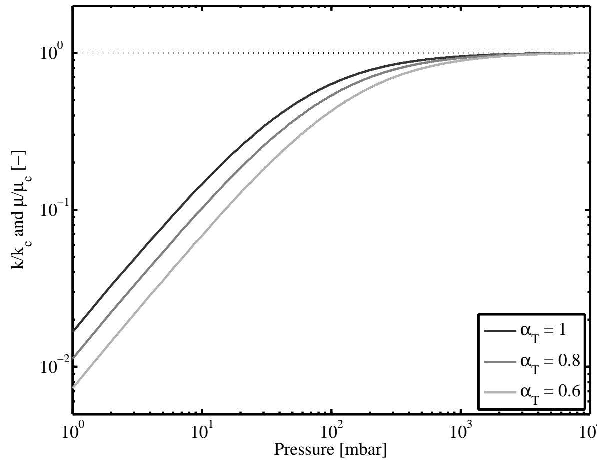

Figure 5.2: The normalized thermal conductivity k/k_c of air as a function of the pressure. Three values for the accommodation coefficient α_T have been chosen to demonstrate the effect of this parameter. The normalized viscosity μ/μ_c is equal to the normalized thermal conductivity.

The thermal conductivity of air as a function of the vacuum pressure, given in (5.7), is implemented in the lumped-capacitance model of our thermal displacement sensor that is described in [73]. This model divides the heater into 23 lumps. Each lump includes the resistive heating of silicon and its resulting increase in electrical resistance. The lumps lose their heat by thermal conductance through silicon towards the bondpads, by conductance through air towards the handle wafer and the stage, and by radiation.

5.2.1.3 Viscosity

By scaling down from a macro-scale to a micro-scale, the mass of structures ($m \sim r^3$) decreases more rapidly than the surface ($A \sim r^2$). For this reason MEMS typically suffer from much more damping due to surface effects than macro-scale machines. Two types of viscous damping of MEMS due to the surrounding air are considered: squeeze-film damping and shear stress damping. Squeeze-film damping becomes an important damping effect when the thickness of the gas film gets smaller than one-third of the width of the plate [96, 8]. In our devices, which move in the wafer plane, this means the plate width is the height of the device layer, 25 µm. So the squeeze-film effect will play a role for air gaps roughly below 8 µm. Since this is not the case in our stages, we assume that squeeze-film damping will not be the dominant damping effect.

The movement of relatively large stages ($> 1\,\mathrm{mm}^2$) with only a thin air layer

between the stage and the handle wafer (1 µm) can introduce significant shear stress damping. Newton's shear stress law gives the shear force due to the parallel movement of two plates with a viscous medium in between,

$$F_\tau = \mu A \frac{v_\mathrm{x}}{y}. \tag{5.8}$$

In this equation, μ is the dynamic viscosity of the medium in $\mathrm{N\,s\,m^{-2}}$, A is the surface area of the plates in $\mathrm{m^2}$, v_x is the velocity of the plates in $\mathrm{m\,s^{-1}}$, and y is the distance between the plates in m.

Since the viscosity and the thermal conductivity of air are both based on the same physical principle, the energy transfer at the collision of air molecules with each other and with the interface, a direct relation exists between the thermal conductivity and the viscosity of air [16],

$$\mu = \frac{4}{15}\frac{m}{k_\mathrm{B}}k. \tag{5.9}$$

In this equation, the thermal conductivity of air k derived in (5.4) to (5.7) is used. Note that instead of the thermal accommodation coefficient α_T from (5.4), a momentum accommodation coefficient α_M must be used, which also has a value roughly between 0.8 and 0.9 for air [27].

The absolute damping coefficient of the MEMS stage equals the part of (5.8) that is linear with v_x, $\mu A/y$. The absolute damping coefficient is used to calculate the relative damping and the Q-factor,

$$\zeta = \frac{\mu A/y}{2\sqrt{k_0 m_0}}, \text{ and} \tag{5.10a}$$

$$Q = \frac{1}{2\zeta}. \tag{5.10b}$$

In this equation, k_0 is the stiffness of the flexure mechanism in $\mathrm{N\,m^{-1}}$ and m_0 is the mass of the MEMS stage in kg. The surface area of the MEMS stage A is approximately $1.5\,\mathrm{mm^2}$ and the gap y between the stage and the handle wafer is 1 µm.

5.2.1.4 Frequency model

The MEMS stage consists of the subsystems as described in the previous sections. The actuator (Section 5.2.1.1), the sensor (Section 5.2.1.2), and the mechanics (Section 5.2.1.3) all contribute to the frequency domain model of the complete stage $H(s)$,

$$H(s) = A(s)M(s)S(s). \tag{5.11}$$

The transfer function of the actuator $A(s)$ is expressed in $\mathrm{N\,V^{-1}}$, the mechanics $M(s)$ in $\mathrm{m\,N^{-1}}$, and the sensor $S(s)$ in $\mathrm{V\,m^{-1}}$. The complex number s originates from the Laplace transform of a time-domain signal and thus represents the frequency.

The actuator consists electrically of a resistance in series with a capacitance, which together function as a low-pass filter. A rough estimate of the resistance, 1 kΩ, and the capacitance, 1 pF, leads to a time constant of 1 ns (160 MHz). We expect no other frequency dependent behavior in the electrostatic actuator. In the frequency range we are interested in, up to 5 kHz, we assume the actuator has a constant transfer, as given in (5.1). The frequency response of the mechanics is considered to be a basic mass–spring–damper in which the Q-factor is a measure of the damping,

$$M(s) = \frac{x}{F} = \frac{1/m_0}{s^2 + s\omega_0/Q + \omega_0^2}. \tag{5.12a}$$

In this equation, ω_0 is the undamped eigenfrequency of the stage, and is given by $\sqrt{k_0/m_0}$. The frequency response of the thermal displacement sensor is more difficult to model. From a step response in the time domain we expect a low-pass frequency domain behavior. A time constant of 150 µs was measured, which equals a cut-off frequency of 1060 Hz.

5.2.2 Control

A common block diagram for a position controller is schematically given in Figure 5.3. The 'plant' $P(s)$ in this diagram represents the MEMS stage. The electrostatic actuator generates a force and the thermal sensor measures the position of the stage. The transfer of the plant is therefore given by $x_{\mathrm{ms}}/F_{\mathrm{act}}$ in $\mathrm{m\,N^{-1}}$. The open-loop transfer function is defined as the transfer of the plant with the controller without the feedback loop, x_{ms}/e. The closed-loop transfer function is the response from input to output, $x_{\mathrm{ms}}/x_{\mathrm{sp}}$, with feedback enabled.

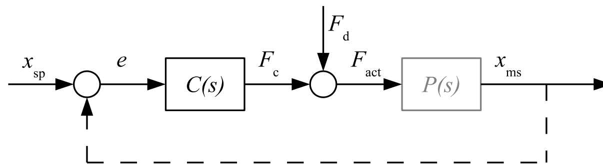

Figure 5.3: A block diagram of the complete system, consisting of the controller $C(s)$ and the plant $P(s)$. The input of the closed-loop system is the setpoint position x_{sp}, the output is the measured position x_{ms}. The feedback is indicated by the dashed line. The MEMS stage (plant) is indicated in red.

Low-stiffness mass-positioning is typically done by a basic PID-controller with or without an additional low-pass filter [114]. The controller acts as a virtual damping (D) and stiffness (P) in parallel with the actual damping and stiffness; the dynamic behavior of the system can be defined in this way. The integral action (I) is required to provide an output force when the position error is zero, which is necessary for a plant with spring behavior.

Discretization, the conversion from continuous time signals into discrete time signals, results in magnitude loss and phase delay close to the sampling frequency. To be able to neglect the influence of discretization, a rule of thumb is to choose the sample rate approximately a factor of 20 higher than the required signal frequency [126, 40]. In case of our MEMS stage with the first eigenfrequencies between 1000 Hz and 1500 Hz, this means that to add damping at this frequency we need to choose a sample rate of at least 20 kHz. However, a sample rate of 20 kHz is not easily met by every real-time platform. An alternative way to control the plant that acts as a stiffness is by only using an integral action, which is described in [128]. The crossover frequency, the frequency at which the open-loop transfer function crosses 0 dB, of the integral controller is chosen several factors below the first eigenfrequency of the system, which means the required sample rate is not extremely high in this case. The drawback of this approach is that we cannot add damping at the first eigenfrequency of the stage.

To achieve reasonably fast response times, the crossover frequency should be chosen as high as possible. On the other hand, increasing the crossover frequency decreases the stability of the controller. A commonly used stability criterion can be determined from the open-loop frequency response and is given by Franklin et al. [40]: the magnitude of the open-loop response should be less than unity when the phase crosses $-180°$; $|C(s)P(s)|_{180°} < 1$. For a system with a high Q-factor, this means that the crossover frequency cannot be chosen too high, since the high gain and the $-180°$ phase shift at the resonance frequency easily leads to instability.

In Section 5.4.1.2 and Section 5.4.1.4, we have seen that for increasing vacuum, the sensor response decreases. This means that the crossover frequency decreases and the response time of the closed-loop system increases. To keep a fast response time, the system should compensate for the decreasing sensor gain as a function of pressure. However, when a vacuum is applied, the Q-factor will increase. This can lead to instability for a system that was stable at ambient pressure. Two solutions are given to improve on the instability as a result of the decreasing pressure:

- add a low-pass filter (2nd order) to increase the phase delay of the open-loop transfer to less than $-180°$ before the resonance frequency, or
- add a notch filter to suppress the gain at the resonance frequency below 0 dB.

The integral controller is defined by the crossover frequency ω_c $(2\pi f_\mathrm{c})$ and the stiffness of the MEMS stage,

$$C_\mathrm{I}(s) = \frac{K_\mathrm{i}}{s} = \frac{\omega_\mathrm{c} k_0}{s}. \tag{5.13}$$

The low-pass filter $C_\mathrm{LP}(s)$ is designed with a cut-off frequency ω_LP of 5 times the crossover frequency ω_c and a relative damping ζ of 0.7,

$$C_\mathrm{LP}(s) = \frac{\omega_\mathrm{LP}^2}{s^2 + 2\zeta\omega_\mathrm{LP} s + \omega_\mathrm{LP}^2}. \tag{5.14}$$

A requirement for the use of a notch filter is that the eigenfrequency that must be suppressed is known. Typically the notch frequency is chosen slightly below the first eigenfrequency of the system. Since the resolution of our frequency measurement was limited to 10 Hz, we have chosen a notch frequency 5 Hz below the measured first eigenfrequency of 1310 Hz, $\omega_\mathrm{n} = 2\pi \cdot 1305\,\mathrm{Hz}$. A notch filter $C_\mathrm{N}(s)$ was designed with parameters $\xi_1 = 0.001$ and $\xi_2 = 0.1$,

$$C_\mathrm{N}(s) = \frac{s^2 + 2\xi_1\omega_\mathrm{n}s + \omega_\mathrm{n}^2}{s^2 + 2\xi_2\omega_\mathrm{n}s + \omega_\mathrm{n}^2}. \tag{5.15}$$

5.3 Experimental

The MEMS stage is integrated into the device layer of a silicon-on-insulator wafer (SOI-wafer) with a single-mask fabrication process. Aspect-ratio controlled deep reactive-ion etching (DRIE) was used to etch through the full device layer of the SOI-wafer of 25 µm. After the reactive-ion etching, the structures were released from the handle wafer by isotropic HF vapor phase etching of the 1 µm thick buried oxide layer. Thin structures (<10 µm) are released from the handle wafer in this way. Wide structures will stay mechanically fixed to the handle wafer, while being electrically isolated from the handle wafer due to the oxide layer. Stages and intermediate bodies that should be able to move are perforated to be released from the handle wafer. The fabricated devices are wire bonded with aluminum wires onto the gold-plated bondpads for measurements. An optical microscope image of the wire bonded MEMS device is given in Figure 5.4. All results in this work are from sensors with heater legs of 100 µm and a sensing part, the part of the heater parallel with the stage, of 150 µm. The heater width is 3 µm and the air gap between the heater and the stage is also 3 µm.

First the stage displacement as a function of the pressure was characterized using stroboscopic video microscopy by a Polytec MSA-400. For this purpose, the complete MEMS stage was placed in a vacuum chamber with a glass window for optical measurement of the stage position. A low-frequency (2 Hz) sine wave with an amplitude of 80 V was applied to the electrostatic actuator. A Texas Instruments OPA454 was used to amplify the generated setpoints to the required high actuation voltages, up to 100 V. The 1σ-noise on the position measurement was determined to be 64 nm over 1337 measurements. With this measurement setup, we verified that the actuator force is independent of the vacuum pressure (Section 5.4.1.1).

For the actuator setpoint generation, the Polytec MSA-400 was replaced by a MathWorks xPC Target platform with a National Instruments PCI-6221 analog I/O card. The thermal displacement sensor was connected in a measurement bridge setup, as shown in Figure 5.5. Resistive heating of the heaters was provided by the supply voltage U_s. When the stage position changes, the resistance of one of the heaters will increase and the resistance of the other will decrease (R_h1 and R_h2). This was measured in the voltage U_m. With a supply voltage of 12 V,

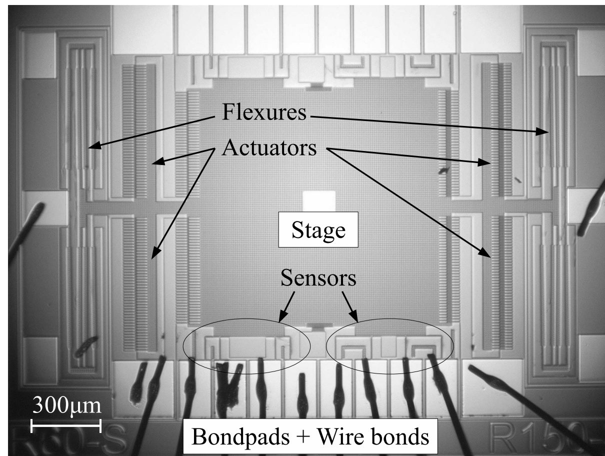

Figure 5.4: Top view optical microscope image of the complete system. The comb-drive actuators in combination with the flexures are able to enable stage displacements up to ±30 µm. Thermal displacement sensors are included for feedback of the stage position.

a sensitivity of 2.17 mV µm^{-1} was measured at ambient pressure. The sensor sensitivity is defined as the change in sensor voltage U_m between maximum and minimum displacement divided by the total displacement. The 1σ noise level of the thermal displacement sensor with electronics was 23 µV, and thus 11 nm, at a sample rate of 1 kHz. The voltage U_m was measured by an analog input of the National Instruments PCI-6221.

The Q-factor as a function of the vacuum pressure was measured using the built-in thermal displacement sensor. A step voltage was applied to the electrostatic actuator and the sensor voltage was measured in time. The Q-factor was obtained by curve fitting of the exponential decay of the oscillation of the MEMS stage. The sensitivity of the thermal displacement sensor decreases for lower pressures, which means that the signal-to-noise ratio of the Q-factor measurement decreases for lower pressures. The accuracy of the pressure meter, a Wöhler DC-17, is specified as ±0.3 mbar and 3% of reading. This means that the uncertainty in the Q-factor measurement increases to almost 17% at a pressure of 20 mbar.

This setup with a sample rate of 5 kHz was also used for the identification and control measurements in Section 5.4.1.4 and Section 5.4.2.

5.4 Results

In the first part of this section the vacuum behavior of the system is measured quasi-statically (Section 5.4.1.1 to 5.4.1.3). A frequency sweep is performed to determine the dynamic behavior in Section 5.4.1.4. The second part of this section

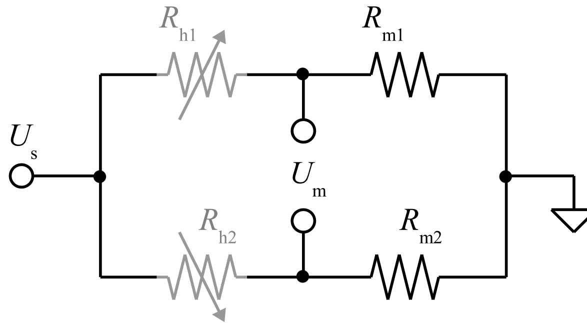

Figure 5.5: The thermal displacement sensor (R_{h1} and R_{h2}) was connected in a measurement bridge setup. The sensor is heated by the supply voltage U_{s}. When the stage position changes, the resistance of one of the heaters will increase and the resistance of the other will decrease. The differential resistance change is measured in the voltage U_{m}.

(Section 5.4.2) shows that we are able to control the position of the stage using the integrated sensor.

5.4.1 Vacuum behavior

The measurement results of the three subsystems of our MEMS stage are presented in the next sections: in Section 5.4.1.1, the electrostatic actuator; in Section 5.4.1.2, the thermal displacement sensor; and in Section 5.4.1.3, the damping of the flexure mechanism. The complete plant is identified in the frequency domain at four different vacuum pressures in Section 5.4.1.4.

5.4.1.1 Actuator

At ambient pressure, the stage was actuated with a voltage of 80 V. The resulting stage displacement had an amplitude A_0 of 21.9 µm. For vacuum pressures between 4.6 mbar and 1.0 bar, the amplitude of the stage displacement was measured optically. The stage response as a function of pressure is given relative to the response at ambient pressure in Figure 5.6.

The normalized amplitude values are all between 0.995 and 1.006, within the uncertainty band of the measurement noise. We conclude that there is no observable influence of the pressure on the relation between the stage displacement and the applied voltage.

5.4.1.2 Sensor

A low-frequency sinusoidal actuation voltage (2 Hz) was applied to the electrostatic actuator. The amplitude of the sensor response U_{m} was measured for vacuum pres-

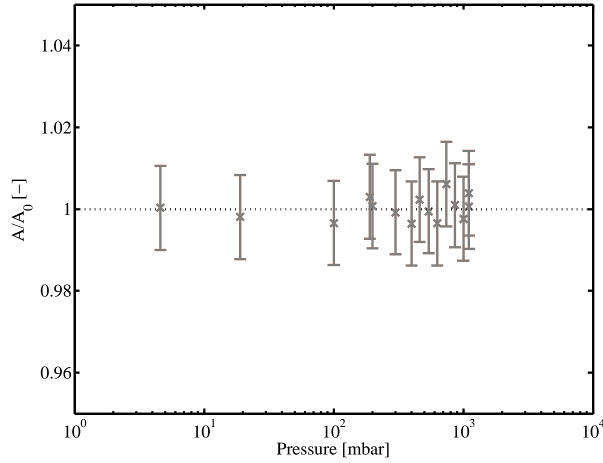

Figure 5.6: The actuator response of the stage as a function of the pressure relative to the actuator response at ambient pressure (A_0). There is no observable influence of pressure on the actuated stage displacement. The error bars indicate the 3σ uncertainty.

sures between 5.0 mbar and 9.9×10^2 mbar. The sensor output is shown relative to the sensor response at ambient pressure, 2.17 mV µm^{-1}, in Figure 5.7.

The sensor response is independent of the pressure within the range of 800 mbar to 10 bar. Below 20 mbar, the response drops by approximately 20 dB per decade of pressure, reaching the detection limit at 1 mbar. The sensor response can be accurately modeled with an accommodation coefficient α_{T} of 0.8 for pressures above 10 mbar.

5.4.1.3 Mechanism

The Q-factor of the resonating stage was measured and the results are given in Figure 5.8. The quality factor of the actuator in resonance decreases with increasing pressure. The behavior can be modeled assuming viscous damping with a momentum coefficient α_{M} of 0.8 for pressures above 50 mbar.

5.4.1.4 System

A frequency sweep from 5 Hz to 2500 Hz was performed on the MEMS stage. A sinusoidal input force was used as a setpoint and the sensor output was measured. The measurements were converted into the transfer function from the input force to the output position. The results for four different pressures, 30 mbar, 70 mbar, 130 mbar, and at an ambient pressure of 980 mbar, are given in Figure 5.9. The sensor gain used for the frequency sweep was determined at ambient pressure at low frequency to be 4.6×10^{-4} m V^{-1}.

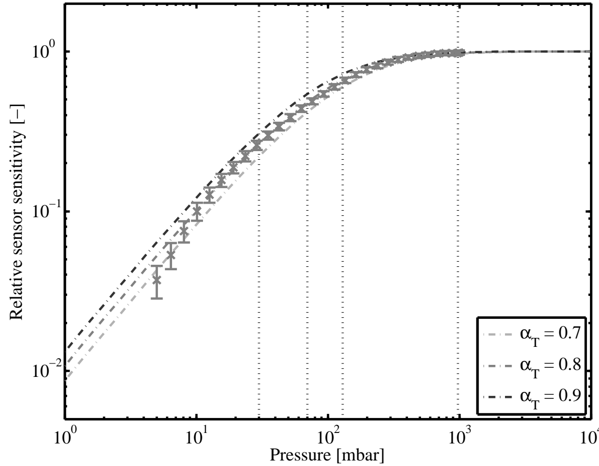

Figure 5.7: Sensor sensitivity, relative to the sensitivity at 1 bar, as a function of pressure, compared to a model with accommodation coefficient α_{T} ranging from 0.9 (top) down to 0.7 (bottom). The sensor response drops for pressures below 800 mbar and can be accurately modeled for pressures above 10 mbar with an accommodation coefficient of 0.8.

From the measurements we can see that below 500 Hz the MEMS stage does not show any frequency dependent behavior: the MEMS stage acts purely as a stiffness. The magnitude corresponds with the inverse of the stiffness of the MEMS stage, $0.28\,\mathrm{m\,N^{-1}}$, multiplied by the normalized sensitivity of the sensor. In this frequency range, we can clearly see the decreasing sensor response as a function of the vacuum pressure. The sensor response is also given in Table 5.1. The average sensitivity of the data points below 500 Hz is taken. The sensor sensitivity from this frequency sweep matches within 8 % the quasi-static measurements and the modeled values (Section 5.4.1.2).

Table 5.1: The table lists the normalized sensor sensitivity from the frequency sweep, the quasi-static characterization, and the model. Normalization is performed relative to the sensitivity at ambient pressure.

Vacuum pressure	**Sensor sensitivity**		
	Model	Quasi-static	Sweep
30 mbar	0.27	0.27	0.25
70 mbar	0.49	0.47	0.47
130 mbar	0.67	0.66	0.65
980 mbar (ambient)	1.0	1.0	1.0

The first resonant frequency of our MEMS stage is found at 1310 Hz. From

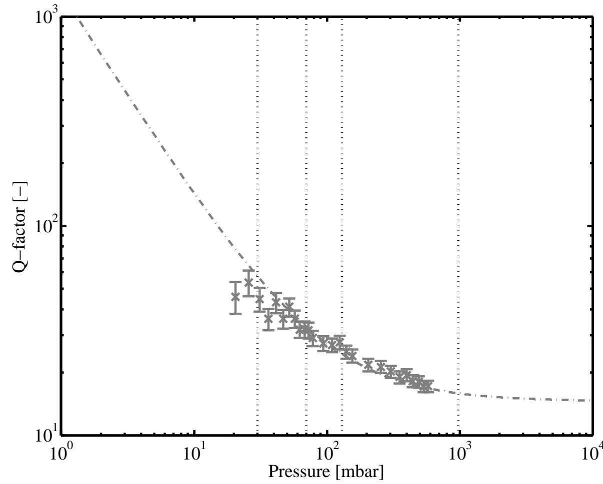

Figure 5.8: Quality factor of resonance as a function of pressure, compared with a model assuming viscous damping. The Q-factor increases for decreasing pressure and can be modeled with an α_{M} of 0.8 for pressures above 50 mbar.

our design, we would expect an eigenfrequency of 1186 Hz. We have seen before that fairly large deviations exist in the eigenfrequency of MEMS devices [69]. From the frequency sweep measurement data, we can obtain the Q-factor based on the width of the peak at the first eigenfrequency: $Q = \omega_0/\Delta\omega_{-3\,\mathrm{dB}}$. Using this method, we have determined the Q-factors of the plant from the frequency sweep data in Figure 5.9, the results are listed in Table 5.2. The values from the frequency sweep measurement are compared with the values from Section 5.4.1.3 and show agreement within 6 % for the values above 50 mbar.

Table 5.2: The Q-factor obtained from the ringdown data and the Q-factor estimated from the plant identification.

Vacuum pressure	**Q-factor**		
	Model	Quasi-static	Sweep
30 mbar	58	44	52
70 mbar	33	32	31
130 mbar	24	25	24
980 mbar (ambient)	16	16	15

The theoretical frequency response of the plant mechanics $M(s)$ at ambient pressure is given by the dashed line in Figure 5.9. We can clearly see that for frequencies over 500 Hz the measured magnitude is lower than the theoretical magnitude. This is most probably caused by the frequency response of our thermal

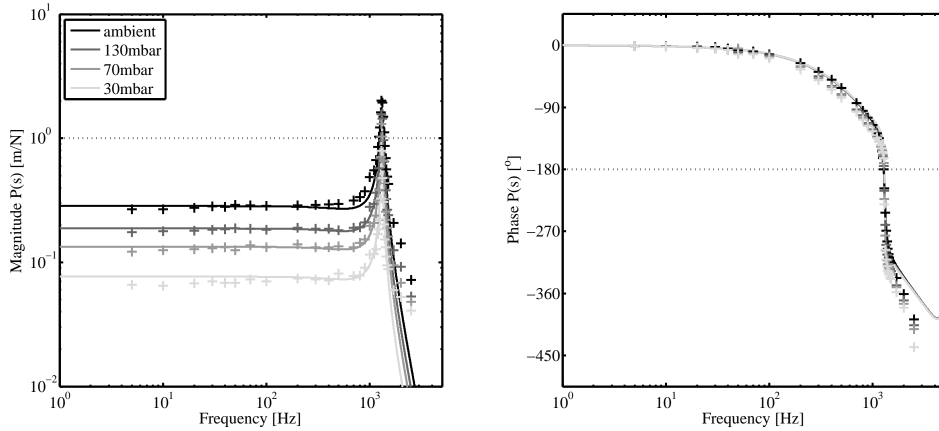

Figure 5.9: The frequency response of the plant $P(s)$ including the response of the sensor is determined at various vacuum pressures. The left image shows the magnitude $x_{\mathrm{ms}}/F_{\mathrm{act}}$, the right image shows the phase delay $\phi(x_{\mathrm{ms}}) - \phi(F_{\mathrm{act}})$. The measurements are indicated by the markers, the models are given by the solid lines. The frequency response excluding the sensor response at ambient pressure is given by the dashed line.

displacement sensor. A second order low-pass filter with a cut-off frequency ω_{LP} of 1060 Hz (150 µs) is used to describe the frequency behavior of the thermal sensor. This results in a much better agreement between the model and the measured magnitude of the frequency response. The second order model was particularly chosen to match the phase shift of the plant model with the measurements.

From this section we conclude that the MEMS stage can be described in the frequency domain by a mass–spring–damper system and a second order low-pass filter for the thermal response of the sensor.

5.4.2 Control

This section shows the measurement results of the MEMS stage with the integral controller with and without the additional filters: the integral controller (C_{I}), the integral controller with low-pass filter ($C_{\mathrm{I+LP}}$), and the integral controller with notch filter ($C_{\mathrm{I+N}}$). First the expected frequency and time response of the controllers is validated by measurements at a crossover frequency of 50 Hz at ambient pressure. Then the models are used to identify the limits regarding crossover frequency and settling time for ambient pressure as well as a vacuum pressure of 1 mbar, which was the detection limit of our thermal displacement sensor.

Figure 5.10 shows the open-loop transfer functions of the MEMS stage at ambient pressure with an integral controller, with an additional second order low-pass filter, and with an additional notch filter. The magnitude plot (left) shows that the crossover frequency of the controllers is indeed 50 Hz. The resonance peak

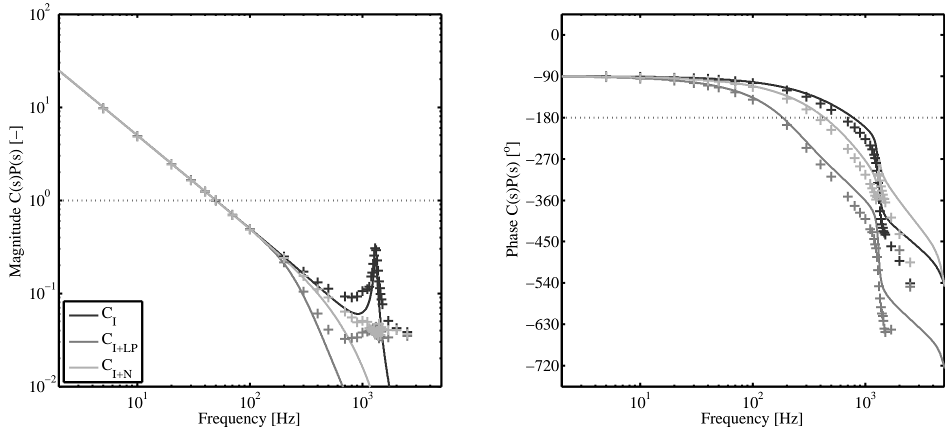

Figure 5.10: The open-loop transfer functions of the plant at ambient pressure with an I-controller (C_{I}), an additional low-pass filter ($C_{\mathrm{I+LP}}$), and an additional notch filter ($C_{\mathrm{I+N}}$) are shown. The left side of the figure gives the magnitude x_{ms}/e, the right side shows the phase delay between input and output. The controllers were set to a crossover frequency of 50 Hz. Measurements are indicated by markers, the physical model is given by the solid lines.

at the first eigenfrequency is clearly visible for the controller without filter. Our sensor signal-to-noise ratio was not sufficient to measure magnitudes smaller than 3×10^{-2} ($-30\,\mathrm{dB}$), which explains the flattening off at that value. The resonance peaks for the controllers with low-pass and notch filter are suppressed below the sensor detection limit. The phase response of the open-loop system is given in Figure 5.10 on the right. The controller with low-pass filter increases the phase delay of the open-loop system. A phase delay of -180° is reached well before the resonance frequency. Overall, the measurements show that the controllers behave as expected and their behavior can be modeled accurately.

By enabling the feedback signal, we can look at the closed-loop time response of the system at a crossover frequency of 50 Hz. The results are given in Figure 5.11. The settling time is defined as the time it takes for the closed-loop system to settle in a specified error band, in this case we have chosen 1%. The left plot shows the advantage of the low-pass and the notch filter: the reduced actuation magnitude at the resonance frequency results in shorter settling times. The right side of Figure 5.11 shows the response of the closed-loop system as a result of a disturbance step in the actuation force, given by F_{d} in Figure 5.3. For the chosen controllers, the resulting position signal shows very little damping at the first eigenfrequency of the MEMS stage. Since the eigenfrequency is above the crossover frequency of the controller, no damping is added by the controllers at this frequency. This disturbance does not lead to instability. From Figure 5.11 (left), the settling times are retrieved and listed in Table 5.3. For a crossover

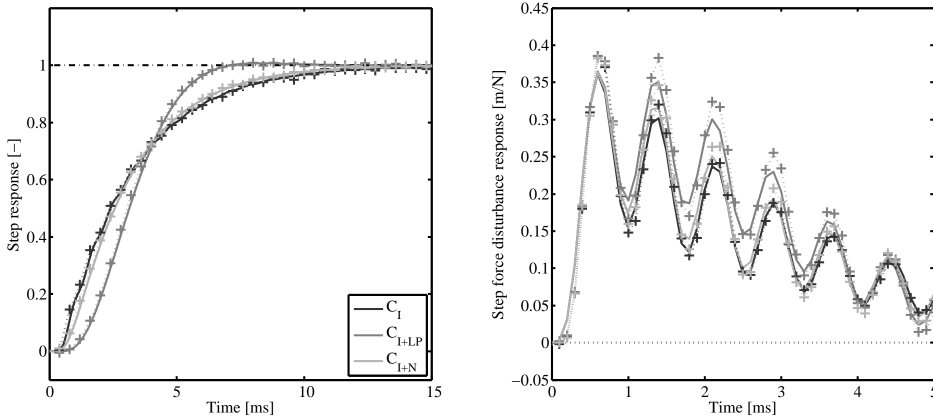

Figure 5.11: The time response of the closed-loop system with C_I, the additional low-pass filter ($C_\mathrm{I+LP}$), and the additional notch filter ($C_\mathrm{I+N}$) is shown. The step response (left) shows the measured position relative to the setpoint position, $x_\mathrm{ms}/x_\mathrm{sp}$, for a step on the setpoint position. The step force disturbance response (right) shows the measured position relative to a step force disturbance, $x_\mathrm{ms}/F_\mathrm{d}$, with $x_\mathrm{sp} = 0$. In both cases, the controllers were set to a crossover frequency of 50 Hz.

frequency of 50 Hz the controller with low-pass filter gives the shortest settling time. Furthermore, the modeled settling times deviate less than 8% from the measured settling times.

Table 5.3: The modeled and measured 1% settling times of the closed-loop system with and without additional filters and a crossover frequency of 50 Hz.

Controller	**Settling time**	
	Model	Measurement
C_I	13.2 ms	13.9 ms
$C_\mathrm{I+LP}$	6.2 ms	6.7 ms
$C_\mathrm{I+N}$	12.0 ms	12.6 ms

The measurements of the open-loop frequency response and the time responses show good agreement with the modeled values. Therefore we will use these models to identify the limits of the system for ambient pressure as well as for a vacuum pressure of 1 mbar. For ambient pressure, a Q-factor of 16, and at 1 mbar, a Q-factor of 1305, the minimum settling time of the controllers was determined. The relative sensor sensitivity of 0.01 at 1 mbar was compensated for by increasing the sensor gain. The minimum settling times for the closed-loop system with the three different controllers are listed in Table 5.4.

At ambient pressure, the settling time decreases by a factor of 4.5 for the con-

Table 5.4: The minimum settling time for the different controllers is determined.

Controller	Minimum settling time (crossover frequency)	
	1.0 bar	1.0 mbar
C_{I}	10.5 ms (77 Hz)	> 100 ms (2 Hz)
$C_{\mathrm{I+LP}}$	2.3 ms (144 Hz)	4.5 ms (114 Hz)
$C_{\mathrm{I+N}}$	2.2 ms (162 Hz)	2.2 ms (163 Hz)

trollers with additional filter in comparison to the integral controller without filter, Table 5.4. Even larger differences are observed at a pressure of 1 mbar. The integral controller without filter becomes unstable at a crossover frequency above 2 Hz. At this crossover frequency, the settling time is over 100 ms. This clearly shows the need of the additional low-pass or notch filter. The maximum crossover frequency of the integral controller with low-pass filter and with notch filter also decreases for a pressure of 1 mbar, but not as dramatically as the crossover frequency of the integral controller without filter. The settling time of the controller with notch filter is slightly lower than the settling time for the controller with low-pass filter, for ambient pressure as well as for 1 mbar.

Both the integral controller with low-pass filter and notch filter increase the maximum crossover frequency of the controlled stage at low pressure in such a way that short settling times can still be achieved. The controller with the notch filter achieves a higher crossover frequency and therefore a lower settling time than the controller with low-pass filter. This makes the controller with notch filter the preferred controller.

5.5 Discussion

A thin film of water might form on the surface of our devices [104], which is expected to evaporate in a vacuum. Since the reported water film thickness is limited to roughly 1 nm, this is too small (0.03 %) to have an observable influence on the actuation force in (5.1) and the actuation amplitude in Figure 5.6.

Although the accuracy of the pressure meter drops for lower pressure, this does not fully explain the deviations between the simulation and the measurements in Figure 5.7 and Figure 5.8. The model given in [73] to describe the sensor sensitivity was validated by various measurements to be accurate within 10 % at ambient pressure. Deviations were explained by mismatches in the electrical resistivity of silicon, the thermal conductivity of silicon, the thermal conductivity of air (all as functions of the temperature) and boundary effects that might not have been adequately taken into account. So the deviation between the simulation and the measurements in Figure 5.7 is not only caused by the increasing uncertainty on the measurements, which is indicated by the error bars, it is also caused by an increasing uncertainty of the model. The same holds for the simplified model that

describes the Q-factor of the MEMS stage. The measurements show a lower Q-factor than the model, which means that additional damping sources exist in the system. For instance, squeeze-film and material damping have not been taken into account. Measurement errors are indicated in Figure 5.8 by the error bars, the model uncertainty is not.

Variations in leafspring thickness have a large influence on the eigenfrequency of the MEMS stage. For example, a leafspring thickness of 3.2 µm instead of 3.0 µm already leads to the measured increase in eigenfrequency from 1186 Hz to 1310 Hz. This is well within the range of values we observed with a similar fabrication process [38]. Fabrication inaccuracies most probably cause the variations in leafspring thickness. Various sources can be distinguished: mask errors, resist etching, and tapering during deep reactive-ion etching [58].

In the design of our controllers, we have seen that their response is slightly affected by discretization. Although working with a sample rate of 5 kHz, the magnitude and phase response of the controller and filters already showed observable deviations for frequencies over 1 kHz. All simulation results, in tables and in graphs, are compensated for the effect of discretization.

5.6 Conclusions

In this paper we proposed an electrostatically actuated MEMS stage with integrated thermal position sensor. The MEMS stage can be described in the frequency domain by a mass–spring–damper system and a second order low-pass filter for the response of the thermal sensor. Models have been developed that quantitatively describe the decreasing thermal conductivity and viscosity of air as a function of pressure. The sensor response can be accurately modeled for pressures above 10 mbar, and that of the Q-factor of the stage, for pressures above 50 mbar.

The maximum crossover frequency for our MEMS stage with only an integral controller decreases rapidly in a vacuum environment, which resulted in a settling time of over 100 ms. An additional low-pass or notch filter also shows a decrease in maximum crossover frequency for a vacuum environment. However the settling times at 1 mbar, 4.5 ms and 2.2 ms, respectively, are still good. Due to its lower settling time, the integral controller with notch filter and a crossover frequency of 163 Hz is the preferred controller.

Generally, we showed that electrostatically actuated microstages with thermal displacement sensors for position control can be used in vacuum environments down to 1 mbar. This enables applications in eSEMs, for example. Although the models were only validated for a single set of characteristic dimensions, the models are suited for a much broader range of parameters.

Chapter 6

A large-stroke 3DOF stage with integrated feedback in MEMS

In this work we design, fabricate, and validate a large-stroke 3DOF positioning stage with integrated displacement sensors for feedback control in a single-mask MEMS fabrication process. Three equal shuttles exactly define the position of the stage in x, y, and R_z. The kinematic relation between the shuttle positions and the stage position is given by the geometric transfer function. By increasing the order of this geometric transfer function the stage error can be reduced. Each shuttle consists of a flexure mechanism, a position sensor and electrostatic comb drive actuators for actuation along a straight line. The range of motion of the stage is limited by electrostatic pull-in of these comb drives. Three parameters of the stage, the leafspring length, the eccentricity, and the tangential arm, have been varied to find their influence on the stage range of motion. These simulation results can be used to design stages with different specifications. Position control of the individual shuttles is applied to control the position of the stage. The stroke of the 3DOF stage is verified up to 161 µm in x, 175 µm in y, and 325 mrad in R_z. This exceeds the range of motion of existing stages.

This chapter will be submitted as 'B. Krijnen, K.R. Swinkels, D.M. Brouwer, L. Abelmann, and J.L. Herder. A large-stroke 3dof stage with integrated feedback in mems. *Journal of Microelectromechanical Systems*, 2014 (to be submitted)'.

6.1 Introduction

Positioning stages in MEMS can be used in a variety of applications, such as probe based data storage systems [36], integrated optical components [97], and sample positioners or manipulators in electron microscopes [25, 94, 133]. Since friction effects have a large influence on the micro scale, typical existing multi degree-of-freedom (DOF) positioning stages in MEMS are based on compliant flexure mechanisms. The lack of friction and backlash also has large advantages with respect to positioning repeatability and wear [120]. An additional advantage is that they can be produced using a single mask.

In literature more multi-DOF stages are found. For example De Jong et al. [28] and Mukhopadhyay et al. [91] show very similar parallel kinematic 3DOF stages with a stroke of 20 µm and 27 µm and a rotation of 70 mrad and 30 mrad, respectively. A six-axis compliant mechanism is presented by Chen and Culpepper [17]. It consists of three pairs of two-axis thermomechanical actuators. The device is capable of moving over a range of 13 µm and 33 mrad. A very compact electrostatic stepper platform is presented by Sarajlic et al. [113] which is capable of 2-DOF movements of 60 µm. These stages do not include position sensing. Several positioning stages with integrated feedback are reported in literature [22, 79, 108]. These stages however require complicated fabrication schemes and assembly or offer relative small stroke. Especially the integration of the complete system without assembly can have major benefits with respect to cost and performance. In this work we present the design, optimization, and validation of a large stroke 3DOF positioning stage with integrated displacement sensors for feedback control in a simple, single-mask fabrication process. A fabrication process based on a silicon-on-insulator (SOI) wafer in combination with directional deep reactive-ion etching (DRIE) is used.

For actuation, typically thermal or electrostatic comb-drive actuators are used. Thermal actuators generally suffer from long term drift due to constant power dissipation and are relatively slow [23, 47, 102]. Electrostatic comb-drive actuators in combination with flexure mechanisms can reach large strokes and only consume power when moving [124]. Since the electric field yields a negative lateral stiffness, electrostatic actuators can suffer from instability if the positive mechanical stiffness of the flexure mechanism or the individual comb fingers is not sufficient. For large deflections, and thus high voltages, the result is pull-in [80]. To prevent pull-in, the flexure mechanism should be compliant in actuation direction and stiff in lateral direction. In previous work we have studied several flexure mechanisms and concluded that the tilted folded flexure is the optimal flexure mechanism for the strokes we are aiming at, between ± 50 µm and ± 100 µm [69].

The chosen position sensor consists of two heaters. The heaters are placed in differential configuration next to each shuttle. A heater consists of a thin plate that is electrically heated. Because the nearby shuttle functions as a heat sink, the amount of overlap determines the temperature of the heater by conduction trough air. As the resistivity of silicon depends on its temperature, the amount of shuttle

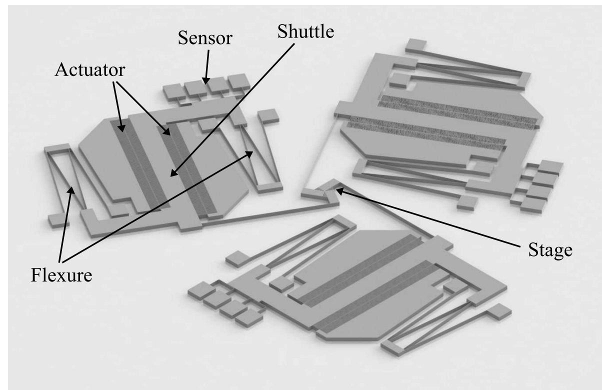

Figure 6.1: Rendered image of the stage connected to three equal single-DOF shuttles. Each shuttle is suspended by a flexure to constrain its movement to a line. The shuttle is actuated by electrostatic comb-drives and the shuttle position is measured by thermal displacement sensors.

overlap determines the heater resistance, which can be measured. The resulting sensor is used for position feedback [73].

To realize the three degrees of freedom, a serial or parallel mechanism can be used. Because routing of the electrical connections to the actuators and sensors is generally difficult in MEMS, a parallel kinematic configuration is chosen. An overview of the system is shown in Figure 6.1. It consists of three straight guided shuttles that are eccentrically connected to a stage. This way the translations x and y and the rotation R_{z} of the stage are exactly defined by the position of the three shuttles. Each shuttle consists of a flexure mechanism, a position sensor and two electrostatic comb drive actuators for actuation along a straight line.

Section 6.2 of this paper will provide theory with respect to the kinematic coupling between the shuttles and the stage (section 6.2.1), calculations on the range of motion of the 3DOF stage (section 6.2.2), optimization of the range of motion with respect to several design parameters (section 6.2.3), and the chosen strategy for position control of the stage (section 6.2.4). In section 6.3 details on the measurement setup and the fabricated devices is given. Afterwards in section 6.4 the measurement results are presented, which consist of the frequency domain identification (section 6.4.1), the closed-loop response of the system (section 6.4.2), and the measured stroke (section 6.4.3). This section will also provide a comparison of the measured stroke of our device with respect to existing stages found in literature.

6.2 Theory

In order to position the 3DOF stage, the kinematic coupling between the shuttles and the stage is required, this is given in section 6.2.1. This method can be used to reduce errors on the stage position and rotation by means of calibration. The stroke of the stage is limited by electrostatic pull-in and is calculated in section 6.2.2. The influence of the stage leafspring length, the eccentricity of the stage, and the tangential arm is studied. The simulation results are presented in section 6.2.3. The chosen strategy for control of the stage is given in section 6.2.4.

6.2.1 Geometry

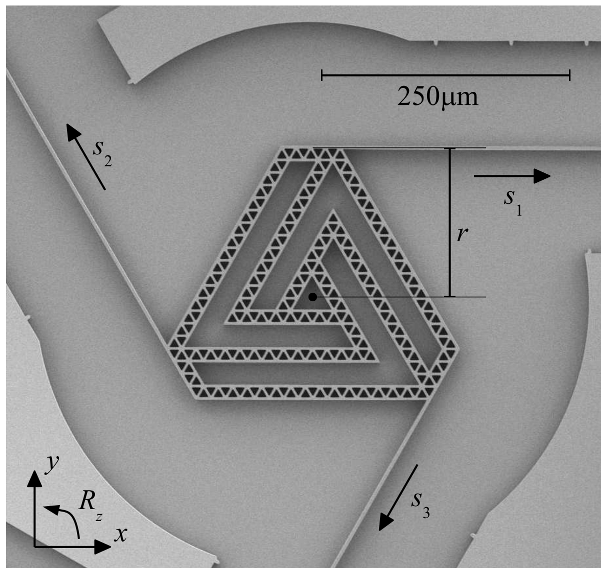

Figure 6.2: A scanning electron microscope image of one of the fabricated stages. Three equal shuttles are eccentrically connected to the stage with eccentricity r. The position of the three shuttles s_1, s_2, and s_3 uniquely defines the position in x and y and the rotation R_z of the stage.

Three equal shuttles are eccentrically connected to the stage with eccentricity r, as shown in Figure 6.2. The three shuttle positions s_1, s_2, and s_3 exactly define the position of the stage in x, y, and R_z. The matrix that defines the relation between the shuttle positions and the stage position is called the geometric transfer function GTF. The simplest GTF has order one (GTF_1) and is a linear relation between the shuttle positions and the stage position; a matrix of size 3x3. Analytically this

first order GTF in the neutral position is given in [28],

$$\begin{bmatrix} s_1 \\ s_2 \\ s_3 \end{bmatrix} = \mathrm{GTF}_{1\mathrm{A}} \begin{bmatrix} x \\ y \\ R_\mathrm{z} \end{bmatrix} \tag{6.1a}$$

$$\mathrm{GTF}_{1\mathrm{A}} = \begin{bmatrix} 1 & 0 & -r \\ -\frac{1}{2} & \frac{1}{2}\sqrt{3} & -r \\ -\frac{1}{2} & -\frac{1}{2}\sqrt{3} & -r \end{bmatrix}. \tag{6.1b}$$

For large deflections the stage position will no longer behave linear as a function of the shuttle positions. To model these non-linear effects, a multibody model of the complete system is made in SPACAR [62]. SPACAR is used to numerically determine the higher order GTFs and the resulting stage position error as a function of the shuttle positions. We have chosen to use SPACAR, since it is a relatively fast program that is capable of spatial mechanics simulations. The shuttles and stage are modelled as rigid elements, the tilted folded flexures and the leafsprings towards the stage are modelled by flexible beam elements. We have used the anisotropic Young's modulus of silicon in our simulations [50].

In SPACAR a wide range of forces was applied to the three shuttles. The resulting stage displacements had a more or less uniform distribution in the $x - y - R_\mathrm{z}$ space. Least square curve fitting was used for determination of the numerical GTFs (GTF_N) up to the order four (and its inverses). We have used the Matlab function *mldivide()* for this. For example, the second order numerical GTF has a matrix size of 3x9 and provides the shuttle positions as a function of the stage position and its second order terms,

$$\begin{bmatrix} s_1 \\ s_2 \\ s_3 \end{bmatrix} = \mathrm{GTF}_{2\mathrm{N}} \begin{bmatrix} x \\ y \\ R_\mathrm{z} \\ x^2 \\ y^2 \\ R_\mathrm{z}^2 \\ xy \\ xR_\mathrm{z} \\ yR_\mathrm{z} \end{bmatrix}. \tag{6.2}$$

The error between the actual stage position and the calculated stage position using the inverse GTF is determined,

$$\begin{bmatrix} e_\mathrm{x} \\ e_\mathrm{y} \\ e_\mathrm{Rz} \end{bmatrix} = \begin{bmatrix} x_\mathrm{actual} \\ y_\mathrm{actual} \\ R_\mathrm{z,actual} \end{bmatrix} - \mathrm{GTF}^{-1} \begin{bmatrix} s_1 \\ s_2 \\ s_3 \end{bmatrix}. \tag{6.3}$$

The results are listed in Table 6.1.

By choosing a GTF of order 4 instead of 1 we can decrease the stage error in x and y by a factor of 140 and the stage error for the rotation R_z by a factor of 80. To

Table 6.1: The stage position error as a function of the fit order, calculated according to (6.3).

Maximum displacement			N^{th} order fit error			
			N = 1	N = 2	N = 3	N = 4
x	139 µm	e_x	6.15 µm	667 nm	139 nm	42.8 nm
y	126 µm	e_y	6.54 µm	629 nm	107 nm	33.0 nm
R_z	456 mrad	e_{Rz}	105 mrad	23.3 mrad	2.63 mrad	1.26 mrad

reach a resolution below 100 nm, we require a GTF of order four. Fairly large tolerances are observed in a similar fabrication process [38], therefore we expect that the higher-order numerical GTFs from SPACAR will still give positioning errors in the actual devices. Since the complete system is a well-constrained flexure-based design, we expect the device to act repeatable. By determination of the (higher-order) GTFs of the actual devices we expect to be able to decrease the stage position errors in a similar way.

6.2.2 Electrostatic pull-in and range of motion

The major problem that limits the displacement of electrostatically actuated stages is pull-in. This effect can play a role in individual fingers and in entire flexure mechanisms. Both cases are often destructive to the device and need to be avoided.

To reach a stroke of ±100 µm, comb-drive fingers with a length of approximately 120 µm are required. Elata and Leus [35] have derived an analytical expression for the minimum thickness of the comb-drive fingers as a function of the applied voltage. We can rewrite this expression to determine the limit point voltage V_{lp} for a given comb-drive finger,

$$V_{\text{lp}} = \sqrt{\frac{Et^6\hat{V}_{\text{PI}}^2}{24\epsilon_0 l^4}}. \tag{6.4}$$

In this equation E is the Young's modulus of silicon, which has a minimum value of 130 GPa [50], ϵ_0 is the vacuum permittivity of $8.85 \times 10^{-12}\,\text{F}\,\text{m}^{-1}$, and $\hat{V}_{\text{PI}}$ is the normalized pull-in voltage of 3.516 [35]. For comb fingers with a length l of 120 µm and a thickness t of 3 µm the maximum voltage to be applied is 164 V. Meijaard et al. [89] show that for misaligned fingers due to quasi straight-line flexures the limit point voltage decreases with 22 % for lateral deflections up to 200 nm. The number of fingers in the comb-drives is chosen such that the required actuation voltage is always below a safe value of 80 V.

Flexure pull-in occurs when the lateral mechanical stiffness of the complete flexure mechanism is insufficient to withstand the negative 'electrostatic stiffness' as a result of the electric field. For stability, an equilibrium should exist in the lateral direction of the flexure mechanism. This equilibrium is given for every

displacement in actuation direction x in [69],

$$\frac{1}{2}N\epsilon_0\epsilon_\mathrm{r}h(x_0+x)U_\mathrm{req}^2\left(\frac{1}{(g-y)^2}-\frac{1}{(g+y)^2}\right) - K_{y,\mathrm{m}}(y-y_\mathrm{m})=0. \quad (6.5)$$

In this equation N is the number of comb finger pairs, ϵ_r is the relative permittivity of air (1), h is the height of the structures and thus the thickness of the device layer (25 µm), x_0 is the initial comb finger overlap (10 µm), U_req is the required voltage to reach the displacement x, g is the initial air gap between the comb fingers (3 µm), and $K_{y,\mathrm{m}}$ is the lateral stiffness of the flexure mechanism. The solution of this fifth order polynomial is the lateral displacement y of the shuttle, which is the result of the parasitic shuttle displacement y_m and the lateral electrostatic force. The variables x, y_m, and $K_{y,\mathrm{m}}$ are derived using the SPACAR model that was described before. Forces in actuation direction are applied to the three shuttles. The outcome of SPACAR (x, y_m, and $K_{y,\mathrm{m}}$) can subsequently be used to calculate the solution to (6.5) for each shuttle. If such a solution exists, this means that no pull-in occurs for that shuttle.

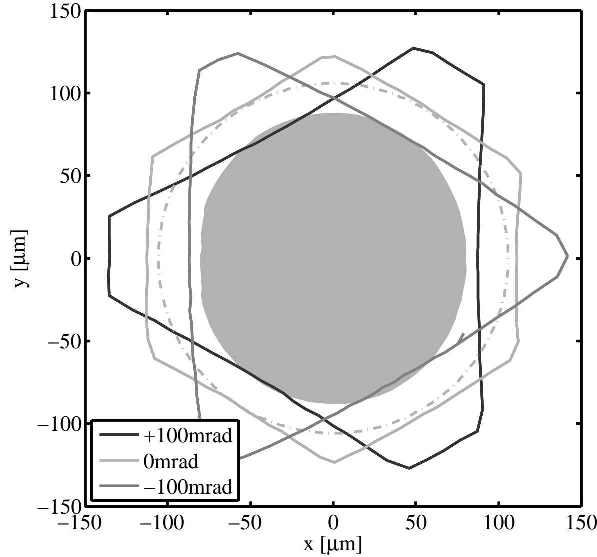

Figure 6.3: The range of motion of the 3DOF stage is given for three rotations; zero rotation and +/-100 mrad. The dash-dotted circle is the largest circle that fits in the hexagon at zero rotation, the radius of this circle is called the stroke (106 µm). The filled area shows the positions that are reached experimentally at zero rotation.

For a large number of shuttle forces the moment that pull-in occurred was calculated by steadily increasing the shuttle forces. In the space $x-y-R_\mathrm{z}$ this

results in a closed 3D surface. A cross-section was made of this surface at three rotations, +100 mrad, zero rotation, and -100 mrad. The resulting range of motion of the stage is plotted in Figure 6.3. We have used shuttles suspended by tilted folded flexures for these simulations. The flexure leafsprings had a thickness of 3 µm and a length of 1000 µm. The leafsprings were tilted over an angle of 85°. At zero rotation the range of motion of the 3DOF stage is roughly limited by a hexagon with six equal sides, representing pull-in in push- and in pull-direction of the three shuttles. The given circle is the largest circle that fits in the hexagon at zero rotation, the radius of this circle is called the stroke. At 0 mrad the stroke of the 3DOF stage is 106 µm. When a combined translation and rotation are required, the stroke decreases. For a rotation of +100 mrad the stroke is 84 µm and for a rotation of −100 mrad the stroke is 83 µm.

6.2.3 Optimization

The SPACAR model was used to vary several geometric parameters that couple the shuttles and the stage. The influence on the stroke and rotation of the stage is studied. The geometric parameters that were varied are the stage eccentricity r, the stage leafspring length l_{sl}, and the tangential arm t. These parameters are graphically shown in Figure 6.4. The stage leafspring length is the length of the leafsprings that connect the shuttles with the stage. The eccentricity is the radius or radial arm of the stage. The tangential arm is the distance between the radial arm and the joint of the stage leafspring and the stage. This distance is defined positive if the stage leafspring attaches before the center of the stage.

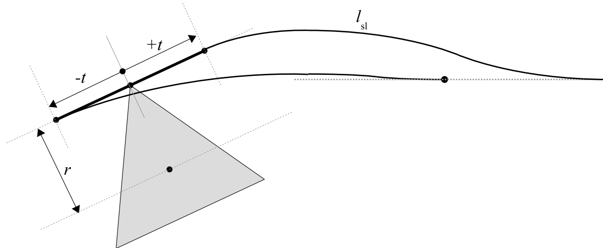

Figure 6.4: The three geometric parameters that were varied in the optimization run; the stage eccentricity r, the stage leafspring length l_{sl}, and the tangential arm t. The bending of the stage leafspring is shown for positive and negative tangential arm, $+t$ and $-t$ respectively. For positive t an equal rotation of the stage requires more bending of the stage leafspring. Therefore the actuator force needs to be higher and this causes pull-in at a smaller stroke.

The results of the optimization run are shown in Figure 6.5. The basic observation is that when a rotation is combined with a translation, the stroke of the 3DOF stage reduces. This we have seen before in section 6.2.2. Furthermore,

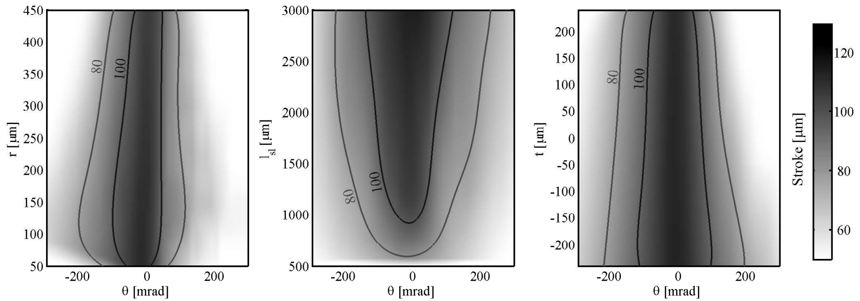

Figure 6.5: The stroke of the stage as a function of the stage eccentricity r (left), the stage leafspring length l_{sl} (center), and the tangential arm t (right). The colormap gives the stroke in micrometer. An optimum in the stage eccentricity is found at 175 µm. Longer stage leafsprings and a larger negative tangential arm result in a larger stroke of the 3DOF stage.

the optimization is mainly used to gain insight in the functioning of the parallel kinematic stage, so only qualitative conclusions are drawn:

- Eccentricity (left): An increase in eccentricity means that a shuttle move results in less rotation of the stage, a decrease in eccentricity results in a higher rotational stiffness. Therefore, an optimum for the stroke as a function of the stage eccentricity exists and is found at 175 µm.
- Stage leafspring length (center): An increase in stage leafspring length results in a larger stroke due to a lower stiffness. The lower stiffness and resonance frequency can become undesired, especially in out-of-plane direction.
- Tangential arm (right): By letting the stage leafsprings connect to the stage beyond the radial arm and thus with negative t, the stroke of the stage increases. This is caused by the energy that is required to bend the stage leafsprings. For a negative tangential arm, the stage leafspring requires less bending than for a positive tangential arm, schematically shown in Figure 6.4.

6.2.4 Feedback control

To apply stable position control of the 3DOF stage, the dynamic behavior of the system is important. Since the complete system is flexure-based, for low frequencies the stage is a stiffness in x, y and R_{z}. The resonance frequencies and corresponding mode shapes are determined from SPACAR. The in-plane mode shapes in x and y direction give the lowest resonance frequencies of 472 Hz. These modes correspond to a pure translation of the stage over the x-axis and the y-axis, respectively. The third resonance frequency is found at 1075 Hz. This mode is a pure rotation in R_{z} of the stage as a result of an equal translation of each shuttle.

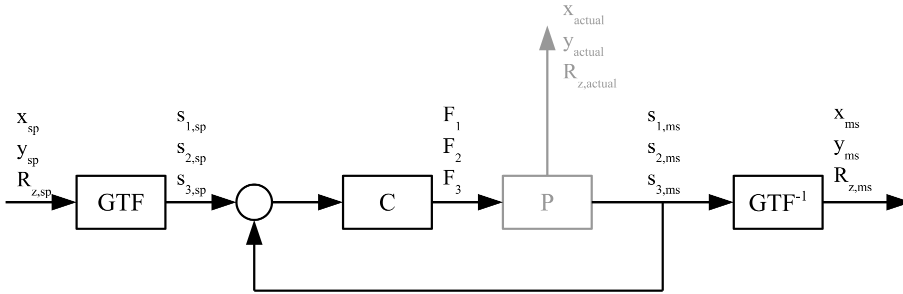

Figure 6.6: A diagram of the MEMS stage, the controller, the GTF, and its inverse (GTF^{-1}). Different positions are defined in this diagram: the setpoint positions are labeled with the subscript 'sp', the measured positions are labeled with the subscript 'ms', and the positions measured with an optical microscope for calibration are labeled 'actual'. The 'actual' position is considered to be the real position of the stage.

The dominant stiffnesses and the corresponding resonance frequencies are given in Table 6.2.

Table 6.2: The dominant dynamics of the MEMS stage from SPACAR.

Mode	Stiffness	Resonance frequency
x	$0.601\,\mathrm{N\,m^{-1}}$	472 Hz
y	$0.601\,\mathrm{N\,m^{-1}}$	472 Hz
R_z	$1.39 \times 10^{-7}\,\mathrm{N\,m\,rad^{-1}}$	1075 Hz

Since we are only interested in actuation far below the first resonance frequencies of the shuttles, the system can be simplified to a stiffness in x, y and R_z. The simplest way to control a system that behaves as a stiffness is by using an integral controller. The transfer function of the integral controller C_I is described by the required bandwidth f_BW and the stiffness of the shuttles k_0,

$$C_\mathrm{I}(s) = \frac{K_\mathrm{i}}{s} = \frac{2\pi f_\mathrm{BW} k_0}{s}. \tag{6.6}$$

The bandwidth f_BW is the frequency at which the controller multiplied by the plant has unit gain, also called the crossover frequency [40]. By adding a low-pass or notch filter we can suppress the low-damped resonance frequency peaks if the bandwidth needs to be increased to reach a shorter settling time. This is shown before in [71, 70]. Figure 6.6 shows the schematic diagram of the plant (the MEMS stage), the controllers, the GTF and its inverse.

6.3 Experimental

Designs with two different geometries were fabricated. The only differences were in the coupling between the shuttles and the stage; one design ('SMALL') has a stage leafspring length of 1000 µm and an eccentricity of 150 µm, the other design ('LARGE') has a stage leafspring length of 1500 µm and an eccentricity of 250 µm. No design variations were made for the shuttles. The tilted folded flexures that suspend the shuttles have a leafspring length of 1000 µm, a leafspring thickness of 3 µm and a tilt angle of 85°.

The 3DOF stages in this work are fabricated in a SOI wafer with a device layer thickness of 25 µm, so this is therefore the height of our structures. Lithography and DRIE etching limits the minimum feature size and minimum trench width of the designs to 3 µm. An aspect ratio of 3:25 is safe for directional DRIE etching [58]. HF vapour phase etching of the buried oxide layer (2 µm) is used to release thin and perforated structures from the substrate [49]. The devices were wire-bonded and packaged for measurements. A scanning electron microscope (SEM) image of one of the fabricated 3DOF stages is shown in Figure 6.7.

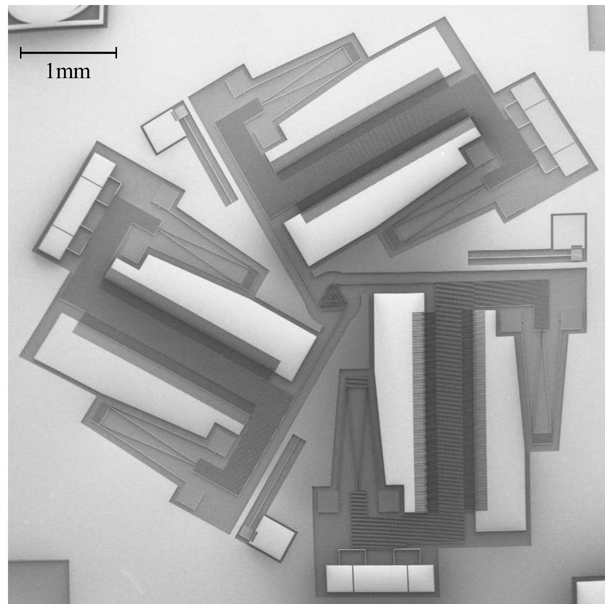

Figure 6.7: A scanning electron microscope image of one of the fabricated 3DOF stages ('LARGE'). Next to the stage leafsprings resonators are integrated to determine the leafspring thickness in the fabricated system.

For position control of the 3DOF stage a MathWorks xPC Target platform is used. This platform runs the control algorithms with a fixed sample frequency of 2 kHz. Texas Instruments OPA454 OpAmps were used for amplification of the

setpoint voltages generated by a National Instruments PCI-6602 in order to generate comb-drive actuation voltages up to 100 V. A resistance in series was used to limit the current to the MEMS stage in case of pull-in (short-circuit). The thermal displacement sensors are measured in a bridge setup with measurement resistors of 200 Ω. A DC supply voltage U_{ss} was used to heat the sensors. The differential bridge output voltage was low-pass filtered at 1.4 kHz to prevent aliasing and reduce high-frequency noise. The voltages were measured using a National Instruments PCI-6221. The 1-σ noise on the sensor voltage was determined to be 40.7 µV with a sensor supply voltage of 10 V. This was the cumulative sensor noise in the frequency band up to 1.4 kHz. The sensor sensitivity was measured to be 1353 V m^{-1} at a 10 V sensor voltage. The 1-σ sensor noise is therefore determined to be 30.1 nm and 0.804 nm/$\sqrt{\text{Hz}}$.

With the described measurement setup we were able to perform a frequency domain identification by providing white noise to the electrostatic actuators, determine the closed-loop time response of the stage, and measure the range of motion in x, y, and R_z of the stage. An optical microscope, a Leica Z16, was used to capture the stage movement with a resolution of approximately 2.5 pixel/µm. Video processing in Matlab was used to determine the stage position and rotation from the captured videos.

6.4 Results

In this section the measurement results are presented. To verify the dominant dynamics a frequency domain identification of the system is performed first (section 6.4.1). Afterwards we show that we are able to control the stage position by control of the shuttle positions (section 6.4.2). Finally the range of motion was measured and compared to existing stages (section 6.4.3).

6.4.1 Identification

To determine the stiffness and resonance frequencies of the 3DOF stage, the system was identified in the frequency domain. White-noise was applied to the input of the comb-drive actuators of each shuttle and the sensor response of the corresponding shuttle was measured. The frequency responses from shuttle force to shuttle position are shown in Figure 6.8. In order to give the frequency response a physical meaning, the actuation voltage is converted to the actuation force in Newton and the sensor voltage is converted to the shuttle displacement in meter. The horizontal line for the frequencies below 100 Hz is the inverse of the mechanical stiffness of the shuttles. The shuttle stiffness is determined from this measurement to be 0.61 N m^{-1} for shuttle 1, 0.58 N m^{-1} for shuttle 2, and 0.66 N m^{-1} for shuttle 3. These values are close to the expected stiffness of 0.60 N m^{-1} as was listed in Table 6.2 for the x and y mode. The variation is most probably caused by tolerances in the fabrication process.

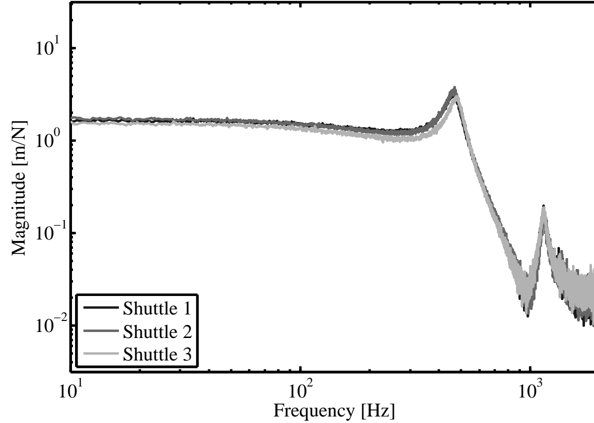

Figure 6.8: The 3DOF stage was identified in the frequency domain by applying white noise to the actuators. The resulting stage position was measured with the integrated sensor corresponding to that shuttle. The first resonance frequencies of the shuttles (∼470 Hz) and the R_z mode (1144 Hz) are distinguished.

From the frequency identification, Figure 6.8, the resonance frequencies of the system were also determined. The first resonance peaks of the shuttles in s_1 (463 Hz), s_2 (468 Hz), s_3 (478 Hz) correspond to the resonance frequencies of the decoupled modes in x and y. The resonance frequency of 1144 Hz was found in the identification of each shuttle. This resonance corresponds to the R_z mode of the system, in which the stage shows a pure rotation caused by equal translation of the shuttles. Between the resonance frequencies in x and y of roughly 470 Hz and the resonance frequency in R_z of 1144 Hz, an 'anti-resonance' in the frequency response is found at a frequency of approximately 970 Hz. The 'anti-resonance' is the sum of the actuated shuttle displacement with a phase lag of 180° and the actuation of the rotational resonance of the 3DOF stage with one actuator blocked. This dynamic behavior is similar to that of a two body mass-spring system that can be described by a fourth order differential equation [114].

We have compared the measured resonance frequencies of the x, y, and R_z mode with SPACAR and ANSYS. First we validated the leafspring thickness of the fabricated stages by three test resonators of which the mass could be estimated accurately and the resonance frequency was determined by measurement. This showed deviations in the leafspring thickness of less than 3 % with respect to the designed value of 3 µm, and less than 1 % on average over three resonators. The leafspring thicknesses in SPACAR and ANSYS were not corrected for these small deviations. The measured and simulated resonance frequencies are given in Table 6.3. The simulated values for the resonance frequencies deviate up to 7 % with respect to the measured values. This can partially be caused by fabrication inaccuracies, but the modelling packages also have their limitations. Since

SPACAR is a multibody modelling package, an estimation of the masses, inertias, and their locations is used in this model. Due to a limited number of mesh elements in ANSYS, it is impossible to include the perforation of shuttles and stage in the these models and an effective value was used. Therefore we conclude that the 3DOF stage behaves as expected with respect to its frequency response. We will apply position control to the stage as described in section 6.2.4.

Table 6.3: Lowest in-plane resonance frequencies of the stage are measured. The measurements are compared with simulated values by SPACAR and by FEM; the results do agree within 7 %.

Mode	SPACAR (Hz)	Measurement (Hz)	FEM (Hz)
s_1	472	463	491
s_2	472	468	491
s_3	472	478	491
R_z	1075	1144	1132

6.4.2 Control

We have applied position control to the shuttles of the 3DOF stage. The first order analytical GTF is used to achieve the required stage displacement and rotation in x, y, and R_z. As was described in section 6.2.4, an integral controller was used for position control of the individual shuttles. The crossover frequency of all three controllers was set to 25 Hz. A first order motion profile was applied as a setpoint for the controllers. The period of this motion profile was decreased from 4 s to 0.25 s. The results are in Figure 6.9. The expected stage response is simulated by assuming that the stage has a stiffness in x and y of $0.601\,\mathrm{N\,m^{-1}}$ and a torsional stiffness in R_z of $1.39 \times 10^{-7}\,\mathrm{N\,m\,rad^{-1}}$, as given in Table 6.2.

We show that control of the position of the individual shuttles with an integral controller can be used for stable position control of the stage. A second conclusion that can be drawn from these measurements is that control of the stage rotation R_z shows a slower time response than control of the stage position in x and y. If the torsional stiffness in R_z is divided by the eccentricity squared (150 µm), the torsional stiffness is converted to an equivalent translational stiffness of $6.2\,\mathrm{N\,m^{-1}}$. This is about ten times higher than the stiffness in x and y. A higher stiffness requires more time for the integrator to settle and therefore the time response of the R_z controller is slower.

6.4.3 Range of Motion

The stroke of our 3DOF stage was determined by describing circles with increasing radius in the xy-plane. We have also applied pure rotations in $+R_z$ and $-R_z$ to the 3DOF stage. We have measured a stroke of 161 µm in x, of 176 µm in y,

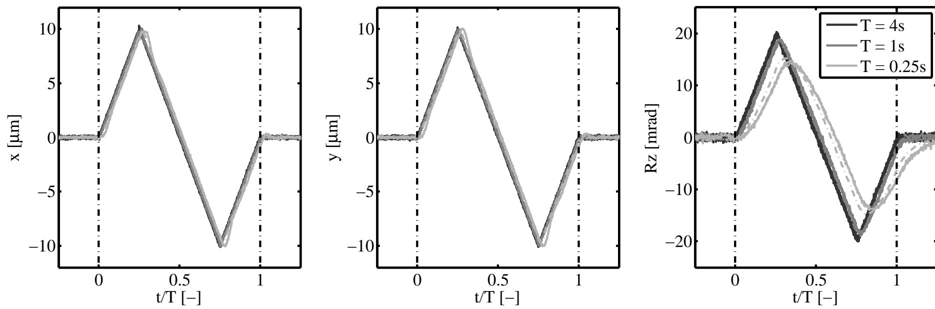

Figure 6.9: A motion profile in x, y, and R_z with different speeds was provided as a setpoint to the control loop. Stable control of the stage position by controlling the position of the three shuttles is shown. Control of the stage rotation is slower than control of the stage position, since the equivalent stiffness of the stage rotation is higher. The simulated stage response is given by the dashed lines, the measured stage response is given by the continuous lines.

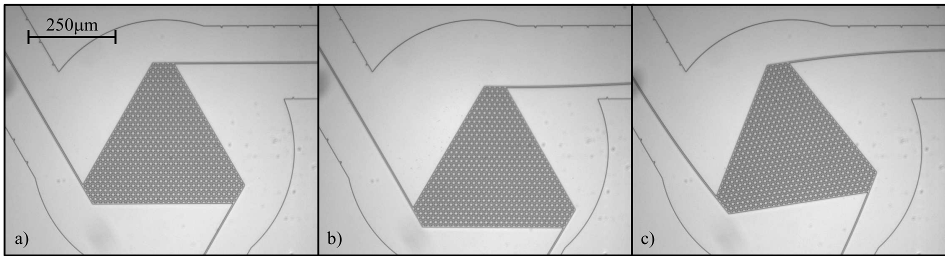

Figure 6.10: The stage in a) neutral, b) deflected , and c) rotated position. The displacement ($x = +60\,\mu\text{m}$, $y = -60\,\mu\text{m}$) and the rotation ($R_z = +160\,\text{mrad}$) of the stage is determined by video analysis.

and a rotation of 325 mrad in R_z by these measurements. The positions that are reached experimentally at zero rotation are given in Figure 6.3. An image of the stage in neutral, deflected, and rotated position is given in Figure 6.10. Since the measurement of the actual pull-in stroke is probably destructive, we have stopped our measurements at approximately 80 % of the expected range of motion.

The measured stroke and rotation of our stage is compared to that of existing stages in literature. Since the stroke of such stages usually is related to the wafer footprint of the complete system, the ratio between the range of the stage and the footprint of the system is used; the range of the stage in the xy-plane is the area of the circle or ellipse in m^2 ($\pi xy/4$), and the footprint is the rectangular area of the device in m^2 ($w \times h$). w and h are the width and the height of the devices, which was reported most of the times and sometimes needed to be derived from the figures. The results of this comparison are given in Table 6.4 and Figure 6.11.

The measured range of motion of our device, 161 µm in x, 175 µm in y, and a

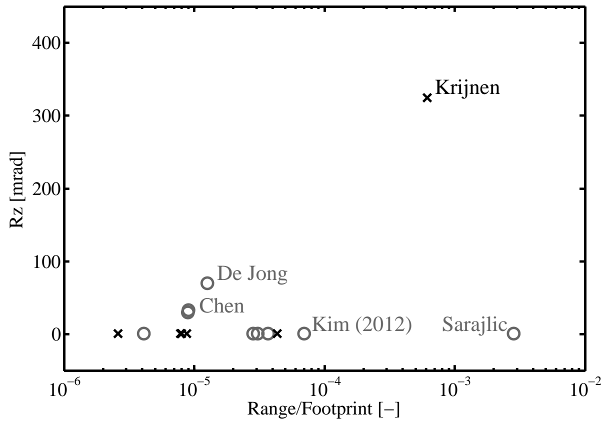

Figure 6.11: The range of motion of our stage is compared to the range of motion of existing stages, taking into account the wafer footprint of the stages. Cross markers indicate stages with integrated feedback, circular markers indicate stages without integrated feedback. When taking the wafer footprint into account, only the stepper stage of Sarajlic exceeds the in-plane displacement of our stage. In absolute sense, the range of motion of our device exceeds the displacement and rotation of existing stages.

rotation of 325 mrad, exceeds the range of motion of existing stages. The stage of Lantz *et al.* [79] is the only other stage that reaches displacements over 100 µm. This stage does not include a rotational DOF and requires a footprint that is more than 7 times larger than the footprint of our stage. If the range of motion is divided by the wafer footprint, as shown in Figure 6.11, the stepper stage of Sarajlic et al. [113] is the only one superior to our stage with respect to in-plane motion. However, the stage of Sarajlic et al. does not include a rotational DOF and does not include feedback. Finally, we conclude that the stage presented in this work is the only known positioning stage that provides more than 2DOFs and has integrated feedback.

6.5 Conclusions

We have designed, fabricated, and validated a large-stroke 3DOF positioning stage with integrated displacement sensors for feedback control in a single-mask MEMS fabrication process. The measured stroke of this stage was 161 µm in x, 175 µm in y direction, and 325 mrad in rotation. This exceeds the range of motion of existing stages. The first resonance frequency of the shuttles was measured to be approximately 470 Hz. Below this frequency the stage behaves as a pure stiffness, to which we applied stable position control with a crossover frequency of 25 Hz. The resonance frequency as well as the stiffness of the shuttles were determined to be within 7 % with respect to the simulated values by SPACAR and ANSYS.

We have also demonstrated a method to reduce the stage position error by introducing the non-linear geometric transfer function. With this method stage position errors of the fabricated stages can be reduced by means of (optical) calibration. At zero rotation the range of motion of the 3DOF stage is described roughly by a hexagon with six equal sides, which represent pull-in in push- and in pull-direction of the three shuttles. Three parameters have been varied to find their influence on the stage translational and rotational range of motion. Increasing the stage leafspring length will increase the stroke and rotation of the stage. An optimum in the eccentricity with respect to the stroke of the stage is found at 175 µm. These simulation results can be used to design stages with different specifications.

Table 6.4: Multi-DOF stages from literature are listed. This data is used to compare the stroke and rotation of our work to that of existing stages. The ratio between the range of the stage and the wafer footprint is used to compare our stage to existing stages, graphically presented in Figure 6.11.

Year	**First author [Reference]**	**Stroke (DOF)** µm, mrad	**Range** µm^2	**Footprint** mm×mm	**Range /Footprint** m^2/m^2	**Feedback**
2002	Kim [65]	48, 48 (x, y)	1.81×10^3	7×7	3.69×10^{-5}	No
2005	Sarajlic [113]	60, 60 (x, y)	2.83×10^3	1×1	2.83×10^{-3}	No
2006	Chen [17]	8, 13, 9 (x, y, z) 19, 18, 33 (R_x, R_y, R_z)	8.17×10^1	3×3	9.08×10^{-6}	No
2007	Liu [83]	25, 25, 3.5 (x, y, z)	4.91×10^2	4×4	3.07×10^{-5}	No
2008	Mukhopadhyay [91]	27, 27, 30 (x, y, R_z)	5.73×10^2	8×8	8.95×10^{-6}	No
2009	Dong [31]	24, 24, 7 (x, y, z)	4.52×10^2	4×4	2.83×10^{-5}	No
2009	Engelen [39]	52, 38 (x, y)	1.55×10^3	19×20	4.08×10^{-6}	No
2010	De Jong [28]	20, 20, 70 (x, y, R_z)	3.14×10^2	5×5	1.26×10^{-5}	No
2012	Kim [66]	50, 50 (x, y)	1.96×10^3	7×4	7.01×10^{-5}	No
2003	Chu [22]	19, 19 (x, y)	2.84×10^2	6×6	7.88×10^{-6}	Yes
2007	Lantz [79]	134, 112 (x, y)	1.18×10^4	16×17	4.33×10^{-5}	Yes
2008	Sun [122]	20, 20 (x, y)	3.14×10^2	11×11	2.60×10^{-6}	Yes
2012	Choi [21]	32, 32 (x, y)	8.04×10^2	10×10	8.04×10^{-6}	Yes
2013	Rakotondrabe [108]	10, 10 (x, y)	7.85×10^1	3×3	8.73×10^{-6}	Yes
2014	Krijnen (this work)	161, 175, 325 (x, y, R_z)	2.21×10^4	6×6	6.15×10^{-4}	Yes

Chapter 7

Discussion and conclusions

Two main objectives were formulated in the introducion, 1) the development of a large-stroke closed-loop positioning system using a simple fabrication scheme and no assembly, and 2) understanding the opportunities and limitations of positioning and manipulation in MEMS for use in future mechatronic applications. This chapter describes the outcome of this research with respect to these objectives.

7.1 Discussion

Working with MEMS requires a different way of thinking. On the microscale alternative sensing and actuation principles can meet the requirements. Examples from this thesis are the electrostatic actuator and the thermal sensor. Results with respect to the generic objective, *understanding the opportunities and limitations of positioning and manipulation in MEMS for use in future mechatronic applications*, are formulated in this section.

Requirements
In general, opportunities for MEMS are applications where the system needs to have a small volume. Due to the small size and low mass, eigenfrequencies are typically high and MEMS are shock resistant. On the other hand, surface effects like stiction and viscous damping have a large influence on the performance. The absolute maximum actuator force, the range of motion, and the stiffness are relatively small; rough limits are 1 mN, 250 µm, and $10\,\mathrm{N\,m^{-1}}$.

Fabrication
Although the tolerances on the fabrication process are relatively large, the use of single-crystalline silicon in combination with flexure mechanisms make the devices suitable for accurate and repeatable positioning. A simple MEMS fabrication process can result in devices that are cheap in mass production. Still it takes considerable time, cost, and effort to achieve a high yield. In the design of new MEMS applications an existing fabrication process is therefore preferred. MEMS are sensitive to external load forces and contamination, so handling and packaging are important steps after fabrication.

Verification
The small surfaces of MEMS make characterization by external accurate position measurement systems difficult (capacitive or interferometric). Integration of test structures is therefore recommended, like resonators to determine the thickness of a beam. Furthermore, specific and expensive equipment is required when working with MEMS. Apparatus used in this research are among others the electron microscope, the probe station, the wire bonder, the white light interferometer and the laser doppler vibrometer.

7.2 Conclusions

With respect to the main objective, *the development of a large stroke closed-loop positioning system using a simple fabrication scheme and no assembly*, we can state that this objective is accomplished and a closed-loop positioning stage was designed, fabricated, and validated by measurements. With respect to the goals described in the introduction, more specific conclusions regarding the research can be drawn.

The extension of the stroke with respect to currently available MEMS stages
By taking into account the mechanical characteristics of a MEMS flexure it is possible to increase the output stroke and force or to decrease the required wafer surface area when using electrostatic actuators (Chapter 2). We have demonstrated several flexure mechanisms that are able to reach a stroke of ±100 µm with footprints between 2.4 mm^2 and 5.6 mm^2. With respect to wafer footprint the tilted folded flexure is in this case the preferred flexure mechanism.

The electrostatic comb-drives are usually suspended by elastic straight-line mechanisms. These flexures cause the shuttle to have, besides the intended longitudinal displacement, a lateral and angular displacement. This results in misalignment of the comb-drive fingers in the actuator. In this work we have presented results on pull-in of individual, misaligned comb-drive fingers (Chapter 3). An asymptotic expression for the pull-in voltage for a finger with a lateral base displacement and a base rotation has been derived. Finite element models show that fringe fields towards the handle wafer tend to lower this pull-in voltage. Measurements on the pull-in of intentionally misaligned fingers agree within 10 % to the finite element models that take these fringe fields into account.

For our designs in Chapter 2 we have used a safety margin of slightly more than 20 % on the maximum comb-drive voltage to avoid finger pull-in due to lateral deflections and fringe fields towards the handle wafer.

Addition of a position sensor in the system to provide feedback
A thermal displacement sensor is presented in this work (Chapter 4). The transfer of heat by conductivity through air from a hot sensor structure towards the moving stage is the basic principle behind this sensor. Due to the small size of the MEMS structures, the thermal sensor can still achieve reasonably high bandwidths, over 300 Hz, in contrast with thermal systems in the macro world. With this sensor we have achieved a resolution of 1.6 nm over a stroke of over 100 µm. To reach this resolution we have applied low-pass filtering over the sensor output with a cut-off frequency of 25 Hz.

Characterization of the system components in a vacuum environment
The electrostatic actuator, viscous damping, and sensor response of a single-DOF stage have been characterized in vacuum (Chapter 5). The decreasing sensor response and the increasing Q-factor of the stage were described quantitatively for pressures down to 1 mbar. An integral controller with low-pass and notch filter and a cross-over frequency of 50 Hz were demonstrated to provide stable position control. At ambient pressure and at 1 mbar the settling times are all below 5 ms.

The design of a MEMS-based positioning stage for in-plane movement
A parallel kinematic stage was designed, fabricated, and validated. The stage consists of three electrostatically actuated shuttles with thermal displacement sensors for feedback. The range of motion of our 3DOF stage is >160 µm in x and y direction and 325 mrad in rotation. This exceeds the range of motion of existing stages, with and without taking into account the device footprint (Chapter 6).

Integration of the complete system in a simple fabrication scheme without the use of assembly

An important advantage of the 3DOF stage that is developed in this research project is the integration of the complete system in the device layer of a SOI-wafer. This means that no assembly is required and the complete system can be fabricated using only a single mask, which are both beneficial with respect to cost and performance. Although the fabrication tolerances and inaccuracies are fairly large, the flexure-based design results in a very repeatable behavior. By means of calibration a high resolution can be achieved (Chapter 6).

Appendix A: Process Description

A schematic overview of the process used for the fabrication of the devices in this thesis is given in Figure A.1:

a) A silicon-on-insulator (SOI) wafer is the starting point.

b) Photoresist is applied by spin coating and baking.

c) A mask is produced by laser writing, the photoresist is patterned by contact UV lithography.

d) The photoresist is developed.

e) Directional deep reactive-ion etching (DRIE) is used for structuring of the silicon device layer.

f) The remaining photoresist is removed.

g) Vapor phase HF (VHF) is used for isotropic etching of the buried oxide layer (SiO_2).

h) Before use the devices need to be diced, wirebonded and packaged.

A critical step in the fabrication process is the VHF release (step g). To show how thin and perforated structures are released and large structures stay anchored, this fabrication step is schematically given from a top view in Figure A.2:

a) After DRIE etching the buried oxide layer is visible from a top view.

b) The isotropic VHF etching has removed the 'field oxide' and has made a start underetching the structures. From the top no more buried oxide is visible, however thin structures are not yet released.

c) VHF etching is stopped when thin structures are released from the handle wafer.

d) The released structures move when a force is applied.

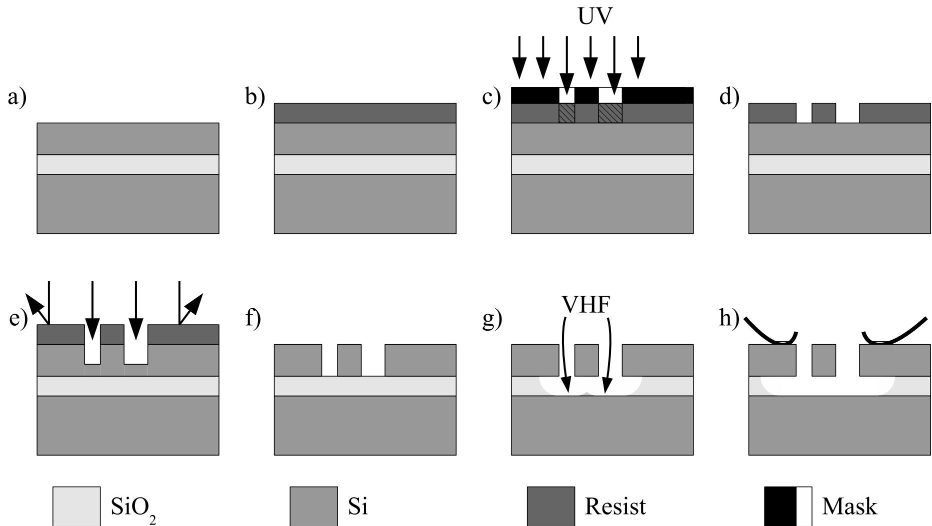

Figure A.1: A schematic overview of the fabrication process based on a silicon-on-insulator (SOI) wafer. The top silicon layer (Si) is structured by deep reactive-ion etching (DRIE), the insulator layer (SiO_2) is etched by vapor phase HF (VHF).

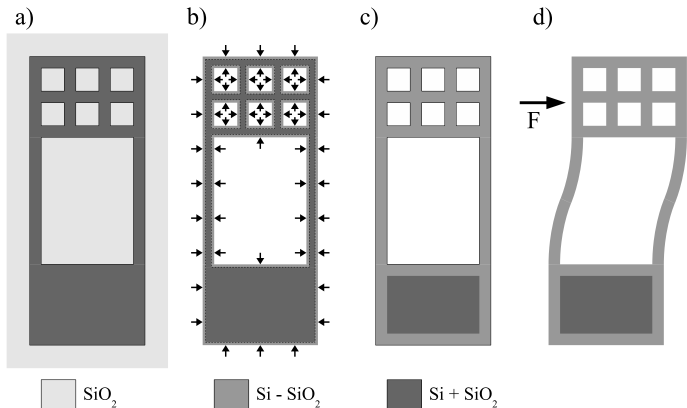

Figure A.2: VHF etching is a critical step in the fabrication of the devices. After VHF the devices are sensitive to among others humidity, electrostatic discharge, and contamination.

Appendix B: Images

In this appendix additional images of fabricated MEMS devices are given. Most images are made using a scanning electron microscope (SEM).

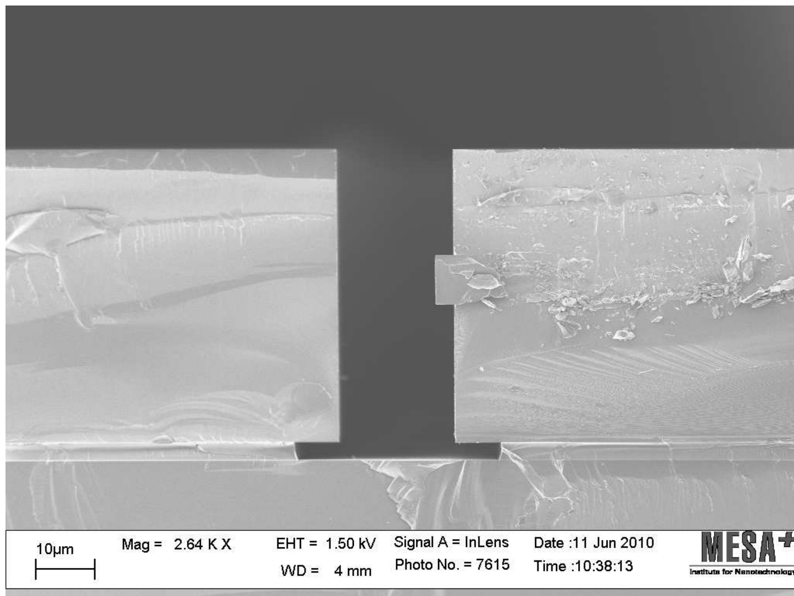

Figure B.1: SEM image of the cross-section of a fabricated device. The image clearly shows the result of the directional DRIE and isotropic VHF etching.

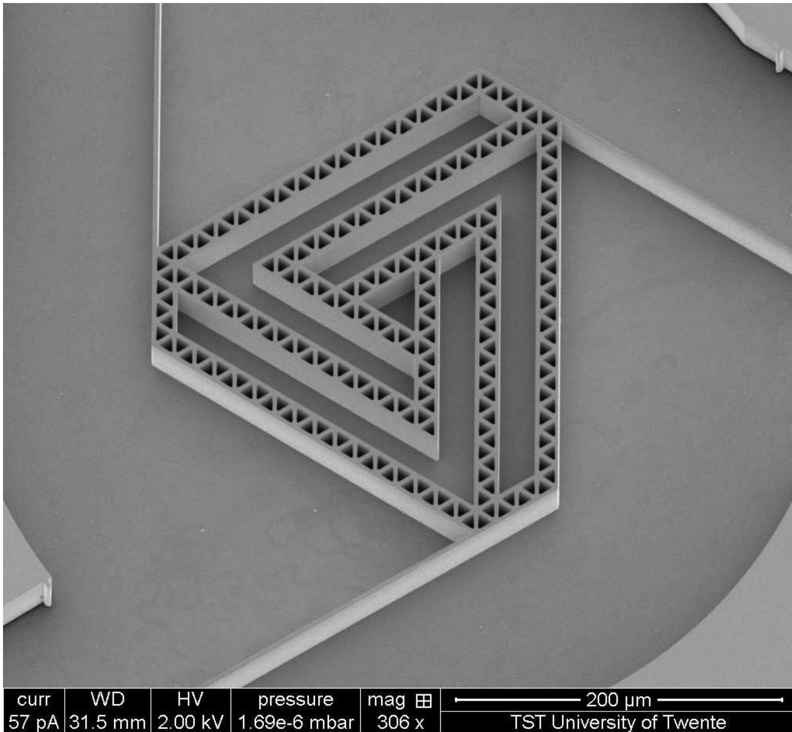

Figure B.2: SEM image of a 3DOF stage with its three connections to the actuated shuttles.

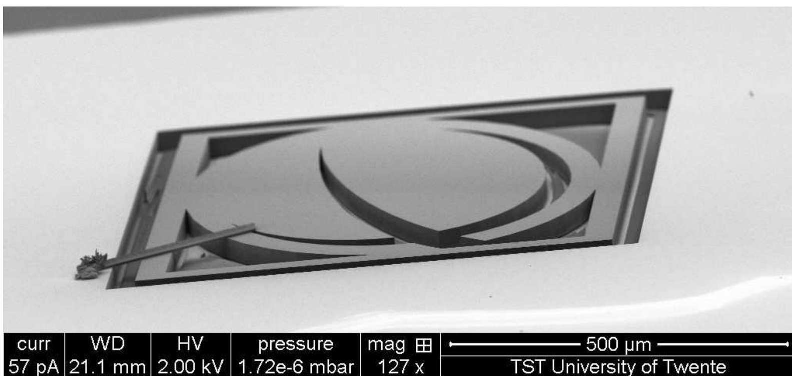

Figure B.3: SEM image of the Demcon logo in the device layer of a SOI wafer. Part of a broken leafspring is located in the bottom left.

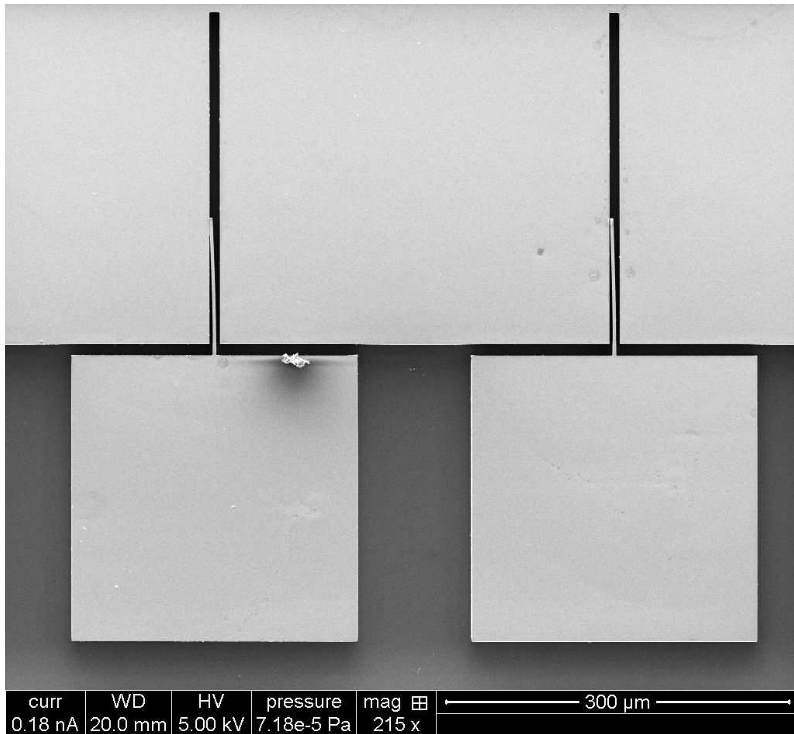

Figure B.4: SEM image of two test structures on which the limit point voltage for finger pull-in was measured.

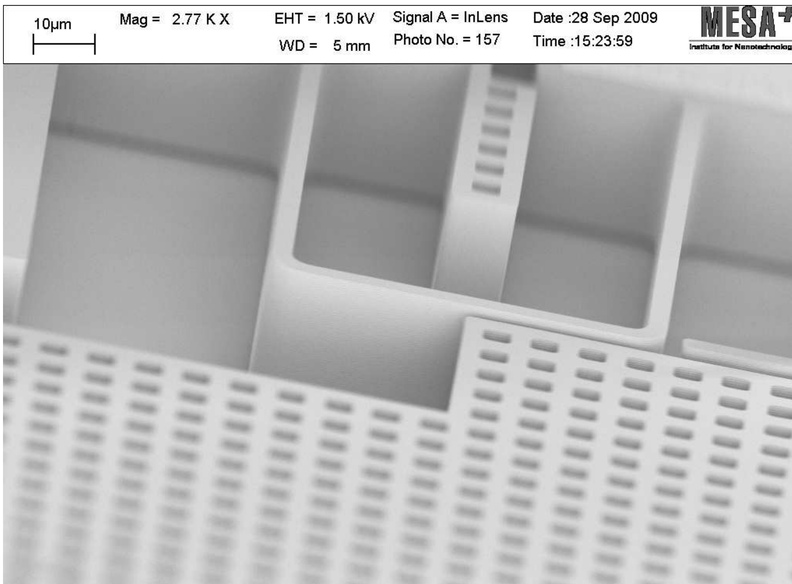

Figure B.5: SEM image of one of the heaters of the thermal displacement sensor. The heater shows half overlap with the perforated stage.

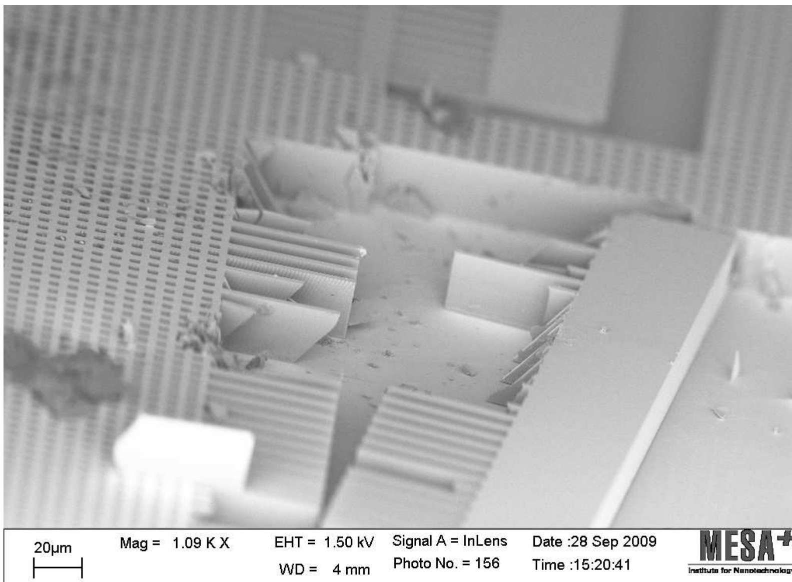

Figure B.6: SEM image of a broken device. For inspection the released stages are sometimes removed by tape, what remains is this apocalyptic scenery.

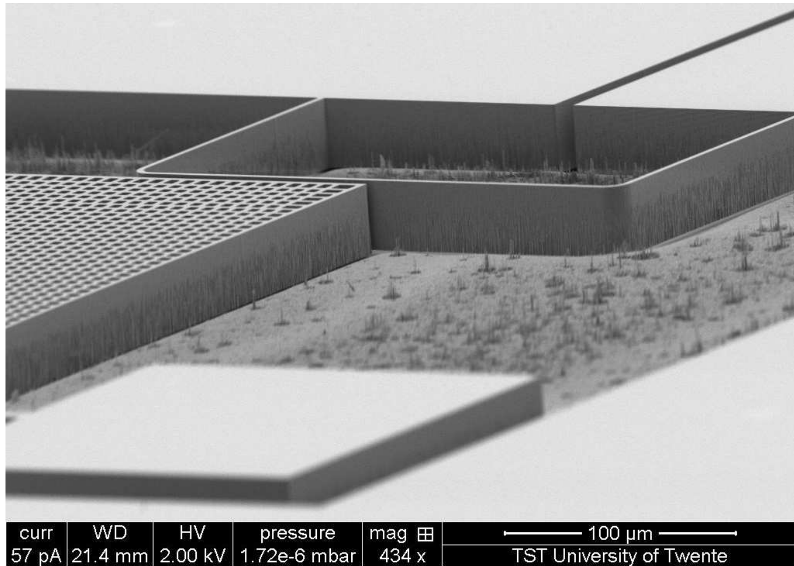

Figure B.7: SEM image of a stage in front of a thermal displacement sensor. DRIE etching is not a uniform process over the wafer surface, which sometimes results in fields of silicon 'grass'.

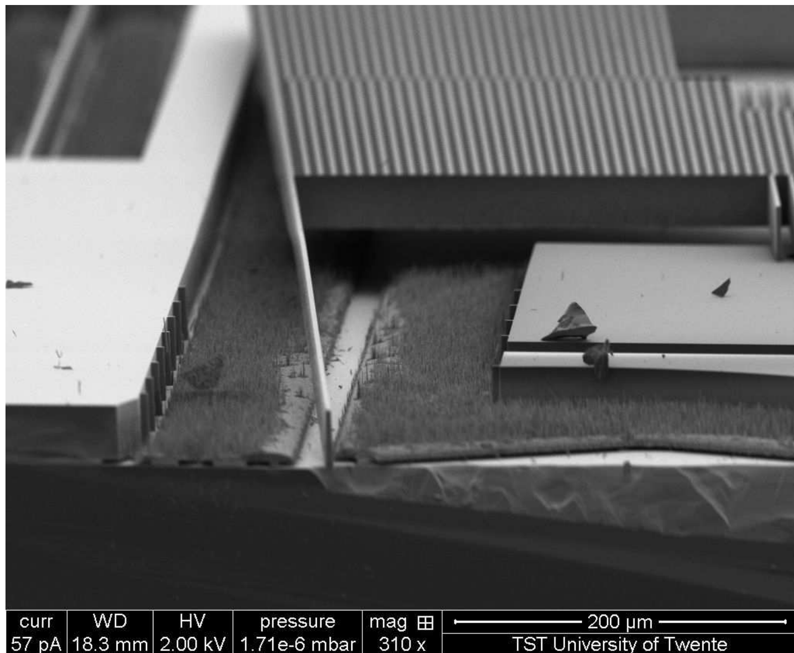

Figure B.8: SEM image of a broken stage that hangs over a field of silicon 'grass'.

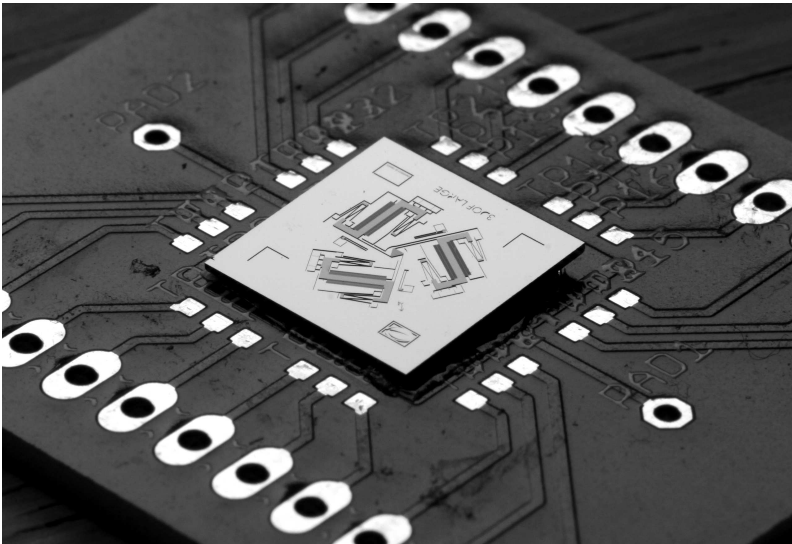

Figure B.9: A digital camera image of the 3DOF stage. Using a macro lens, one can still see some details of the MEMS device (size: $8x8mm^2$).

Bibliography

[1] 20-sim. http://www.20sim.com/, 2010.

[2] S. Abu-Salih and D. Elata. Experimental validation of electromechanical buckling. *Journal of Microelectromechanical Systems*, 15(6):1656–1662, 2006.

[3] J.S. Aden, J.H. Bohrquez, D.M. Collins, M.D. Crook, A. Garca, and U.E. Hess. The third-generation hp thermal inkjet printhead. Technical report, Hewlett-Packard, http://citeseerx.ist.psu.edu/viewdoc/download?doi=10.1.1.362.3312&rep=rep1&type=pdf, 1994.

[4] W.J. Alvesteffer, D.C. Jacobs, and D.H. Baker. Miniaturized thin film thermal vacuum sensor. *Journal of Vacuum Science & Technology A*, 13(6):2980–2985, 1995.

[5] M. Asheghi, B. Behkam, K. Yazdani, R. Yoshi, and K. Goodson. Thermal conductivity model for thin silicon-on-insulator layers at high temperatures. In *Proceedings of 2002 IEEE International SOI Conference*, pages 51–52, Williamsburg, VA, USA, 2002.

[6] D.G. Ashwell. The anticlastic curvature of rectangular beams and plates. *Journal of Royal Aeronautical Society*, 54:708–715, 1950.

[7] S. Awtar, A.H. Slocum, and E. Sevincer. Characteristics of beam-based flexure modules. *Journal of Mechanical Design*, 129(6):625–639, 2007.

[8] M. Bao and H. Yang. Squeeze film air damping in mems (review). *Sensors and Actuators A*, 136(1):3–27, 2007.

[9] Y. Bellouard, A.A. Said, M. Dugan, and P. Bado. High accuracy microdisplacement sensor with integrated optics-based detection means. In *Proceedings IEEE International Conference on Robotics and Automation*, pages 850–855, Barcelona, Spain, 2005.

[10] G.K. Binnig, C.F. Quate, and C. Gerber. Atomic force microscope. *Physical Review Letters*, 56(9):930–933, 1986.

[11] D.M. Brouwer, J.P. Meijaard, and J.B. Jonker. Large deflection stiffness analysis of parallel prismatic leaf-spring flexures. *Precision Engineering*, 37(3):505–521, 2013.

[12] D.M. Brouwer, A. Otten, J.B.C. Engelen, B. Krijnen, and H.M.J.R. Soemers. Long-range elastic guidance mechanisms for electrostatic comb-drive actuators. In *Proceedings of the 10th EUSPEN International conference*, volume 1, pages 462–465, Delft, The Netherlands, 2010.

[13] V. Cazcarra and P. Zunino. Influence of oxygen on silicon resistivity. *Journal of Applied Physics*, 51(8):4206–4211, 1980.

[14] A. Chambers. *Modern Vacuum Physics*. CRC PressINC, Boca Raton, Florida, USA, 1st edition, 2004.

[15] C. Chen and C. Lee. Design and modeling for comb drive actuator with enlarged static displacement. *Sensors and Actuators A*, 115(2-3):530–539, 2004.

[16] G. Chen. *Nanoscale Energy Transport and Conversion: A Parallel Treatment of Electrons, Molecules, Phonons, and Photons*. Oxford University Press, New York, NY, USA, 1st edition, 2005.

[17] S.C. Chen and M.L. Culpepper. Design of a six-axis micro-scale nanopositioner muhexflex. *Precision Engineering*, 30(3):314–324, 2006.

[18] P. Cheung, R. Horowitz, and R.T. Howe. Design, fabrication, position sensing, and control of an electrostatically-driven polysilicon microactuator. *IEEE Transactions on Magnetics*, 32(1):122–128, 1996.

[19] S.H. Choa. Reliability of vacuum packaged mems gyroscopes. *Microelectronics Reliability*, 45:361–369, 2004.

[20] S.H. Choa. Reliability of mems packaging: vacuum maintenance and packaging induced stress. *Microsystem Technologies*, 11:1187–1196, 2005.

[21] Y.S. Choi, Y. Zhang, and D.W. Lee. A thermal-driven silicon micro xy-stage integrated with piezoresistive sensors for nano-positioning. *Journal of Micromechanics and Microengineering*, 22(5):055002, 2012.

[22] L.L. Chu and Y.B. Gianchandani. A micromachined 2D positioner with electrothermal actuation and sub-nanometer capacitive sensing. *Journal of Micromechanics and Microengineering*, 13(2):279–285, 2003.

[23] J.H. Comtois, M.A. Michalicek, and C.C. Barron. Electrothermal actuators fabricated in four-level planarized surface micromachined polycrystalline silicon. *Sensors and Actuators A*, 70(1):23–31, 1998.

[24] R.J. Corruccini. Gaseous heat conduction at low pressures and temperatures. *Vacuum*, 70(1):19–29, 1959.

[25] R. Danev, R.M. Glaeser, and K. Nagayama. Practical factors affecting the performance of a thin-film phase plate for transmission electron microscopy. *Ultramicroscopy*, 109(4):312–325, 2009.

[26] U.A. Dauderstdt, P.H.S. de Vries, R. Hiratsuka, and P.M. Sarro. Silicon accelerometer based on thermopiles. *Sensors and Actuators A*, 7-8:201–204, 1995.

[27] E.J. Davis. A history and state-of-the-art of accommodation coefficients. *Atmospheric Research*, 82(3-4):561–578, 2006.

[28] B.R. de Jong, D.M. Brouwer, M.J. de Boer, H.V. Jansen, H.M.J.R. Soemers, and G.J.M. Krijnen. Design and fabrication of a planar three-dofs mems-based manipulator. *Journal of Microelectromechanical Systems*, 19(5):1116–1130, 2010.

[29] J.P. den Hartog. *Mechanical Vibrations*. McGraw-Hill, New York, USA, 4th edition, 1956.

[30] C.M. DiBiasio and M.L. Culpepper. Design of a meso-scale six-axis nanopositioner with integrated position sensing. In *Proceedings Fifth Annual International Symposium on Nanomanufacturing*, Delft, The Netherlands, 2008.

[31] J. Dong and P.M. Ferreira. Electrostatically actuated cantilever with soi-mems parallel kinematic xy stage. *Journal of Microelectromechanical Systems*, 18(3):641–651, 2009.

[32] J.M. Dorkel and P. Leturcq. Carrier mobilities in silicon semi-empirically related to temperature, doping and injection level. *Solid-state electronics*, 24(9):821–825, 1981.

[33] U. Durig. Fundamentals of micromechanical thermoelectric sensors. *Journal of Applied Physics*, 98(4):044906, 2005.

[34] W.P. Eaton and J.H. Smith. Micromachined pressure sensors: review and recent developments. *Smart Materials and Structures*, 6(5):530–539, 1997.

[35] D. Elata and V. Leus. How slender can comb-drive fingers be? *Journal of Micromechanics and Microengineering*, 15(5):1055–1059, 2005.

[36] E. Eleftheriou, T. Antonakopoulos, G. K. Binnig, G. Cherubini, M. Despont, A. Dholakia, U. Drig, M. A. Lantz, H. Pozidis, H. E. Rothuizen, and P. Vettiger. Millipede - a mems-based scanning-probe data-storage system. *IEEE Transactions on Magnetics*, 39(2):938–945, 2003.

[37] A. Ellett and R.M. Zabel. The pirani gauge for the measurement of small changes of pressure. *Physical Review*, 37(9):1102–1111, 1931.

[38] J.B.C. Engelen, H. de Boer, J.G. Beekman, L.C. Fortgens, D.B. de Graaf, S. Vocke, and L. Abelmann. The micronium-a musical mems instrument. *Journal of Microelectromechanical Systems*, 21(2):262–269, 2012.

[39] J.B.C. Engelen, H.E. Rothuizen, U. Drechsler, R. Stutz, M. Despont, L. Abelmann, and M.A. Lantz. A mass-balanced through-wafer electrostatic x/y-scanner for probe data storage. *Microelectronic Engineering*, 86(4-6):1230–1233, 2009.

[40] G.F. Franklin, J.D. Powell, and A. Emami-Naeini. *Feedback Control of Dynamic Systems.* Addison-Wesley, Boston, MA, USA, 3rd edition, 1994.

[41] J.M. Gere and S.P. Timoshenko. *Mechanics of Materials.* Chapman and Hall, London, UK, 3rd edition, 1991.

[42] V.M. Glazov and A.S. Pashinkin. The thermophysical properties (heat capacity and thermal expansion) of single-crystal silicon. *High Temperature*, 39(3):413–419, 2001.

[43] J.D. Grade, H. Jerman, and T.W. Kenny. Design of large deflection electrostatic actuators. *Journal of Microelectromechanical Systems*, 12(3):335–343, 2003.

[44] J.D. Grade, K.Y. Yasumura, and H. Jerman. Electrothermal actuators fabricated in four-level planarized surface micromachined polycrystalline silicon. *Sensors and Actuators A*, 114(3):413–422, 2004.

[45] P. Greiff, B. Boxenhorn, T.King, and L.Niles. Silicon monolithic micromechanical gyroscope. In *Solid State Sensors and Actuators*, volume 1, pages 966–968, San Francisco, CA, USA, 1991.

[46] H. Hammer. Analytical model for comb-capacitance fringe fields. *Journal of Microelectromechanical Systems*, 19(1):175–182, 2010.

[47] R. Hickey, D. Sameoto, T. Hubbard, and M. Kujath. Time and frequency response of two-arm micromachined thermal actuators. *Journal of Micromechanics and Microengineering*, 13(1):40–46, 2003.

[48] R.P. Hogervorst, B. Krijnen, D.M. Brouwer, J.B.C. Engelen, and U. Staufer. A single-mask thermal displacement sensor in mems. In *Proceedings of the 10th EUSPEN International conference*, volume 1, pages 47–50, Delft, The Netherlands, 2010.

[49] P.J. Holmes and J.E. Snell. A vapour etching technique for the photolithography of silicon dioxide. *Microelectronics and reliability*, 5(4):337–341, 1966.

[50] M.A. Hopcroft, W.D. Nix, and T.W. Kenny. What is the young's modulus of silicon. *Journal of Microelectromechanical Systems*, 19(2):229–238, 2010.

[51] J.B. Hopkins and M.L. Culpepper. Synthesis of multi-degree of freedom, parallel flexure system concepts via freedom and constraint topology (fact) - part i: Principles. *Precision Engineering*, 34(2):259–270, 2010.

[52] L.J. Hornbeck. Digital light processing for high-brightness, high-resolution applications. In *Electronic Imaging '97*, pages 1–14, 1997.

[53] D.A. Horsley, N. Wongkomet, R. Horowitz, and A.P. Pisano. Precision positioning using a microfabricated electrostatic actuator. *IEEE Transactions on Magnetics*, 35(2):993–999, 1999.

[54] M.T.K. Hou, G.K.W. Huang, J.Y. Huang, K.M. Liao, R. Chen, and J.L.A. Yeh. Extending displacements of comb drive actuators by adding secondary comb electrodes. *Journal of Micromechanics and Microengineering*, 16(4):684–691, 2006.

[55] L.L. Howell. *Compliant Mechanisms*. John Wiley & Sons, New York, USA, 1st edition, 2001.

[56] F.P. Incropera and D.P. DeWitt. *Introduction to Heat Transfer*. John Wiley & Sons, New York, USA, 3rd edition, 1996.

[57] J.H. Lienhard IV and J.H. Lienhard V. *A heat transfer textbook*. Phlogiston press, Cambridge, MA, USA, 3rd edition, 2008.

[58] H.V. Jansen, M.J. de Boer, S. Unnikrishnan, M.C. Louwerse, and M.C. Elwenspoek. Black silicon method X: a review on high speed and selective plasma etching of silicon with profile control: an in-depth comparison between bosch and cryostat DRIE processes as a roadmap to next generation equipment. *Journal of Micromechanics and Microengineering*, 19(3):1–41, 2009.

[59] J.H. Jerman and J.D. Grade. Miniature device with translatable member. *US Patent 6,664,707 B2*, 2003.

[60] W.A. Johnson and L.K. Warne. Electrophysics of micromechanical comb actuators. *Journal of Microelectromechanical Systems*, 4(1):49–59, 1995.

[61] R.V. Jones. Some uses of elasticity in instrument design. *Journal of Scientific Instruments*, 39(5):193, 1962.

[62] J.B. Jonker and J.P. Meijaard. Spacar - computer program for dynamic analysis of flexible spatial mechanisms and manipulators. In W. Schiehlen, editor, *Multibody Systems Handbook*, pages 123–143. Springer, 1990.

[63] V. Kaajakari, T. Mattila, A. Oja, and H. Sepp. Nonlinear limits for single-crystal silicon microresonators. *Journal of Microelectromechanical Systems*, 13:715–724, 2004.

[64] E.H. Kennard. *Kinetic Theory of Gases.* McGraw-Hill, New York, USA, 1938.

[65] C.H. Kim and Y.K. Kim. Micro xy-stage using silicon on a glass substrate. *Journal of Micromechanics and Microengineering*, 12(2):103–107, 2002.

[66] Y.S. Kim, J.M. Yoo, S. H. Yang, Y.M. Choi, N.G. Dagalakis, and S.K. Gupta. Design, fabrication and testing of a serial kinematic mems xy stage for multifinger manipulation. *Journal of Micromechanics and Microengineering*, 22(8):085029, 2012.

[67] W.T. Koiter. *Over de stabiliteit van het elastisch evenwicht.* PhD thesis, TU Delft, 1945.

[68] M.P. Koster. *Constructieprincipes voor het nauwkeurig bewegen en positioneren.* PPI Uitgeverij, Enschede, NL, 4th edition, 2005.

[69] B. Krijnen and D.M. Brouwer. Flexures for large stroke electrostatic actuation in mems. *Journal of Micromechanics and Microengineering*, 24(1):015006, 2014.

[70] B. Krijnen, D.M. Brouwer, L. Abelmann, and J.L. Herder. Vacuum performance and control of a mems stage with integrated thermal position sensor. In *Proceedings of the 14th EUSPEN International conference*, volume 2, pages 435–438, Dubrovnik, Croatia, 2014.

[71] B. Krijnen, D.M. Brouwer, L. Abelmann, and J.L. Herder. Vacuum behavior and control of a mems stage with integrated thermal displacement sensor. *Sensors and Actuators A: Physical*, 2014 (submitted).

[72] B. Krijnen, R.P. Hogervorst, J.W. Van Dijk, J.B.C. Engelen, D.M. Brouwer, and L. Abelmann. Single-mask thermal displacement sensor in mems. In *Proceedings of the MME 2010 International Workshop*, pages 52–55, Enschede, The Netherlands, 2010.

[73] B. Krijnen, R.P. Hogervorst, J.W. van Dijk, J.B.C. Engelen, L.A. Woldering, D.M. Brouwer, L. Abelmann, and H.M.J.R. Soemers. A single-mask thermal displacement sensor in mems. *Journal of Micromechanics and Microengineering*, 21(7):074007, 2011.

[74] B. Krijnen, K.R. Swinkels, D.M. Brouwer, L. Abelmann, and J.L. Herder. A large-stroke 3dof stage with integrated feedback in mems. *Journal of Microelectromechanical Systems*, 2014 (to be submitted).

[75] B. Krijnen, K.R. Swinkels, D.M. Brouwer, and J.L. Herder. Position control of a mems stage with integrated sensor. In *Proceedings of the 13th EUSPEN International conference*, volume 1, pages 322–325, Berlin, Germany, 2013.

[76] A.A. Kuijpers, G.J.M. Krijnen, R.J. Wiegerink, T.S.J. Lammerink, and M.C. Elwenspoek. A micromachined capacitive incremental position sensor: part 1. analysis and simulations. *Journal of Micromechanics and Microengineering*, 16(6):S116–S124, 2006.

[77] A.A. Kuijpers, G.J.M. Krijnen, R.J. Wiegerink, T.S.J. Lammerink, and M.C. Elwenspoek. A micromachined capacitive incremental position sensor: part 2. experimental assessment. *Journal of Micromechanics and Microengineering*, 16(6):S125–S134, 2006.

[78] M.A. Lantz, G.K. Binnig, M. Despont, and U. Drechsler. A micromechanical thermal displacement sensor with nanometre resolution. *Nanotechnology*, 16(8):1089–1094, 2005.

[79] M.A. Lantz, H.E. Rothuizen, U. Drechsler, W. Hberle, and M. Despont. A vibration resistant nanopositioner for mobile parallel-probe storage applications. *Journal of Microelectromechanical Systems*, 16(1):130–139, 2007.

[80] R. Legtenberg, A.W. Groeneveld, and M.C. Elwenspoek. Comb-drive actuators for large displacements. *Journal of Micromechanics and Microengineering*, 6(3):320–329, 1996.

[81] R. Legtenberg and H.A.C. Tilmans. Electrostatically driven vacuum-encapsulated polysilicon resonators part i. design and fabrication. *Sensors and Actuators A*, 45:57–66, 1994.

[82] R. Legtenberg and H.A.C. Tilmans. Electrostatically driven vacuum-encapsulated polysilicon resonators part ii. theory and performance. *Sensors and Actuators A*, 45:67–84, 1994.

[83] X. Liu, K. Kim, and Y. Sun. A mems stage for 3-axis nanopositioning. *Journal of Micromechanics and Microengineering*, 17(9):1796–1802, 2007.

[84] N. Maluf and K. Williams. *An introduction to Microelectromechanical Systems Engineering*. Artech House, Boston, MA, USA, 2nd edition, 2004.

[85] J.P. Meijaard. Validation of flexible beam elements in dynamics programs. *Nonlinear Dynamics*, 9(1):21–36, 1996.

[86] J.P. Meijaard. Refinements of classical beam theory for beams with a large aspect ratio of their cross-sections. In *Proceedings of the IUTAM Symposium on Dynamics Modeling and Interaction Control in Virtual and Real Environments*, pages 285–292, Budapest, Hungary, 2011.

[87] J.P. Meijaard, D.M. Brouwer, and J.B. Jonker. Analytical and experimental investigation of a parallel leaf spring guidance. *Multibody System Dynamics*, 23(1):77–97, 2010.

[88] J.P. Meijaard, B. Krijnen, and D.M. Brouwer. Deflection of an eccentric tooth of a comb-drive in an electrostatic field. In *Proceedings of ASME 2013 International Design Engineering Technical Conferences*, pages 1–7, Portland, Oregon, USA, 2013.

[89] J.P. Meijaard, B. Krijnen, and D.M. Brouwer. Deflection and pull-in of a misaligned comb drive finger in an electrostatic field. *Journal of Microelectromechanical Systems*, 23(4):927–933, 2014.

[90] M.Lutz, W. Golderer, J. Gerstenmeier, J. Marek, B. Maihofer, S. Mahler, H. Munzel, and U. Bischof. A precision yaw rate sensor in silicon micromachining. In *Solid State Sensors and Actuators*, volume 2, pages 847–850, Chicago, IL, USA, 1997.

[91] D. Mukhopadhyay, J. Dong, E. Pengwang, and P. Ferreira. A soi-mems-based 3-dof planar parallel-kinematics nanopositioning stage. *Sensors and Actuators A: Physical*, 147(1):340–351, 2008.

[92] COMSOL Multiphysics. `http://www.comsol.com/`, 2010.

[93] K. Najafi and K. Suzuki. A novel technique and structure for the measurement of intrinsic stress and young's modulus of thin films. In *Proceedings, IEEE Micro Electro Mechanical Systems, 1989, An Investigation of Microstructures, Sensors, Actuators, Machines and Robots*, pages 96–97, Salt Lake City, USA, 1989.

[94] M. Nakajima, F. Arai, and T. Fukuda. In situ measurement of youngs modulus of carbon nanotubes inside a tem through a hybrid nanorobotic manipulation system. *IEEE Transactions on Nanotechnology*, 5(3):243–248, 2006.

[95] H.C. Nathanson and R.A. Wickstrom. A resonant-gate silicon surface transistor with high-q band-pass properties. *Applied Physics Letters*, 7(4):84–86, 1965.

[96] W.E. Newell. Miniaturization of tuning forks. *Science*, 161(3848):1320–1326, 1968.

[97] W. Noell, P.A. Clerc, L. Dellmann, B. Guldimann, H.P. Herzig, O. Manzardo, C. Marxer, K. Weible, R. Dndliker, and N. de Rooij. Applications of soi-based optical mems. *IEEE Journal on Selected Topics in Quantum Electronics*, 8(1):148–154, 2002.

[98] M. Olfatnia, S. Sood, and S. Awtar. Note: An asymmetric flexure mechanism for comb-drive actuators. *Review of Scientific Instruments*, 83(11):116105, 2012.

[99] M. Olfatnia, S. Sood, J.J. Gorman, and S. Awtar. Large stroke electrostatic comb-drive actuators enabled by a novel flexure mechanism. *Journal of Microelectromechanical Systems*, 22(2):483–494, 2013.

[100] P.M. Osterberg and S.D. Senturia. M-test: A test chip for mems material property measurement using electrostatically actuated test structures. *Journal of Microelectromechanical Systems*, 6(2):107–118, 1997.

[101] J. Ouyang and Y. Zhu. Z-shaped mems thermal actuators: Piezoresistive self-sensing and preliminary results for feedback control. *Journal of Microelectromechanical Systems*, 21(3):596–604, 2012.

[102] S.L. Paalvast, H.T.M. Pham, P.M. Sarro, and R.H. Munnig Schmidt. Fast response thermal linear motor with reduced power consumption. In *Proceedings of the Eurosensors XXIII conference*, pages 690–693, 2009.

[103] A. Pantazi, M.A. Lantz, G. Cherubini, H. Pozidis, and E. Eleftheriou. A servomechanism for a micro-electro-mechanical-system-based scanning-probe data storage device. *Nanotechnology*, 15(10):S612–S621, 2004.

[104] S.T. Patton, K.C. Eapen, and J.S. Zabinski. Effects of adsorbed water and sample aging in air on the n level adhesion force between si(100) and silicon nitride. *Tribology International*, 34(7):481–491, 2001.

[105] A. Petropoulos, G. Kaltsas, and D. Goustouridis. A novel system for displacement sensing, integrated on a plastic substrate. *Microelectronics Journal*, 40(9):1387–1392, 2009.

[106] Polytec. `http://www.polytec.com/`, 2010.

[107] D.J. Rader, W.M. Trott, J.R. Torczynski, J.N. Castaeda, and T.W. Grasser. Measurements of thermal accomodation coefficients. Technical report, Sandia, 2005.

[108] M. Rakotondrabe, A.G. Fowler, and S.O.R. Moheimani. Control of a novel 2-dof mems nanopositioner with electrothermal actuation and sensing. *IEEE Transactions on Control Systems Technology*, accepted.

[109] N.M. Ravindra, B. Sopori, O.H. Gokce, S.X. Cheng, A. Shenoy, L. Jin, S. Abedrabbo, W. Chen, and Y. Zhang. Emissivity measurements and modeling of silicon-related materials: An overview. *International Journal of Thermophysics*, 22(5):1593–1611, 2001.

[110] S. Reggiani, M. Valdinoci, L. Colalongo, M. Rudan, G. Baccarani, A.D. Stricker, F. Illien, N. Felber, W. Fichtner, and L. Zullino. Electron and hole mobility in silicon at large operating temperatures part I: Bulk mobility. *IEEE Transactions on Electronic Devices*, 49(3):490–499, 2002.

[111] L.M. Roylance and J.B. Angell. A batch-fabricated silicon accelerometer. *IEEE Transactions on Electron Devices*, 26(12):1911, 1979.

[112] J.B. Sampsell. Digital micromirror device and its application to projection displays. *Journal of Vacuum Science & Technology B*, 12(6):3242–3246, 1994.

[113] E. Sarajlic, E. Berenschot, H. Fujita, G. Krijnen, and M. Elwenspoek. Bidirectional electrostatic linear shuffle motor with two degrees of freedom. In *18th IEEE International Conference on Micro Electro Mechanical Systems*, pages 391–394, Miami Beach, Florida, USA, 2005.

[114] R. Munnig Schmidt, G. Schitter, and J. van Eijk. *The Design of High Performance Mechatronics*. IOS Press, Amsterdam, The Netherlands, 1st edition, 2011.

[115] A.A. Seshia, M. Palaniapan, T.A. Roessig, R.T. Howe, R.W. Gooch, T.R. Schimert, and S. Montague. A vacuum packaged surface micromachined resonant accelerometer. *Journal of Microelectromechanical Systems*, 11:784–793, 2002.

[116] F.S. Sherman. A survey of experimental results and methods for the transition regime of rarefied gas dynamics. In *Rarefied Gas Dynamics*, volume 2, page 228, 1963.

[117] J.S. Shie, B.C.S. Chou, and Y.M. Chen. High performance pirani vacuum gauge. *Journal of Vacuum Science & Technology A*, 13(6):1972–1979, 1995.

[118] Solidworks Simulation. `http://www.solidworks.com/sw/products/solidworks-simulation.htm`, 2012.

[119] S.T. Smith and D.G. Chetwynd. *Foundations of Ultraprecision Mechanism Design*. CRC Press, Boca Raton, Florida, USA, 1st edition, 1992.

[120] H.M.J.R. Soemers. *Design Principles for Precision Mechanisms*. University of Twente, Enschede, The Netherlands, 1st edition, 2010.

[121] J. Stoer. *Einfhrung in die Numerische Mathematik*. Springer-Verlag, Berlin, Germany, 1st edition, 1972.

[122] L. Sun, J. Wang, W. Rong, X. Li, and H. Bao. A silicon integrated micro nano-positioning xy-stage for nano-manipulation. *Journal of Micromechanics and Microengineering*, 18(12):125004, 2008.

[123] S.M. Sze and Kwok K. Ng. *Physics of Semiconductor Devices*. John Wiley & Sons, Hoboken, NJ, USA, 3rd edition, 2006.

[124] W.C. Tang, T.H. Nguyen, and R.T. Howe. Laterally driven polysilicon resonant microstructures. *Sensors and Actuators*, 20(1):25–32, 1989.

[125] J.M.T. Thompson and G.W. Hunt. *A General Theory of Elastic Stability*. Wiley, London, UK, 1st edition, 1973.

[126] J. van Amerongen and T.J.A. de Vries. Digitale regeltechniek. Technical report, University of Twente, 2002.

[127] A.M.A. van der Heijden. *W.T. Koiter's Elastic Stability of Solids and Structures.* Cambridge University Press, Cambridge, UK, 1st edition, 2009.

[128] J. van Dijk. Systeem- en regeltechniek 2. Technical report, University of Twente, 2009.

[129] D.H. Wiersma, S.E. Boer, R.G.K.M. Aarts, and D.M. Brouwer. Design and performance optimization of large stroke spatial flexures. *Journal of Computational and Nonlinear Dynamics*, 9(1):011016, 2014.

[130] T. Yamane, N. Nagai, S. Katayama, and M. Todoki. Measurement of thermal conductivity of silicon dioxide thin films using a 3ω method. *Journal of Applied Physics*, 91(12):9772–9776, 2002.

[131] G. Zhou and P. Dowd. Tilted folded-beam suspension for extending the stable travel range of comb-drive actuators. *Journal of Micromechanics and Microengineering*, 13(2):178–183, 2003.

[132] Y. Zhu, A. Bazaei, S.O.R. Moheimani, and M.R. Yuce. Design, modeling, and control of a micromachined nanopositioner with integrated electrothermal actuation and sensing. *Journal of Microelectromechanical Systems*, 20(3):711–718, 2011.

[133] Y. Zhu, A. Corigliano, and H.D. Espinosa. A thermal actuator for nanoscale in situ microscopy testing: design and characterization. *Journal of Micromechanics and Microengineering*, 16(2):242–253, 2006.

Summary

Micro-electromechanical systems (MEMS) are all around us nowadays, especially in sensor technology. MEMS-based positioning stages can become favorable in applications where the available volume is small, the response needs to be fast, and the fabrication costs low. This thesis describes the development of such a positioning stage with integrated feedback in a simple, single-mask MEMS fabrication process. Fabrication is based on a silicon-on-insulator (SOI) wafer. A single mask is used for patterning of a resist layer. Afterwards two etching steps are performed, 1) directional deep reactive-ion etching (DRIE) through the silicon device layer and 2) isotropic vapour phase hydrogen fluoride (VHF) etching of the buried silicon dioxide layer.

A positioning stage cannot function without an actuator. An electrostatic comb-drive actuator does not only generate a force in the actuation direction, the actuator also generates forces in the lateral direction. These lateral forces can cause instability when the lateral stiffness of the complete flexure mechanism or the individual fingers is not sufficient. Several straight-line flexure mechanisms for guidance of a stage to reach large displacements are optimized with respect to their wafer footprint. The widely used folded flexure is still the best flexure mechanism for relatively small stroke, but lacks lateral stiffness for larger displacements. The slaved folded flexure, the tilted folded flexure, and the Watt flexure are more suitable for large displacements; the tilted folded flexure is for many combinations of required stroke and load force the optimal mechanism with respect to wafer footprint. For individual comb-drive fingers, both perfectly aligned and misaligned in the electrostatic field, the moment of pull-in is approximated analytically and verified with finite element simulations. The finite element results that include the effect of the grounded substrate are in close agreement with the measured deflection curves of misaligned fingers as a function of the applied voltage.

The position of the electrostatically actuated stage is measured by an integrated thermal displacement sensor. The operating principle of this sensor is the conductive heat transfer through air of a resistively heated silicon beam towards the actuated stage parallel to the beam. A lumped model of the sensor is presented and the sensor sensitivity is validated as a function of the doping concentration, the operating temperature, and the geometry. The sensor requires only little wafer

footprint and can reach nanometer resolution. For characteristic dimensions in the micrometer range the thermal conductivity of air is dependent on the pressure, which results in a drop in the sensor response in vacuum. Since the stage is elastically suspended and is mainly damped by air, for decreasing pressure the Q-factor of the stage increases. The effect of vacuum on the quasi-static and dynamic behavior of the stage, sensor, and actuator is modelled and verified by measurements. The results are used for stable position control of the stage.

The single degree-of-freedom (DOF) components are used to design, fabricate, and validate a closed-loop positioning stage in MEMS with three degrees-of-freedom. The range of motion of the 3DOF stage exceeds the range of motion of existing stages. The complete system is integrated in the device layer of a SOI-wafer. No assembly is required and the complete system can be fabricated using only a single mask.

Samenvatting

Micro elektromechanische systemen (MEMS) kom je tegenwoordig overal tegen, vooral als sensor. Positioneersystemen in MEMS kunnen voordelen bieden in toepassingen waar het volumebudget klein is, de responstijd snel en de fabricagekosten laag moeten zijn. Dit proefschrift beschrijft de ontwikkeling van een positioneersysteem met geïntegreerde terugkoppeling in een simpel fabricageproces gebruik makend van slechts één masker. Fabricage is gebaseerd op een 'silicon-on-insulator' (SOI) wafer. Het masker wordt gebruikt voor het schrijven van patronen in de fotoresist laag. Daarna worden twee ets stappen gedaan, 1) directioneel 'deep reactive-ion etching' (DRIE) voor het etsen door de devicelaag van het silicium en 2) isotroop gasvormig waterstoffluoride (VHF) etsen voor het verwijderen van het onderliggende siliciumdioxide.

Een positioneersysteem kan niet functioneren zonder actuator. Een elektrostatische kam actuator genereert niet alleen een kracht in de aandrijfrichting, deze actuator genereert ook krachten in de laterale richting. Deze laterale krachten kunnen instabiliteit veroorzaken als de mechanische stijfheid van het gehele bladveermechanisme of van de individuele vingers niet hoog genoeg is. Meerdere bladveermechanismes voor het rechtgeleiden van een stage over grote slag zijn geproduceerd en geoptimaliseerd naar benodigd wafer oppervlak. De veelgebruikte 'folded flexure' is voor kleine slag het optimale bladveermechanisme, voor langere slag mist dit mechanisme echter laterale stijfheid. De 'slaved folded flexure', 'tilted folded flexure' en het Watt mechanisme zijn beter geschikt voor grotere verplaatsingen; de 'tilted folded flexure' is voor veel combinaties van gewenste slag en vereiste kracht het optimale mechanisme kijkend naar het benodigde wafer oppervlak. Voor individuele vingers van de kam actuator, zowel symmetrisch als asymmetrisch gelegen in het elektrostatische veld, is het moment van instabiliteit analytisch bepaald en geverifieerd met eindige elementen simulaties. De resultaten van de eindige elementen analyse die het geaarde substraat meenemen komen goed overeen met de gemeten verplaatsing van de asymmetrisch gelegen vingers als functie van de elektrische spanning.

De positie van de elektrostatisch geactueerde stage wordt gemeten door een geïntegreerde thermische positiesensor. Het werkingsprincipe van deze sensor is warmteoverdracht door lucht, van een verhitte silicium structuur naar een parallel

gelegen stage. Een model van de sensor is ontwikkeld en de sensor gevoeligheid is gevalideerd als functie van de dopingconcentratie, de ingestelde temperatuur en de geometrie. De sensor heeft slechts weinig wafer oppervlak nodig en haalt nanometer resolutie. De geleiding van warmte door lucht is voor karakteristieke lengtes van enkele micrometers afhankelijk van de druk. Dit betekent dat de sensor gevoeligheid afneemt in een vacuüm omgeving. Omdat de stage elastisch is opgehangen en de beweging van de stage voornamelijk wordt gedempt door de lucht, neemt de Q-factor toe als de druk afneemt. Het effect van een vacuüm omgeving op het quasi-statische en dynamische gedrag van de stage, de actuator en de sensor is gemodelleerd en geverifieerd met metingen. De resultaten zijn gebruikt voor het stabiel regelen van de positie van de stage.

De componenten van het systeem voor één graad van vrijheid zijn gebruikt voor het ontwerpen, fabriceren en valideren van een teruggekoppelde positioneerstage in MEMS met drie vrijheidsgraden. Het bereik van onze stage is groter dan het bereik van bestaande stages. Daarnaast is het gehele systeem geïntegreerd in de devicelaag van een SOI-wafer. Er is geen assemblage nodig en het complete systeem kan gefabriceerd worden met behulp van slechts één masker.

Nawoord

Zes jaar geleden werd mij de kans geboden te beginnen aan dit onderzoek en dit is het eindresultaat. Het is mooi geweest. En dat is inderdaad dubbel op te vatten. Het werken met 'nieuwe' technieken is zowel mooi als frustrerend. Waarom werkt het de eerste keer wel en de tweede keer niet? Wat hebben we anders gedaan dan de vorige keer? Hoe is dit gedrag nu weer te verklaren? Uiteindelijk kijk ik met een trots en voldaan gevoel terug. We zijn er in geslaagd iets moois te maken.

Allereerst wil ik Demcon natuurlijk bedanken voor het bieden van deze kans. De unieke mogelijkheid om een promotie onderzoek te combineren met 'echt' werk was ideaal. Daarnaast wil ik vele collega's bij Demcon bedanken voor de interesse in mijn onderzoek.

Dannis, bedankt voor de dagelijkse begeleiding! Ik vond het heel prettig samenwerken, je was altijd beschikbaar voor een kritisch of afleidend gesprek. Je kennis van MEMS en van constructieprincipes heb ik zoveel mogelijk proberen mee te nemen. Leon, de manier waarop je problemen tot de kern kan terugdringen is indrukwekkend en je enthousiasme is aanstekelijk; bedankt! Daarnaast wil ik Herman en Just bedanken voor de tijd en moeite die jullie hebben gestoken in het begeleiden van mijn promotie. Johan, bedankt voor het mij leren omgaan met MEMS. Léon en Jaap, bedankt voor jullie bijdrages aan dit proefschrift.

Je hoort wel eens slechte verhalen over de inzet van studenten in een promotietraject. Ik denk dat ik geluk heb gehad. Richard, Jan-Willem, Koen, bedankt voor jullie bijdrage aan dit werk.

Naast het werk is het belangrijk om afleiding te hebben. Al jarenlang voetbal ik met veel plezier bij PW. Wonder boven wonder is het ons afgelopen seizoen zelfs gelukt om kampioen te worden, waardoor het afronden van dit onderzoek al de tweede promotie van dit jaar wordt. Buiten het voetbal om wil ik de 'zondagavond groep' noemen voor de sportieve en culinaire afleiding in de weekenden.

En natuurlijk is het fijn als je terug kan vallen op een aantal mensen. Bedankt pap en mam voor de deur die altijd openstaat, ook al maak ik daar niet altijd even vaak gebruik van. En verder dat jullie mij lekker mijn eigen gang laten gaan en mij mijn eigen keuzes laten maken. De laatste jaren is Marjolein daar bijgekomen; het is een erg goed gevoel dat er iemand is. Laten we de drukte even vaarwel zeggen om te gaan genieten van een welverdiende rondreis door Zuid-Amerika.

Micro-electromechanical systems (MEMS) are all around us nowadays, especially in sensor technology. MEMS-based positioning stages can become favorable in applications where the available volume is small, the response needs to be fast, and the fabrication costs low. This thesis describes the development of such a positioning stage.

Single degree-of-freedom (DOF) electrostatic actuators are used to apply a force to a shuttle that is constrained to move over a straight line by a flexure mechanism. The position of the shuttle is measured by using an integrated sensor. The operating principle of this sensor is the conductive heat transfer through air of a resistively heated silicon beam towards the actuated shuttle parallel to the heated beam. Closed-loop position control of the shuttle using the integrated sensor is demonstrated.

Three single DOF shuttles are coupled to form a parallel kinematic 3DOF stage for in-plane motion. The 3DOF stage was designed, fabricated, and validated to have a large range of motion compared to existing stages. The complete stage is integrated in the device layer of a SOI-wafer, which means no assembly is required and the stage can be fabricated using only a single mask.

Bram Krijnen received a M.Sc. degree in electrical engineering from the University of Twente Enschede, The Netherlands, in 2007. Afterwards he joined Demcon Advanced Mechatronics in Enschede as a mechatronic system engineer, while at the same time pursuing a research project leading to this doctoral thesis in 2014. Bram continues his career at Demcon.

ISBN: 978-90-365-3730-8